A Comparative Study of Coherent & Incoherent Doppler Lidar Techniques

Submitted by

Wilbert R. Skinner and Paul B. Hays

Study Report Prepared for

Marshall Space Flight Center

Performed Under Contract NAS8-38775

June 3, 1994

Contents

Figures

Tables

1. Introduction

Accurate measurement of the global wind field in the lower atmosphere has long been recognized as important to the accuracy of weather forecasts (Atlas and Korb, 1981; Atlas et al., 1985; Grassotti et al., 1991) as well as being an important component in the solution of many other scientific questions (Curran et al., 1987a). The most promising technique for measuring global wind fields is to use a space-borne Doppler lidar.

Two different technologies can be used to determine the Doppler shift: coherent, and incoherent or direct detection. There is a great deal of misunderstanding between the proponents of the two techniques about the capabilities and limitations of each system. This report attempts to bridge the gap by discussing each technique and comparing their capabilities. Since the authors are familiar with incoherent techniques and the audience is primarily more familiar with the coherent method, one of the main emphases of this report is to explain in some detail the basic incoherent detection concepts.

Although there has not been nearly as much effort expended on incoherent detection as on coherent, a number of works have appeared that give some theoretical background and operational results of the technique. Ground-based incoherent lidar systems working in the yellow-green wavelength (0.5 μm) region have demonstrated a capability to measure vector wind with an accuracy of approximately 1 m/sec (Benedetti-Michelangeli et al., 1972, 1974; Chanin et al., 1989; Teply et al., 1991; Abreu et al., 1992). In particular, the paper by Abreu et al. describes a system that is very similar to the incoherent lidar system we will describe later. This technique of determining wind velocity relies on detecting the Doppler shift experienced by a pulse of narrow-band laser light as it is scattered by the atmosphere. The detection is accomplished using an incoherent interferometric determination of the laser wavelength before and after scattering. The implications of carrying out such measurements from an orbital platform were first discussed by Abreu (1979). Hays et al. (1984) extended that early investigation and carried out a detailed system trade-off assessment. This paper presented the theoretical model of a Doppler lidar with incoherent Fabry-Perot detection, followed by a development of the technique used for system optimization. Several near-optimum systems were discussed and evaluated to illustrate the variations which could be developed from the engineering point of view. The result of this analysis was a conceptual design for a 0.5μ incoherent lidar to be operated from a spacecraft flying at an altitude of 800 km. The design study optimized the system in terms of the statistical uncertainty in measuring the horizontal wind speed. The result of this optimization was a class of high-resolution Fabry-Perot interferometers which operate at very high orders, that is, have long spacer gaps and free spectral ranges of the order of 0.03 cm^{-1} (1 GHz). Rosenberg and Sroga (1985) discussed some engineering implications and early prototype results for an incoherent system. In 1989 the University of Michigan examined some engineering aspects of a space-borne incoherent system using a frequency double Nd:YAG laser (Abreu et al., 1989). McDermid et al. (1985) and Rees and McDermid (1990) considered an incoherent system operating in the near UV at either 308 nm with an XeCl excimer laser or near 355 nm with a frequency tripled Nd:YAG. Such systems would operate in an eye-safe region of the spectrum and eliminate one of the difficulties that accompany visible light systems. Korb et al. (1992) described a variation of incoherent detection known as the "Edge technique," which differs from other incoherent techniques in the details of the detector design.

The work presented here expands on these earlier results. The necessary background material is discussed in Section 3. We will consider a technique which converts the circular fringes of a Fabry-Perot interferometer into a linear pattern, thus allowing the use of a conventional linear detector such as a CCD. The effect of this detection system for a space-borne lidar is that the detector efficiency is increased by a factor of ~10. This order of magnitude increase has profound implications when the incoherent and coherent techniques are compared. Previous comparisons (Menzies, 1985, 1986) used incoherent designs with low quantum efficiencies in comparisons with coherent systems. In addition, the incoherent systems were not optimized to the extent that has been done here.

We will consider the results of the GLOBE study of aerosol backscatter more carefully than previous incoherent lidar studies. The low aerosol concentrations that are common in the free troposphere have implications for the performance of both coherent and incoherent systems. This has caused us to examine lidars that can use the molecular backscatter signature. The molecular signature, while not as sensitive to Doppler shifts as the aerosol return, is relatively steady and provides a large signal that gives a good measure of the wind.

Our purpose in this report is two-fold: 1) describe the basics of the coherent and incoherent systems, particularly the latter, and 2) compare the performance of the two technologies in a meaningful way. In order to concentrate on these issues, we will not address many other questions of interest. We will not, for example, discuss the relative merits of different scanning strategies. The accuracy and coverage requirements for a wind sensor will not be discussed, although both are quite important for the design of any system. We also recognize that our description of the incoherent system will leave some questions unanswered Questions such as the effects of correlations between backscatter coefficients and wind are important, but fundamentally of second order and beyond the scope of this study.

We conclude that an incoherent system, if properly designed, can achieve accuracies that are comparable to those obtained by a coherent system. An incoherent system can make useful wind measurements even when the aerosol concentration is very low. This insures that global wind measurements can be made. An incoherent system has no problems with speckle, and the measurements can be readily averaged to reduce the total wind uncertainty (measurement error plus atmospheric wind variance). These factors need to be considered very carefully when considering the relative merits of the two technologies.

2. Aerosol Distributions

The global distribution of aerosol scatterers throughout the troposphere and lower stratosphere is a critical issue in the design of a wind-sensing lidar system. This is particularly true for the coherent lidars which only scatter from aerosols. The question is complicated further when one is comparing the performance of lidar systems which have base operating wavelengthts that vary from the near ultraviolet at 355 nm to 9.1 microns in the infrared. The aerosol particles contributing to the backscatter in these two extreme regions are quite different in size. Scattering in the visible and near ultraviolet takes place primarily from aerosols with a radius near 0.1 microns, while in the infrared near 9.1 microns the contributing size is closer to 1.0 microns. Thus, it is difficult to directly relate the scattering in these spectral regions. There do appear to be relatively simple relationships for particular populations of scatterers. Gras et al. (1991) show that in the free troposphere the ratio of their calculated backscattering cross sections varies with a ratio very close to the inverse square of the wavelength. Observed betas have, on the average, a somewhat smaller ratio. An interesting note here is that this inverse square variation with wavelength implies that the sensitivity of coherent lidars should be relatively independent of wavelength (Gras et al., 1991).

We begin by considering the aerosols that will scatter infrared radiation near the 9.1 micron region.

2.1. *Infrared Spectral Region*

There are a number of studies of the distribution of aerosol scatterers in the size range that influences mid-infrared radiation. One of the first published studies

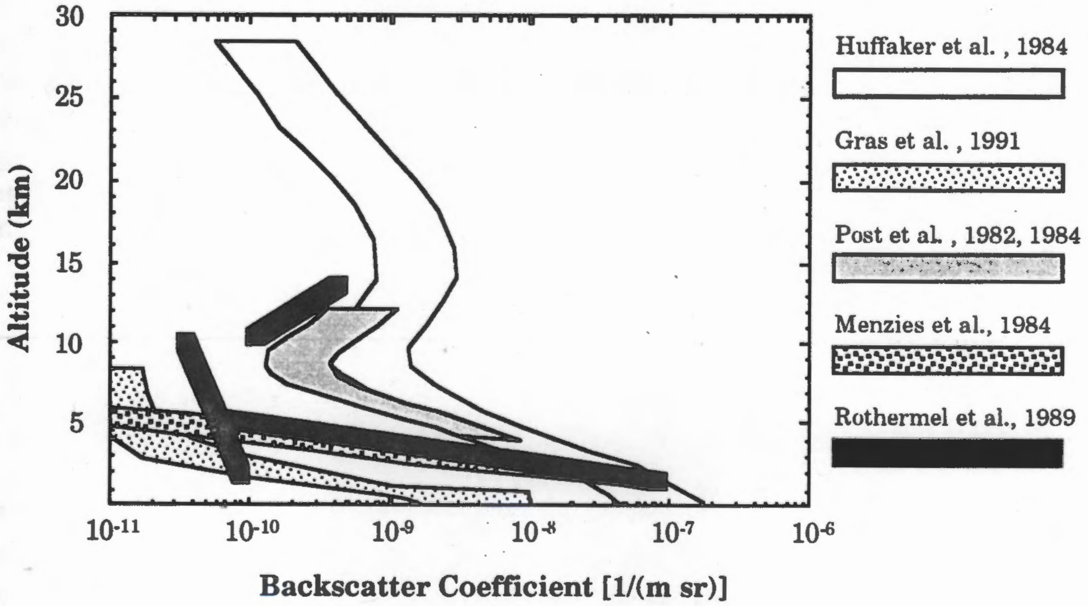

Fig. 1. Aerosol backscatter coefficients at 10 microns.

(Huffaker et al., 1984) of the coherent lidar used information on the aerosol scatterers as observed with visible light (Kondratyev et al., 1976), as well as from the AFCRL models (Valley, 1965), to estimate the scattering in the infrared. The aerosol backscatter coefficients in this study were treated as random variables with the mean lying in the band shown in Fig. 1 labeled Huffaker et al., 1984. These values are close to those used by Abreu (1979), Abreu et al. (1981), and Hays et al. (1984) with a scaling appropriate for the shorter wavelengths. These values are high compared to the more direct observations described by Post et al. (1982), Post (1984), Menzies et al. (1984), and the more modern observations reported by Rothermel et al. (1989), and Gras et al. (1991). A composite of these reports and observations is shown in Fig. 1. All of these backscatter profiles tend to have very low values in the middle troposphere. This tendency for the air to be clean in this region is especially significant in the southern hemisphere where values of the backscatter coefficient can drop as low as 10^{-11}/(m sr), as seen in the observations reported by Gras and Jones (1989) and Gras et al. (1991). The study by Rothermel et al. is of particular interest since they relate the aerosol populations to different physical sources. They report the mixing ratio of aerosol in air and identify three relatively distinct populations of aerosols in the troposphere. They find 1) a background population with mixing ratio of about $10^{-10}(m^2/kg^{-1}sr^{-1})$, 2) a convective population that varies rapidly with altitude starting at about $10^{-7}(m^2/kg^{-1}sr^{-1})$ at 2 kilometers and eventually dropping to $10^{-10}(m^2/kg^{-1}sr^{-1})$ at 6 kilometers, and finally 3) a slowly varying stratospheric population that increases with altitude starting from a value of about 5×10^{-10} $(m^2/kg^{-1}sr^{-1})$ at 10 kilometers. They note that the stratospheric aerosol content will vary widely depending upon volcanic activity. Rothermel's study is particularly significant since they conclude that a significant fraction of the Earth's atmosphere above the planetary boundary layer may be very clear and produce very little aerosol backscatter. The statistical results of the GLOBE 1990 study (Bowdle, 1994) support this conclusion and indicate that the background population and the convective population are present in most samples to varying degrees. The convective population appears to be absent over the oceans in a significant fraction of the observations. It is quite possible that the troposphere is indeed very clean in regions of the atmosphere far removed from industrial contamination, and that in the regions where there are a lack of wind observations there are also very few aerosols.

2.2. *Chapman Layer Stratospheric Aerosol Model*

We use a multicomponent model based on the observations of Rothermel et al. (1989) to simulate the distribution of aerosols with height. The mixing ratio of aerosols is composed of four functions. From the ground to 1 kilometer the mixing ratio is constant and determined by conditions in the planetary boundary layer. Above that altitude the mixing ratio is composed of a constant background mixing ratio contribution, an exponentially decreasing convective contribution, and a modified Chapman layer to represent the stratospheric aerosols. There are three parameters in this formula that can be varied to simulate the aerosol distributions in various regions of the atmosphere. These are the boundary layer mixing ratio,

M_{BL}, the background mixing ratio, M_{BG}, and a stratospheric mixing ratio contribution, M_{ST}. The model has the form

$$\beta(z) = \begin{cases} \rho(z) M_{BL} & Z \le Z_{BL}, \\ \rho(z)\left(M_{BG} + M_{BL}\, 10^{-0.75*(Z-Z_{BL})}\right) + M_{ST} \exp\left[-\left(\frac{z - z_{ST}}{H_{ST}}\right) - e^{-\frac{z-z_{ST}}{2H_{ST}}}\right] & Z \ge Z_{BL}, \end{cases} \qquad (1)$$

where $Z_{BL} = 1.0$ km, $Z_{ST} = 20.0$ km, and $H_{ST} = 3.0$ km.

An interesting global form of this model would be to set the boundary layer, background, and stratospheric mixing values to a simple set of conditions, such as continental and oceanic boundary layers, northern and southern hemisphere background values, and stratospheric values which vary with latitude depending on volcanic activity. However, in this study we use this model to quantify the various situations for which we compare the two types of lidar.

A typical range of values is:

$1.0 \times 10^{-9} < M_{BL} < 1.0 \times 10^{-7}$ (boundary layer)
$1.0 \times 10^{-11} < M_{BG} < 1.0 \times 10^{-9}$ (background)
$5.0 \times 10^{-10} < M_{ST} < 5.0 \times 10^{-9}$ (stratospheric mixing)

These situations are illustrated in Fig. 2 where these aerosol model profiles are shown overlaying the primary observations we have discussed. These were calculated using the IDL program given in Appendix I.

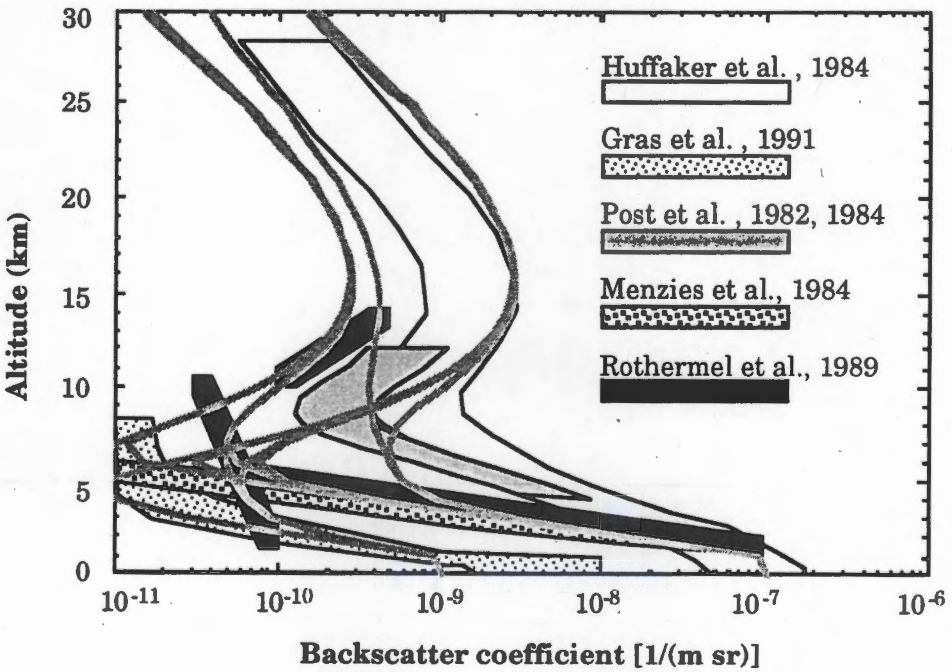

Fig. 2. Range of backscatter coefficients represented by the new aerosol model. Included is the data presented in Fig. 1 and curves generated by using Eq. (1).

2.3. *Visible and Near Ultraviolet Aerosol Backscatter*

We have previously noted that there is a relatively simple approximate relationship for the variation of backscattering with wavelength. Gras et al. (1991) show that in the free troposphere the ratio of their calculated backscattering cross sections varies very close to the inverse square of the wavelength. These calculations are based on the observed particle size distribution functions. Directly observed betas are, on the average, somewhat less regular. We choose to use the simple inverse square law to relate the backscattering with wavelength. This allows a simple and relatively fair comparison of the coherent and incoherent lidar systems. The backscatter coefficients used in this study are shown in Fig. 3. This simple model of the aerosol distribution allows us to describe the various geophysical situations in which lidar observations would be made and allows a simple comparison to the behavior of the backscatter at the various wavelengths. Choice of the boundary layer, free troposphere, and stratosphere scattering can be easily used to simulate northern or southern hemisphere, continental or oceanic, and various conditions of volcanic activity in our comparison.

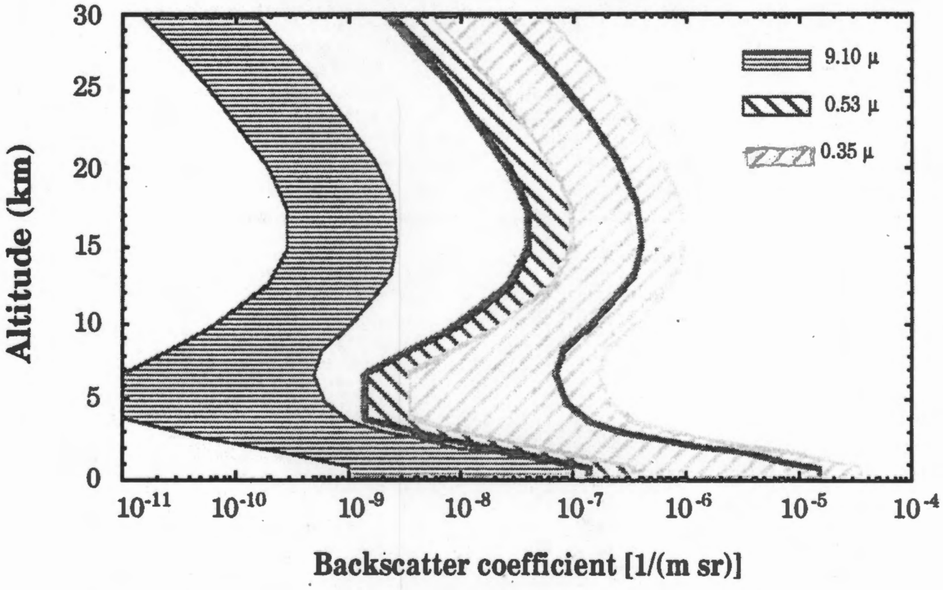

Fig. 3. Range of backscatter coefficients for various wavelengths.

3. Description of Incoherent and Coherent Wind Profilers

3.1. *Description of Incoherent Lidar*

3.1.1. OPERATION OF INCOHERENT LIDAR

The incoherent lidar system investigated here makes use of a Fabry-Perot interferometer (also called an etalon) as a high spectral resolution element, capable of detecting Doppler shifts of the backscattered signal that correspond to velocities less than 1 m/s. A schematic of a conceptual system configuration is presented in Fig. 4. The figure illustrates how laser light which has been scattered by the atmosphere is gathered by a telescope and collimated before passing through an etalon. An actual space-borne incoherent lidar system would have many similarities to the High Resolution Doppler Imager (HRDI) on the Upper Atmosphere Research Satellite which measures winds by passive measurement of absorption and emission lines in the Earth's stratosphere, mesosphere and lower thermosphere (Hays et al., 1993). A Fabry-Perot interference pattern (set of concentric rings) appears at the infinity focus of the interferometer objective lens, where a detector system is placed. Figure 5 shows the interference pattern of the interferometer as it appears in the image plane. If one were to spatially scan one order of the interferometer in the image plane, the line shape of the backscattered laser signal would be obtained. This is illustrated in Fig. 6, with Fig. 6(a) showing the line shape for two cases, one with and one without a Doppler shift. The difference between the two is shown in Fig. 6(b). The Doppler shift causes an increase in the signal in some channels and a decrease in others. It is from this line shape information that Doppler shift is obtained. A special detector is necessary in order to spatially scan the interferometer's image plane due to the

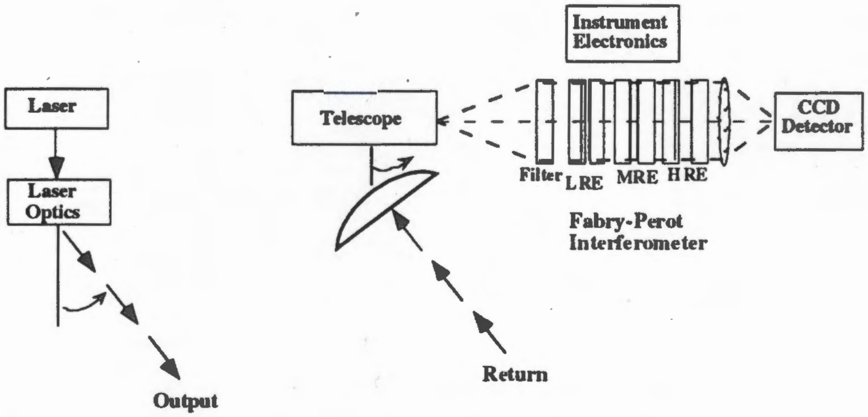

Fig. 4. Schematic of a conceptual incoherent lidar system configuration.

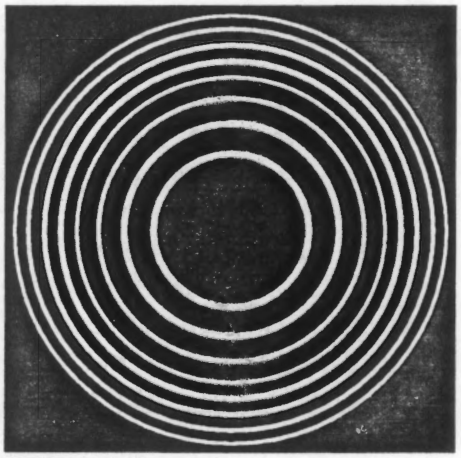

Fig. 5. Fabry-Perot interferometer fringe pattern.

circular nature of the pattern. The Fabry-Perot interferometer flown on the Dynamics Explorer satellites (Hays et al., 1981; Killeen et al., 1983) and HRDI (Hays and Wang, 1991) used a multi-ring anode detector to spatially scan the image plane. An alternative to the multi-ring anode detector is a technique developed by Hays (1990) which converts the circular fringes into a linear pattern which can be detected with a conventional linear detector, such as a CCD. This is a very critical development as it increases the sensitivity of the instrument by more than a factor of 10. Description and details of the basic optical components of this system from an engineering point of view will be considered in the next section.

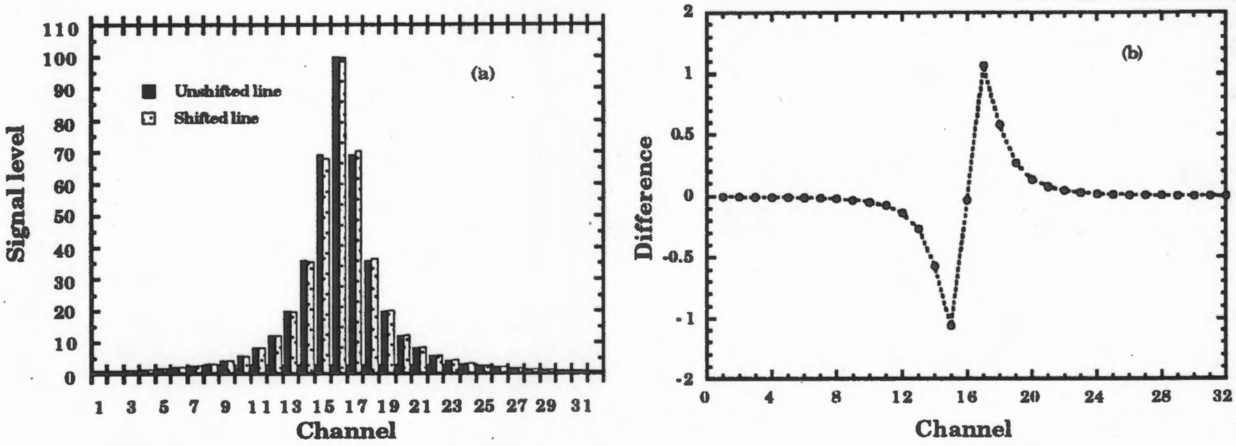

Fig. 6. (a) Spectral line signature with and without Doppler Shift. (b) Difference of shifted and unshifted line.

3.1.1.1. *CCD detection*. A technique for converting the circular fringes of a Fabry-Perot interferometer into a linear pattern which can be detected with a conventional linear detector has been described by Hays (1990). The technique, called the Circle to Line Interferometer Optical System (CLIO), simplifies the analysis of interferometric information by converting the circular rings, or fringes, into a linear pattern similar to that produced by a conventional spectrometer. The resulting linear fringe pattern can be scanned using any one of the many commercially available linear array detectors, such as a CCD. Advantages of a CCD over a conventional IPD are higher quantum efficiency, wider spectral range, lower cost, more flexibility of operation, and simpler electronics.

The specific optical technique used to produce this linear interference pattern is to transform the rings that appear at the infinite focus of the objective lens in a Fabry-Perot interferometer into a series of line segments on the axis of a 45° half-angle internally reflecting cone. This process may be accomplished using a single sector of a cone to transform a sector of the circular ring pattern. The entire ring pattern may also be transformed by combining a cone sector with an optical kaleidoscope which concentrates the entire fringe pattern into the single cone sector, typically a 90° to 120° pie shaped azimuthal region in the fringe plane. The basic optical configuration is illustrated schematically in Fig. 7. Here the cone is shown to be situated with its vertex on the optical axis in the focal plane of the main objective lens of the Fabry-Perot optical system where the ray bundles are focused.

The cone acts as a very astigmatic element that focuses all meridional rays of light which would intersect a circle in the fringe plane at a point on the cone axis. Rays which are not in the meridional plane tend to be focused on a line that is perpendicular to the cone axis at the same axial distance from the vertex.

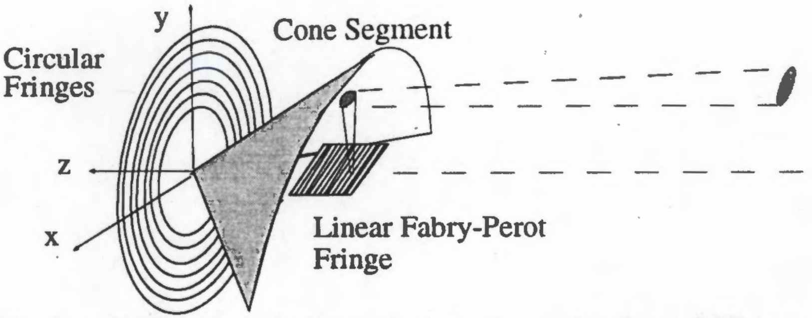

Fig. 7. Schematic of basic optical configuration for a CCD/cone system.

While an IPD has only 12 or 32 rings, a conventional CCD combined with the conical circle-to-line optical system can provide a nearly perfect 500 element ring detector. Furthermore, linear solid-state detectors have advantages in providing high quantum efficiency, small, rugged construction, and low cost. An experimental test of this device was reported by Hays (1990) with a positive result.

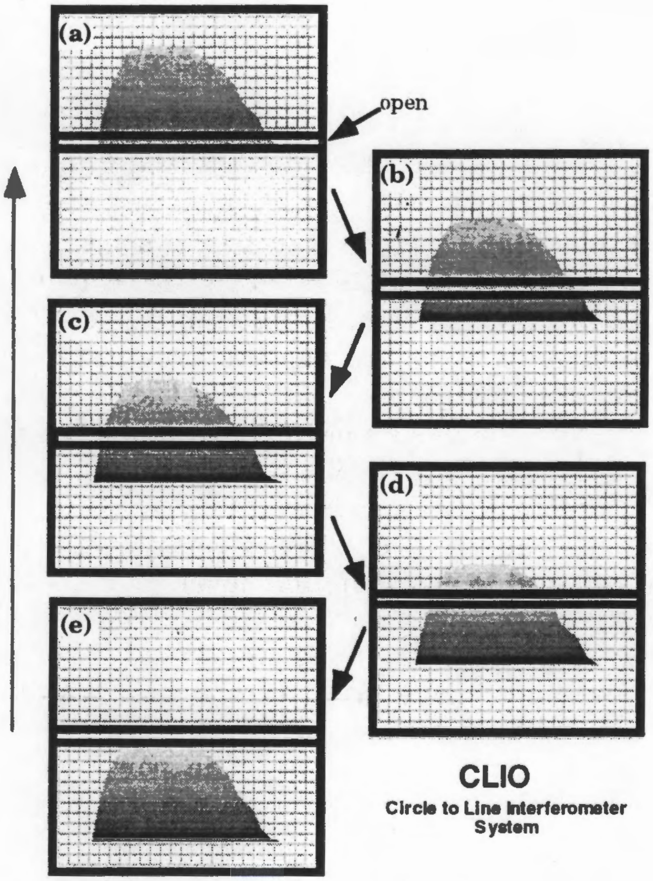

Fig. 8. CCD Lidar Detector time history. As the pulse returns from various altitudes the image is shifted across the detector (steps a through e). At the end the image is shifted back to the start for the next laser pulse (step e to a). Only the segment of the CCD marked "open" is actually exposed to light.

The CCD detector would be used in a configuration similar to a streak photographic system. The entire chip would be masked off from incoming light, except for a few rows of pixels at the chip's midpoint. These exposed pixels would sit in the image plane of the Circle-to-Line Converter. Just before the laser is fired, the CCD begins shifting the exposed pixels up under the mask. This first set of pixels gives dark count and background information. After the laser is fired the return signal is imaged onto the exposed rows of pixels. While the CCD is shifting its pixels upward a very small portion of the laser light is leaked into the interferometer and onto the CCD. This provides the laser spectral reference. As the laser pulse is propagating in the atmosphere the CCD chip is continually shifted upward so as to save the image data from previous altitudes and expose new pixels. In this way an image is created where a row of pixels contains spectral information at a particular altitude. Once the return signal is finished, the CCD resets to the bottom and waits for the next return signal from the atmosphere. This will require approximately 5.3 milliseconds. The process just described is illustrated in Figs. 8(a)-(e).

A typical requirement for wind measurement is 1 km altitude resolution. At a firing angle of 45° the laser pulse requires 9.42 μ sec to propagate down through 1 km of atmosphere and have the scattered signal come back up the 1 km. At a maximum shift rate of 1 pixel per microsecond, then, the CCD can shift approximately 10 pixels per kilometer. This rate would require the slit opening of the CCD's mask to be 10 pixels wide. During the readout process those 10 pixels will be summed together into a single altitude measurement. The time duration for the signal to traverse from a 25 km altitude down to ground level and back is 236 μ sec. At 10 pixels per altitude resolution this now gives us a total of 25 altitude samples. There could be from 10 to 100 wavelength samples, depending on details of the system. This gives a total data output of 250 to 2500 data points.

3.1.2. MATHEMATICAL DESCRIPTION OF INCOHERENT LIDAR

The Fabry-Perot detector system used in these analyses is similar to the High Resolution Doppler Imager (HRDI) developed for passive wind measurements on board the Upper Atmosphere Research Satellite (UARS) (Hays et al., 1993). This is a stable, high-resolution system consisting of a solid plane etalon and a multi-ring anode detector to spatially scan the image plane of the Fabry-Perot interferometer. In addition, to the high-resolution element for spectral scanning, two etalons and an interference filter are used to provide a very narrow-band filtering element and allow the device to operate in the large solar background present during the daytime. The design of multiple etalons has been discussed elsewhere (Skinner et al., 1987; McNutt, 1965) and will not be reiterated here. It is sufficient to note that it is practical with such systems to make the parasitic light 10%-30% of the light transmitted by the desired passband. This is sufficient to reduce the solar background to an acceptable level.

In this section we will review the basic lidar equations, including the appropriate spectral character. The analytical form of the Fabry-Perot will be presented followed by convolution of the two which will provide the form of the signal measured by the instrument.

3.1.2.1. *Lidar equation*. The power collected per lidar pulse is given by the convolution of the transmitted signal and the broadening functions associated with the scattering media:

$$\overline{P}(r,\nu) = \frac{P_T O_A(r) A_T \Delta h T^2(r)}{4\pi r^2} \cdot \left\{ P_A(\pi,r)\beta_A(r) f(\nu,\nu_1,U,\alpha_A,\Delta\nu_1,\Delta\nu_T) + P_m(\pi,r)\beta_m(r) f(\nu,\nu_1,U,\Delta\nu_G,\Delta\nu_1,\Delta\nu_T) \right\}, \tag{2}$$

where $\overline{P_r}(r,\nu)$ is the power returned from range r and wavenumber ν, P_t is the laser power transmitted centered at wavenumber ν_l, $O_A(r)$ is the fractional overlap of the telescope field of view and the laser beam, A_r is the area of the receiving telescope, $P_s(\pi,r)$ is the scattering phase function at range r for backscatter (180°), and s can either represent aerosols (A) or molecules (m). The 4π in the denominator normalizes the scattering phase function over all angles ($\iint P(\theta,\phi)\sin\theta\, d\theta\, d\phi = 4\pi$), $\beta_s(r)$ is the scattering coefficient at range r, and Δh is the line-of-sight resolution. The quantity $T^2(r)$ accounts for the round-trip extinction along the laser beam path between the source and the scattering media. This round-trip extinction for a single scattering atmosphere is given by

$$T^2(r) = \exp\left\{-2\int_0^r [\beta_A(r') + \beta_m(r')]dr'\right\}. \tag{3}$$

The fractional overlap of the telescope field of view and the laser beam, $O_A(r)$, varies as a function of range and is important for ground-based systems where it is desired to measure the field very close to the ground. A space-based system would have a constant overlap, and it can be made as close to unity as desired. The function f represents the terms that determine the spectral shape of the return. We consider the shape to be determined by the factors described in Sections 3.1.2.2 to 3.1.2.5.

3.1.2.2. *Doppler shift due to mean wind motions*. The Doppler shift is given by

$$\Delta\nu = \nu_l \frac{2U_h \sin\phi}{c}, \tag{4}$$

where $\Delta\nu$ is the Doppler shift, ν_l is the laser wavenumber, U_h is the horizontal wind speed in the direction of viewing, and ϕ is the angle from nadir the beam makes as it passes through the layer.

3.1.2.3. *Laser width*. The spectral shape of the laser is assumed to be Gaussian of the form

$$G_{laser}(\Delta\nu,\Delta\nu_l) = \frac{1}{\sqrt{\pi}\,\Delta\nu_l} e^{-\frac{\Delta\nu^2}{\Delta\nu_l^2}}, \tag{5}$$

where $\Delta\nu_l$ is the 1/e width of the laser. We will discuss later the necessary laser widths.

3.1.2.4. *Scattering broadening*. The scattering media (aerosols and molecules) broaden the signal due to their random motions. The molecules have a Gaussian broadening function:

$$G_{molecules}(\Delta\nu,\Delta\nu_G) = \frac{1}{\sqrt{\pi}\,\Delta\nu_G} e^{-\frac{\Delta\nu^2}{\Delta\nu_G^2}}, \tag{6}$$

where $\Delta\nu_G$ is the 1/e width and is given by

$$\Delta\nu_G = \frac{\nu_l}{c}\left(\frac{2kT}{m}\right)^{\frac{1}{2}}, \tag{7}$$

or

$$\Delta\nu_G = 4.30\times10^{-7}\,\nu_l\left(\frac{T}{M}\right)^{\frac{1}{2}}, \qquad (8)$$

where k is Boltzmann's constant, m is the mean mass of a molecule in the atmosphere, and M is the mean molecular weight (M=28.964). Typical values of the Rayleigh width are shown in Table 1.

Table 1. Typical Rayleigh widths.

T (K)	$\Delta\nu_G$					
	cm^{-1}		nm		MHz	
	355 nm	532 nm	355 nm	532 nm	355 nm	532 nm
200	3.18×10^{-2}	2.12×10^{-2}	4.01×10^{-4}	6.01×10^{-4}	955	637
250	3.56×10^{-2}	2.37×10^{-2}	4.48×10^{-4}	6.72×10^{-4}	1067	712
300	3.90×10^{-2}	2.60×10^{-2}	4.91×10^{-4}	7.36×10^{-4}	1169	780

The aerosol function has a Lorentzian form (Fiocco and DeWolf, 1968; Benedetti-Michelangeli et al., 1972)

$$L_{aerosol}(\Delta\nu,\alpha_A) = \frac{1}{\pi}\frac{\alpha_A}{\alpha_A^2+\Delta\nu^2}, \qquad (9)$$

where the half width α_A is given by

$$\alpha_A = \frac{2\pi\nu^2 D}{c}, \qquad (10)$$

with D the diffusion coefficient. Table 2 shows typical aerosol widths as a function of particle radius.

Table 2. Typical aerosol widths.

Particle Radius (μm)	Diffusion Coefficient cm^2s^{-1}	α_A				
		cm^{-1}		nm	MHz	
		355 nm	532 nm		355 nm	532 nm
10^{-2}	1.3×10^{-4}	2.1×10^{-5}	9.5×10^{-6}	2.7×10^{-7}	6.5×10^{-1}	2.9×10^{-1}
10^{-1}	2.2×10^{-6}	3.7×10^{-7}	1.6×10^{-7}	4.6×10^{-9}	1.1×10^{-2}	4.9×10^{-3}
10^{0}	1.3×10^{-7}	2.1×10^{-8}	9.5×10^{-9}	2.7×10^{-10}	6.5×10^{-4}	2.9×10^{-4}

The widths are extremely narrow compared to the molecular broadening and in most cases are much narrower than the laser pulse so that aerosol scattering is essentially a delta-function.

3.1.2.5. *Turbulent motions*. In addition to random motions of molecules and aerosols, the model allows for random motions of bulk parcels, i.e. turbulence. We assume a simple Gaussian shape to represent this broadening:

$$G_{\text{turbulence}} = \left(\Delta\nu, \Delta\nu_T\right) = \frac{1}{\sqrt{\pi}\ \Delta\nu_T} e^{-\frac{\Delta\nu^2}{\Delta\nu_T^2}}, \tag{11}$$

where

$$\Delta\nu_T = \frac{\nu_1}{c} U_T,. \tag{12}$$

and ν_T is a characteristic turbulent velocity.

The spectral shape of the return signal has the quantitative form shown in Fig. 9. The molecular scattered light has a broad spectral shape and the aerosol scattered light forms a sharp peak. Underlying that form is a background from scattered sunlight, which at this scale forms a flat continuum.

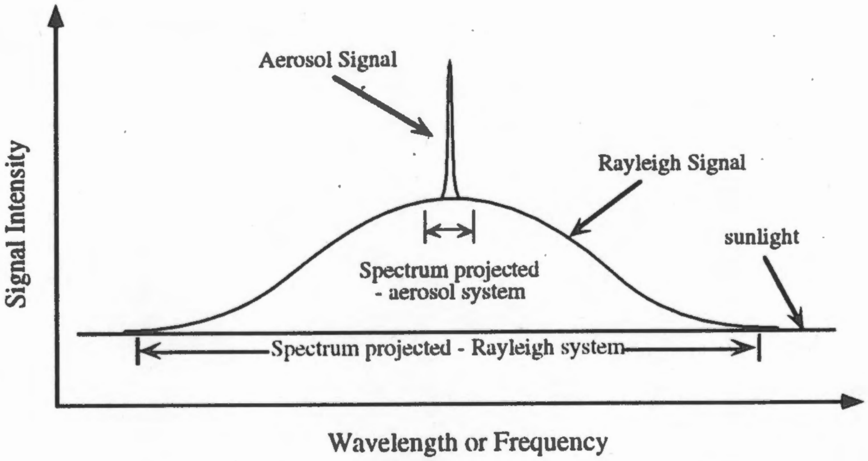

Fig. 9. Return signal for an incoherent lidar system.

3.1.2.6. *Fabry-Perot interferometer*. The Fabry-Perot interferometer is a simple device, as shown in Fig. 10. It consists of two very flat transparent plates that are held parallel to each other. In the figure, the plates are separated by three posts that are carefully ground to be the same length. The inner surface of each plate is coated with a high reflectivity coating. This coating is usually a dialectic multilayer, but occasionally silver or aluminum is used. The systems we are concerned with are multiple Fabry-Perot systems and in general we must include interactions between the etalons to accurately represent the transmission function. However, these interactions are not significant in most of the systems we discuss and additional etalons can be considered part of the filtering system. Later we will describe a system that does require such considerations and the appropriate equations are developed in Appendix II. Here we develop the equations for a single etalon system. The transmission, T, of a perfect Fabry-Perot is given by the Airy function (see Hernandez, 1986, or Vaugh, 1989, for a complete description of the Fabry-Perot):

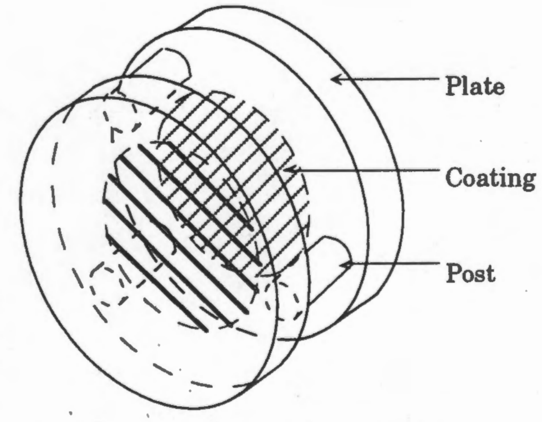

Fig. 10. Fabry-Perot interferometer. The main components are two flat plates, highly reflecting dielectric coating and three posts to hold the plates parallel.

$$T(m)=\frac{\left(1-\frac{L}{1-R}\right)^2(1-R)^2}{1-2R\cos 2\pi M+R^2}, \quad (13)$$

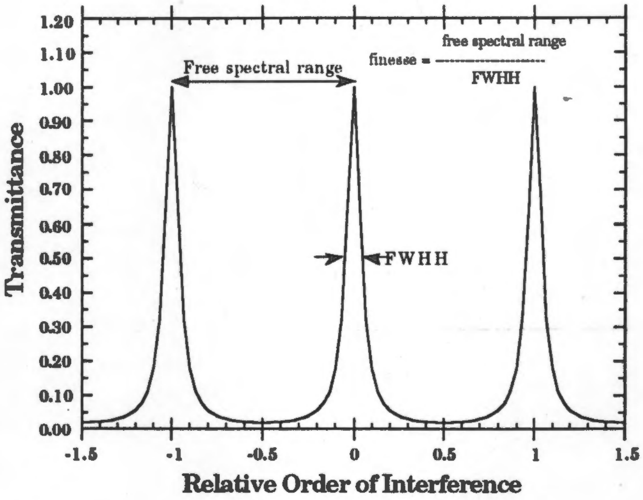

Fig. 11. Transmission function of the Fabry-Perot.

with L the loss per plate (absorption and scattering), R is the plate reflectivity, and M is the order of interference. Equation (13) describes periodic transmission function, as shown in Fig. 11. This figure illustrates some very important terms that are useful to understand the discussion that follows. The separation between peaks is known as the free spectral range and depends inversely on the spacing between the plates; large spacing means a small free spectral range. The full width at half height is the resolution of the instrument, and the ratio of the free spectral range to the resolution is the finesse. The finesse is the number of resolution elements that can fit in between two resonance peaks. It is a dimensionless measure of the "quality" of the device. In the absence of any defects, the finesse is related only to the reflectivity. For example, a reflectivity of 0.80 gives a finesse of 14, and a reflectivity of 0.90 gives 30. In the presence of defects, the finesse for a given reflectivity will be less than that specified by the reflectivity and the peak transmittance will be lower. Careful attention must be given to defects when a Fabry-Perot system is designed or the finesse and throughput will be much less than anticipated. From an examination of Fig. 11 and from this discussion it is seen there are two ways to achieve a high resolution. First, the finesse can be made large, but this is limited to what the technology can provide. It is possible to find small etalons that in the visible have finesses up to 50, but for larger etalons that must survive a journey to space the possible finesse is typically much lower, approximately 15–20. Some engineering effort in improving techniques for mounting etalons could probably increase this value. The second way to increase resolution is to decrease the free spectral range by making the gap large. This also has practical limits. To our knowledge, no etalon has been constructed with a gap larger than 30 cm (Rosenberg and Sroga, 1985).

Equation (13) can be written in an equivalent form:

$$T(M)=\left(1-\frac{L}{1-R}\right)^2\left(\frac{1-R}{1+R}\right)\left(1+2\sum_{n=1}^{\infty}R^n\cos 2\pi nM\right). \qquad (14)$$

Although not immediately apparent, Eq. (14) is the inverse Fourier transform of the Fourier transform in Eq. (13). Equation (14) is the preferred form of the Airy function in this study because it allows easy convolutions with broadening functions.

The order of interference M is

$$M = 2\mu t\nu\cos\theta, \tag{15}$$

where μ is the index of refraction of the material between the plates, t is the effective separation of the plates (for the purposes considered here, it is the same as the physical separation), ν is the wavenumber of light, and θ is the angle of incidence in the Fabry-Perot cavity. It is useful to consider perturbations of t, ν and θ from a set of standard conditions and normal incidence:

$$t = t_0 + \Delta t \tag{16}$$

$$\nu = \nu_0 + \Delta\nu \tag{17}$$

$$\cos\theta = 1 - \frac{\theta^2}{2}. \tag{18}$$

So the order of interference can be written

$$M = 2\mu t_0\nu_0 + 2\mu t_0\Delta\nu + 2\mu\nu_0\Delta t - 2\mu t_0\nu_0\frac{\theta^2}{2}, \tag{19}$$

where only the first order terms have been kept. We let

$$M = M_o + \Delta M \tag{20}$$

where

$$M_0 = 2\mu t_0\nu_0 \tag{21}$$

and

$$\Delta M = 2\mu t_0\Delta\nu + 2\mu\nu_0\Delta t - 2\mu t_0\nu_0\frac{\theta^2}{2}. \tag{22}$$

The quantity $1/2\mu t_0$ is the change in wavenumber required to change the order of interference by one and is defined as the free spectral range, $\Delta\nu_{FSR}$. ΔM then becomes

$$\Delta M = \frac{\Delta\nu}{\Delta\nu_{FSR}} - \frac{\nu_0}{\Delta\nu_{FSR}}\frac{\theta^2}{2} + 2\mu\nu_0\Delta t. \tag{23}$$

Without loss of generality we can require M_0 to be an integer and therefore $T(M) = T(\Delta M)$.

We first consider the effects of thickness variations on the etalon transmission. These variations are inevitable and have various sources. There are large-scale bowing and distortions of the Fabry-Perot plates due to manufacturing, coating and mounting processes. There are microscopic variations in thickness as a result of manufacturing and coating. There are models to describe each of these effects (Hays and Roble, 1970; Hernandez, 1966). Here we assume the variations from the mean follow a Gaussian distribution such that the probability of a deviation δt is

$$P(\delta t) = \frac{1}{\sqrt{\pi}\,\Delta t_e} e^{-\frac{\delta t^2}{\Delta t_e^2}}. \tag{24}$$

This probability function is convolved with the Airy function to give

$$T(\Delta\nu,\theta) = \left(1 - \frac{L}{1-R}\right)^2 \left(\frac{1-R}{1+R}\right)\left[1 + 2\sum_{n=1}^{\infty} R^n e^{-4\pi^2 n^2 \nu^2 \Delta t_e^2} \cos 2\nu n\left(\frac{\Delta\nu}{\Delta\nu_{FSR}} - \frac{\nu_0}{\Delta\nu_{FSR}}\frac{\theta^2}{2}\right)\right]. \tag{25}$$

We make a simplification in notation which allows a more compact representation. Let

$$\begin{aligned} A_n &= \left(1 - \frac{L}{1-R}\right)^2 \left(\frac{1-R}{1+R}\right) && \text{for } n = 0 \\ &= \left(1 - \frac{L}{1-R}\right)^2 \left(\frac{1-R}{1+R}\right) R^n e^{-4\pi^2 n^2 \nu^2 \Delta t_e^2} && \text{for } n > 1 \end{aligned} \tag{26}$$

so the Airy function can be written

$$T(\Delta\nu,\theta) = \sum_{n=0}^{\infty} A_n \cos 2\pi n\left(\frac{\Delta\nu}{\Delta\nu_{FSR}} - \frac{\nu_0}{\Delta\nu_{FSR}}\frac{\theta^2}{2}\right). \tag{27}$$

The Fabry-Perot collects light over a finite range of angles. A larger range of angles implies more light can be collected, but this serves to broaden the signal (lower the resolution) and can be considered, in some respects, to be a defect term. The trade-off between resolution and light gathering ability is an important design consideration. The transmittance of a single channel of a Fabry-Perot system which collects light from angles $\theta_o - \Delta\theta$ to $\theta_o + \Delta\theta$ can be written

$$T(\Delta\nu,\theta_o,\Delta\theta) = \frac{\int_{\theta_o - \frac{\Delta\theta}{2}}^{\theta_o + \frac{\Delta\theta}{2}} T(\Delta\nu,\theta)\theta d\theta}{\int_{\theta_o - \frac{\Delta\theta}{2}}^{\theta_o + \frac{\Delta\theta}{2}} \theta d\theta}, \tag{28}$$

where we have assumed the angles are small which is a very good approximation for the systems we are considering here. This equation can be readily evaluated to give:

$$T(\Delta\nu,\theta_o,\Delta\theta) = \sum_{n=0}^{\infty} A_n \cos 2\pi n\left[\frac{\Delta\nu}{\Delta\nu_{FSR}} - \frac{\nu_0}{2\Delta\nu_{FSR}}\left(\theta_o^2 + \frac{\Delta\theta^2}{4}\right)\right] \operatorname{sin c}\left(\frac{\pi n \nu_o \theta_o \Delta\theta}{\Delta\nu_{FSR}}\right), \tag{29}$$

where sinc(x) = sin(x)/x. This can be simplified by recognizing the number of channels per free spectral range (also known as the aperture finesse) is given by:

$$N_{FSR} = \frac{\Omega_{FSR}}{\Omega_{channel}} = \frac{\Delta\nu_{FSR}}{\nu_o \theta_o \Delta\theta}. \tag{30}$$

Using this and noting that the j^{th} channel is

$$j = \frac{\left(\theta_{o,j}^2 + \frac{\Delta\theta_j^2}{4}\right)}{\theta_o \Delta\theta}, \tag{31}$$

gives the following equation for the Fabry-Perot:

$$T(\Delta\nu, j) = \sum_{n=0}^{\infty} A_n \cos 2\pi n\left(\frac{\Delta\nu}{\Delta\nu_{FSR}} - \frac{j}{N_{FSR}}\right) \sin c\left(\frac{\pi n}{N_{FSR}}\right). \tag{32}$$

This derivation assumes each channel covers the same wavelength interval.

The number of counts, N_{laser}, sensed by any channel of a detector is given by the convolution of the Fabry-Perot instrument function as given by Eq. (32), and the spectral return is given by Eq. (2) multiplied by appropriate instrument constants. This operation gives:

$$\begin{aligned} N_{laser}(j) = {} & \frac{P_T \lambda}{hc} O_A(r) \frac{A_T \Delta h}{4\pi r^2} T^2(r) \frac{Q T_{op} T_f(\nu)}{n_c} \\ & \cdot \sum_{n=0}^{\infty} A_{1,n} \cos\left\{\left(\frac{2\pi n}{\Delta\nu_{FSR}}\right)\left(\nu_1 - \nu_0 - \frac{\nu_1 U}{c} \sin\phi - \frac{j\Delta\nu_{FSR}}{N_{FSR}}\right)\right\} \\ & \cdot \exp\left[-\frac{\pi^2 n^2}{\Delta\nu_{FSR}^2}\left(\Delta\nu_1^2 + \Delta\nu_T^2\right)\right] \cdot \sin c \frac{\pi n}{N_{FSR}} \\ & \cdot \left[P_A(\pi, r)\beta_a(r) \exp\left(\frac{-2\pi\alpha_A n}{\Delta\nu_{FSR}}\right) + P_m(\pi, r)\beta_m(r) \exp\left\{\frac{-\pi^2 n^2 \Delta\nu_G^2}{\Delta\nu_{FSR}^2}\right\}\right], \end{aligned} \tag{33}$$

where Q is the detector quantum efficiency, T_{op} is the transmittance of the optics, exclusive of the etalons, and n_c is the number of channels in the detector, h is Plank's constant, c is the speed of light, and λ is the wavelength of light. The quantity T_f is the transmittance of the filter and any additional etalons.

The total number of counts on each channel is due not only to laser counts but also to the signal from detector thermal noise, read noise (if using a CCD), and a solar contribution. The total number of counts is then

$$N(j) = N_{laser}(j) + N_{Dark}(j) + N_{solar}(j) + N_{read}(j). \tag{34}$$

The solar signal is given by:

$$N_{solar}(j) = \frac{A_T \Omega_T Q T_{op} \Delta t}{n_c} \frac{\lambda B_{sun}}{hc} \int_0^{\infty} T_F(\nu) T_{12}(\nu) d\nu, \tag{35}$$

with A_T the telescope area, Ω_T the telescope field of view in solid angle (which must be at least as great as the laser divergence in order to collect all of the laser light), B_{sun} the solar brightness, Δt the total integration time which is related to Δh and the number of shots added by

$$\Delta t = \frac{2h \sec\phi n_{shots}}{c}, \tag{36}$$

where ϕ is the nadir angle of observation. The integral can be minimized by properly choosing the gaps of the additional etalons (see Skinner et al., 1987).

3.1.3. WIND ERROR

3.1.3.1. Wind error calculation. The wind analysis procedure consists of determining the shift in position of the returned signal relative to the reference laser signal. A least squares fitting applied to Eq. (33) can be used to determine the velocity as well as other parameters of interest, such as β_A, β_m, and $\Delta\nu_G$ (which is related to temperature). The process is to linearize N with respect to the quantities to be fit followed by standard least squares routines which can determine the parameters and their uncertainties (Bevington, 1969; Pless et al., 1989). The linearized form of N can be written

$$\begin{aligned} N(j,U,\beta_A,\beta_m,\Delta\nu_G) &= N(j,U_0,\beta_{A0},\beta_{mo},\Delta\nu_{G0}) \\ &+ \left.\frac{\partial N}{\partial U}\right|_{U_0}(U-U_0) + \left.\frac{\partial N}{\partial \beta_A}\right|_{\beta_{A0}}(\beta_a-\beta_{a0}) + \left.\frac{\partial N}{\partial \beta_m}\right|_{\beta_{m0}}(\beta_m-\beta_{m0}) \\ &+ \left.\frac{\partial N}{\partial \Delta\nu_G}\right|_{\Delta\nu_{G0}}(\Delta\nu_G-\Delta\nu_{G0}). \end{aligned} \tag{37}$$

From Eq. (33) the derivatives can be determined analytically, but their form provides no insight and we shall not display them here.

Of interest to this study is the determination of the wind error and a simple description of the method to determine the error is presented here. It is important to note that winds are essentially independent of the other parameters, and the error derived here is identical to that obtained by least square methods (or any number of other algorithms). The analysis assumes that the wind velocities are small enough that the signal at the j^{th} channel in the presence of a wind can be related to the unshifted line by

$$N_j(U) = N_j(0) + \frac{\partial N_j}{\partial \nu}\frac{2\nu}{c}U\sin\phi, \tag{38}$$

where N_j is number of photons counted in the j^{th} channel, ν is the laser wavenumber, and U is the effective line-of-sight wind speed associated with the Doppler shift of the backscattered signal. For purposes of error analysis, it is assumed that $N_j(0)$ is known and that errors are uncorrelated. The wind speed is found from a least-squares fit using the equation

$$U = \frac{\dfrac{c}{2\nu\sin\phi}\displaystyle\sum_{j=1}^{n_c}\frac{N_j(U)-N_j(0)}{\sigma_j^2}\frac{\partial N_j}{\partial\nu}}{\displaystyle\sum_{j=1}^{N}\left(\frac{\partial N_j}{\partial\nu}\right)^2\frac{1}{\sigma_j^2}}, \tag{39}$$

where σ_j^2 is the variance of N_j. Poisson statistics are applicable in determining σ_j so that $\sigma_j^2 = N_j$. The variance, $(\delta U)^2$, associated with the measurements is determined by using the propagation of errors theorem and is given by

$$(\delta U)^2 = \frac{c^2}{4\nu^2\sin^2\phi\displaystyle\sum_{j=1}^{n_c}N_j\left(\frac{1}{N_j}\frac{\partial N_j}{\partial\nu}\right)^2}. \tag{40}$$

We can further understand the characteristics of Eq. (40) if we note that the counts are the sum of the signal (N_{laser}) and noise sources (N_{noise}) (which can be due to detector noise, solar radiation background and the like):

$$N_j = N_{j,laser} + N_{j,noise}. \tag{41}$$

Since the noise has no dependence on wavenumber:

$$\frac{\partial N_j}{\partial\nu} = \frac{\partial N_{j,laser}}{\partial\nu}. \tag{42}$$

This allows the error equation to be written in a form that explicitly allows signal and noise to be considered in the variance of the horizontal line of sight:

$$(\delta U)^2 = \frac{c^2}{4\nu^2\sin^2\phi\displaystyle\sum_{j=1}^{n_c}\left[\left(\frac{N_{j,laser}^2}{N_{j,laser}+N_{j,noise}}\right)\left(\frac{1}{N_{j,laser}}\frac{\partial N_{j,laser}}{\partial\nu}\right)^2\right]}. \tag{43}$$

The signal to noise ratio (SNR) is a very useful concept which can readily be incorporated into these equations. The signal is simply $N_{j,laser}$, and the variance of $N_{j,laser}$ is

$$\sigma_j^2 = N_{j,laser} + N_{j,noise}. \tag{44}$$

So the SNR is

$$(S/N) = \frac{N_{j,laser}}{\left(N_{j,laser}+N_{j,noise}\right)^{\frac{1}{2}}}. \tag{45}$$

If the noise term is 0, then S/N = $\sqrt{N_{j,laser}}$, which is a familiar form. The error equation can then be written

$$(\delta U)^2 = \frac{c^2}{4\nu^2 \sin^2\phi \sum_{j=1}^{n_c}\left[(S/N)_j^2\left(\frac{1}{N_{j,\text{laser}}}\frac{\partial N_{j,\text{laser}}}{\partial \nu}\right)^2\right]}. \tag{46}$$

We illustrate the nature of Eqs. (40) or (46) by considering a simple example. We consider a spectrum which is an Airy function (i.e. a δ source function convolved with a perfect Fabry-Perot). This Airy function has a finesse of 15 and projects one order onto a detector which has 32 channels. We examine the error as a function of peak counts and noise. Figure 12 shows the results of this simulation. In Fig. 12(a) we show the error as a function of peak counts for various noise levels. The thick solid line on the left is the error if no noise were present. As the lines progress to the right the noise is 0.03, 0.1, 0.3, 1.0, 3.0, 10.0, 30.0, 100.0, 300.0 counts per channel. We note that most of the information about the Doppler shift comes from the sides of the line where the signal is about half of its maximum

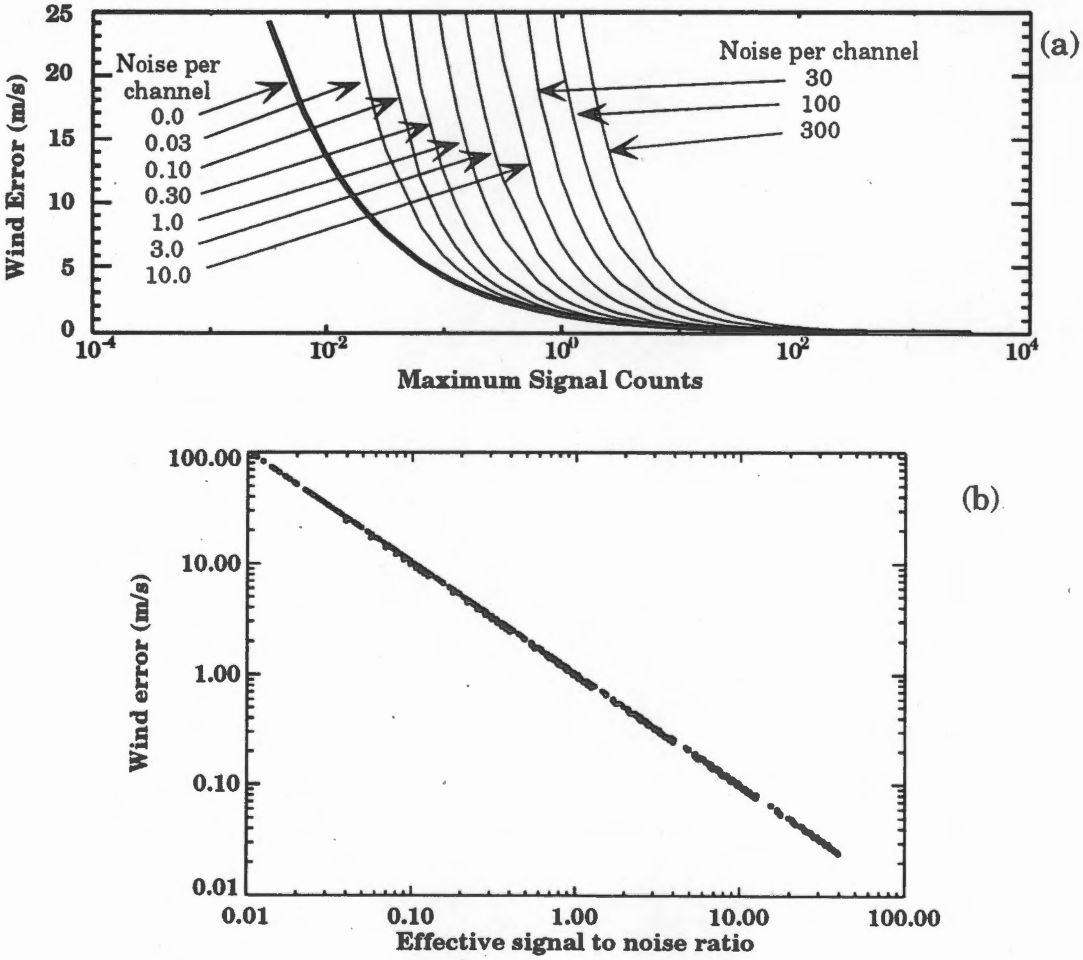

Fig. 12. Simulated wind error. (a) Wind error as a function of count level and noise. (b) Wind error as a function of effective signal to noise ratio.

value (see Fig. 6). Although the SNR is different on each channel, we can define the S/N at this point as the effective SNR, which is

$$(S/N)_{\mathrm{eff}} = \frac{N_{j\mathrm{max,laser}}}{\sqrt{2}\left(N_{j\mathrm{max,laser}} + 2N_{\mathrm{noise}}\right)^{\frac{1}{2}}}, \tag{47}$$

where $N_{j\mathrm{max,laser}}$ is the maximum number of counts from the laser source. Figure 12(b) shows the error as a function of the effective SNR. All of the data now fall along one line, demonstrating the usefulness of this approach.

3.1.3.2. *Idealized wind error calculation.* We now examine an idealization that is useful to understand some of the fundamental features of errors with an incoherent detector. We assume the only source of photons to be from the laser (no dark or read noise, no solar photons), and the spectral shape of the signal to be Gaussian:

$$N_j = \frac{N_o e^{-\frac{\Delta\nu_j^2}{\Delta\nu_e^2}} \delta\nu}{\sqrt{\pi}\Delta\nu_e}, \tag{48}$$

where N_o is the total number of detected photons, $\delta\nu$ is the width of the spectral channel, $\Delta\nu_j$ is the distance from line center for channel j, and $\Delta\nu_e$ is the 1/e width of the distribution. The derivative of this with respect to wavenumber is

$$\frac{\partial N_j}{\partial \Delta\nu} = \frac{-2\Delta\nu_j N_j}{\Delta\nu_e^2}. \tag{49}$$

So that for this case the variance [see Eq. (40)] can be written

$$\delta U^2 = \frac{c^2 \Delta\nu_e^4}{16\nu^2 \sin^2\phi \sum_{j=1}^{n_c} N_j \Delta\nu_j^2}. \tag{50}$$

If we let the channel width decrease and the number of channels increase to keep the spectral coverage constant we can replace the sum by an integral. If the range covered by the detector is greater than the effective width of the line, then it can be solved analytically and the standard deviation of the wind error becomes

$$\left(\delta U^2\right)^{\frac{1}{2}} = \frac{c\Delta\nu_e}{4\nu \sin\phi \sqrt{N_o}} = \frac{c\Delta\nu_e}{4\nu \sin\phi (S/N)}. \tag{51}$$

This is identical to the result obtained by Gagné et al. (1974) except for a factor a 2 that is obtained when using an active system such as a lidar.

3.1.3.3. *Summary of incoherent wind errors.* Equation (51) and Eq. (46) show several fundamental properties concerning the wind error:

1. The wind error decreases linearly with the width of the spectral feature.
2. In the absence of noise from sources other than the laser signal, the error increases as the inverse of the square root of the signal; e.g. a factor of 4 decrease in signal increases the error by a factor of 2. In the presence of other

noise sources (read noise, solar radiation, dark count, etc.) the error increases at a faster rate.

3. There exists no threshold below which a wind estimate cannot be made.
4. The errors cannot be characterized by SNR considerations alone, since often a reduction of SNR is more than made up for by an increase in sharpness of the signal.
5. Doppler shifts can be measured which are much smaller than the instrument resolution. This often misunderstood point is really the result of semantics. The classical definition of resolution asks the question, "How close together can two identical spectral features be before my instrument loses the ability to determine there are two spectral features?", which is a completely different question than "How well can I determine the shift of spectral feature?", which is the question Doppler shift measurements answer.

The difficulty in designing a system is that the spectral width and signal level are not independent parameters. We will consider this further in a later section.

3.1.3.4. *Zero location.* The measurement of the Doppler shift requires a knowledge of the position of the spectral feature in the absence of a wind component [$N_j(0)$ in Eq. (39)]. There are several ways to gain this information. As the laser is fired a very small fraction of the light will be directed into the receiving system. This will provide a reference for the entire system. Because of the spacecraft velocity and the Earth's rotation it may not be adequate to provide a true zero position to the desired accuracy. However, it will provide excellent knowledge of the laser and detector stability.

On average, the Earth is about 50% cloud covered, so about 1 out of 2 pulses will hit the surface and provide a strong return. Since the velocity of the surface is well known, this will provide an absolute zero reference. This knowledge will be combined with the stability infomation from the laser reference to provide zero wind positions over cloudy areas.

There are several hundred radiosondes launched approximately twice daily from locations all over the globe. A statistical study using this data will validate the above procedure, allow for the determination of any systematic errors, and confirm the statistical error analysis.

3.1.3.5. *Measurement and observational error for an incoherent system.* An important consequence of the noise characteristics of the incoherent systems is the ability to average several lower quality measurements into one with higher quality. This can be used to reduce the total error in the wind measurement (including measurement and atmospheric variances). A useful measure of the observation variance is (Emmitt, private communication, 1993)

$$\delta U_o^2 = \frac{\delta U^2}{PN_1} + \frac{\delta U_s^2}{PN_2} + \delta U_g^2, \qquad (52)$$

where δU_o^2 is the total uncertainty of a horizontal component of the wind within a target volume, δU^2 is the variance in the measurement (discussed above), δU_s^2 is the total variance of the winds on all scales less than 2L (L=side dimension of the target volume), δU_g^2 are errors associated with incoherent averaging of the sample volume, N_1 is the number of independent shots to reduce δU^2, N_2 is the number of shots effective in reducing δU_s^2, and P is the fraction of shots that pass a "goodness" test. With an incoherent system all measurements add information, so P=1. The system can be readily designed so each measurement observes a difference section of the sample volume, so $N_1 = N_2 = N$. The overall error is then

$$\delta U_o^2 = \frac{\delta U^2 + \delta U_s^2}{N} + \delta U_g^2. \tag{53}$$

If we assume δU_g is very small, then additional measurements collected with an incoherent system will always drive the uncertainty down. This may not be the case for a coherent system.

3.1.4. THROUGHPUT CONSIDERATIONS

The lidar detection system must use all of the light collected by the telescope for maximum efficiency. In this section we discuss some of the considerations and how throughput impacts the design of the incoherent system.

Here we define the throughput (or étendue), L, of an optical element as the product of the element area, A, and the solid angle cone of light, Ω, passing through the element:

$$L = A\Omega. \tag{54}$$

First we consider the throughput for the collecting telescope. The area is simply the collecting area of the primary, and for small angles the solid angle is related to the telescope field of view by

$$\Omega = \pi\theta_T^2, \tag{55}$$

where θ_T is the half angle field of view of the telescope. Of course, one of the necessary requirements of the telescope is that

$$\theta_T \geq w_1, \tag{56}$$

with w_1 the divergence of the laser. This insures that the telescope field of view is large enough to view the entire laser illuminated spot. The throughput for the telescope is then

$$L_T = \left(\frac{\pi D_T \theta_T}{2}\right)^2. \tag{57}$$

The derivation of the throughput for the etalon is similar, except now the angle is related to the wavelength range, and consequently to the dynamic range of the system. From Eq. (23) we get the relationship between angle and wavenumber range as

$$\frac{\Delta\nu}{\nu_0} = \frac{\theta_e^2}{2}. \tag{58}$$

We can consider $\Delta\nu$ to be the wavenumber interval in the cone angle described by θ_e. Also, the Doppler equation gives

$$\frac{\Delta\nu}{\nu_0} = \frac{2U_R}{c}, \tag{59}$$

where U_R is the velocity dynamic range. Consequently, we have

$$\theta_e^2 = \frac{4U_R}{c} \tag{60}$$

and

$$L_e = \frac{\pi^2 D_e^2 U_R}{c}. \tag{61}$$

Since the two throughputs must be equal,

$$\frac{D_T^2\theta_T^2}{4} = \frac{D_e^2 U_R}{c}. \tag{62}$$

A value of U_R = 50 m/s is the smallest practical value for a system required to measure winds in the atmosphere, and 800 m/s corresponds to roughly the width of the molecular scattered signal. A practical upper limit to the size of an etalon is 15 cm, so a dynamic range of 50 m/s requires that the telescope field of view and the laser divergence be less than 0.12 mr given a telescope diameter of 1 m. The acceptable divergence increases as the square root of the dynamic range, so if the dynamic range is increased to 200 m/s the laser divergence can be as large as 0.25 mr.

This shows the relationship between some fundamental parameters. To get the maximum sensitivity to winds we want U_R to be as small as possible. A practical lower limit is 50 m/s since the atmosphere can have winds on the order of ±25 m/s. As U_R decreases the etalon diameter must increase. Similarly, if we want to increase θ_T, which may be desired to make a laser operating at 532 nm "eye safe," the etalon diameter must again increase. Table 3 shows some relationships between θ_T and D_e for various values of U_R with the diameter of the telescope fixed at 1 meter.

Table 3. Relationship between etalon diameter, laser beam divergence, and velocity dynamic range

Telescope half angle fov (mr)	Etalon Diameter		
	U_R=50 m/s (cm)	U_R=200 m/s (cm)	U_R=800 m/s (cm)
0.05	6.1	3.1	1.5
0.10	12.2	6.1	3.1
0.15	18.4	9.2	4.6
0.20	24.5	12.2	6.1
0.25	30.6	15.3	7.7
0.30	36.7	18.4	9.2

These considerations also have implications for the etalon gap thickness and consequently the system resolution. The wavenumber interval covered by the instrument, $\Delta\nu$, can be expressed as a fraction of the etalon free spectral range:

$$\Delta\nu = \varepsilon\Delta\nu_{FSR} = \frac{\varepsilon}{2t}, \tag{63}$$

where ε is the fraction of an order observed. We substitute this into Eq. (59) and rearrange to find

$$\varepsilon = \frac{4t\nu U_R}{c}. \tag{64}$$

Table 4 shows the values of ε for various values of t and U_R.

Table 4. Fraction of order observed.

	U_R					
	50m/s		**200m/s**		**800m/s**	
t (cm)	**355 nm**	**532 nm**	**355 nm**	**532 nm**	**355 nm**	**532 nm**
1.00	1.88×10^{-2}	1.25×10^{-2}	7.51×10^{-2}	5.01×10^{-2}	3.00×10^{-1}	2.00×10^{-1}
2.00	3.76×10^{-2}	2.51×10^{-2}	1.50×10^{-1}	1.00×10^{-1}	6.00×10^{-1}	4.01×10^{-1}
3.00	5.64×10^{-2}	3.76×10^{-2}	2.25×10^{-1}	1.50×10^{-1}	9.01×10^{-1}	6.02×10^{-1}
3.33					1.00×10^{0}	
4.99						1.00×10^{0}
5.00	9.39×10^{-1}	6.27×10^{-2}	3.76×10^{-1}	2.51×10^{-1}		
10.00	1.88×10^{-1}	1.25×10^{-1}	7.51×10^{-1}	5.01×10^{-1}		
13.31			1.00×10^{0}			
15.00	2.82×10^{-1}	1.88×10^{-1}		7.52×10^{-1}		
19.95				1.00×10^{0}		
20.00	3.76×10^{-1}	2.51×10^{-1}				
25.00	4.69×10^{-1}	3.13×10^{-1}				
30.00	5.63×10^{-1}	3.76×10^{-1}				
35.00	6.57×10^{-1}	4.39×10^{-1}				
40.00	7.51×10^{-1}	5.01×10^{-1}				
45.00	8.45×10^{-1}	5.64×10^{-1}				
50.00	9.39×10^{-1}	6.27×10^{-1}				
53.25	1.00×10^{0}					
55.00		6.89×10^{-1}				
60.00		7.52×10^{-1}				
65.00		8.15×10^{-1}				
70.00		8.77×10^{-1}				
75.00		9.40×10^{-1}				
79.80		1.00×10^{0}				

3.1.5. EYE SAFETY

Eye safety is an important consideration for lidar systems, particularly for incoherent systems which tend to operate near visible wavelengths.

The issue of eye safety must be approached from two directions: first, it must be determined how much laser light is dangerous, and second, the exposure dose must be calculated.

The first issue concerns the determination of the maximum permissible exposure (MPE). This requires a knowledge of the laser wavelength, pulse duration, pulse repetition frequency (prf), and other optical conditions. Most, but not all, of the relationships are spelled out in ANSI standard on the safe use of lasers (ANSI, 1993; OSHA, 1991). What assumptions should be made concerning optically aided viewing (e.g., size of binoculars or telescope) are not covered in that document.

The second issue requires knowledge of satellite altitude, laser power, prf, beam divergence, and atmospheric properties. Again, important parameters concerning atmospheric propagation, particularly scintillation, are not covered in the ANSI standard. For the discussion here we follow rules that are similar to those used by the LITE system (McCormick et al., 1993; Couch et al., 1991). We assume the following (Winker, private communication, 1994):

1) An observer may be viewing the laser with 10 x 50 binoculars.
2) Scintillation effects may increase the energy by a factor of 5.

Figure 13 shows the MPE for a single pulse as a function of wavelength for two pulse lengths that bracket the practical limits (5 ns and 500 ns). This clearly shows the relative value of working in the IR or in the near UV compared to 532 or 1064 nm. A pair of 10x50 binoculars increases the flux on the eye by approximately a factor of 100 and scintillation by a factor of 5, so the actual MPE for a single pulse is reduced by 500.

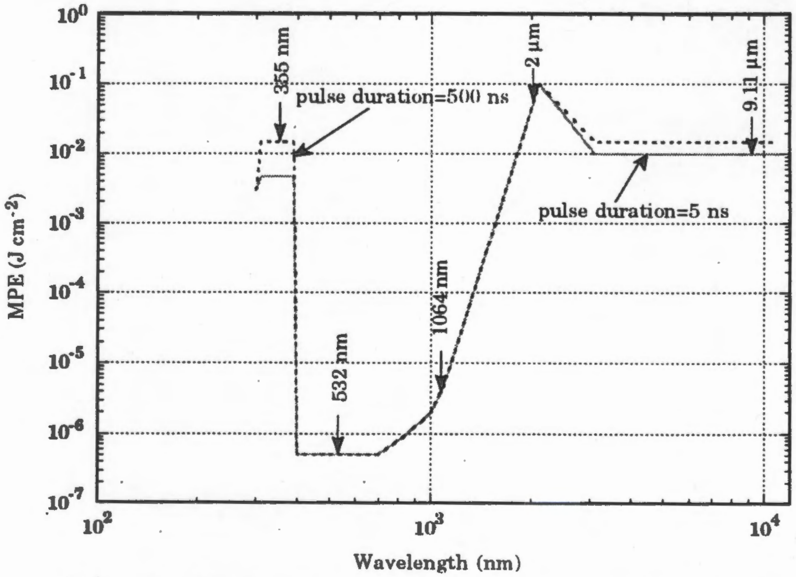

Fig. 13. Maximum permissible exposure (MPE) for single laser pulses.

In order to estimate the brightness of the laser as seen from the ground, we assume a flat Earth. The laser beam is assumed to have a Gaussian angular profile

$$P(\Delta\phi) = \frac{2P_T}{\pi w^2} e^{-\frac{2\Delta\phi^2}{w^2}}, \qquad (65)$$

where P is the power per solid angle, P_T is the total pulse energy, w is the $1/e^2$ angle of the beam, and $\Delta\phi$ is the angle from the center of the beam. If the satellite is at altitude h above the surface and viewing an angle ϕ_0 from the nadir, the distribution on the surface is

$$P(\Delta x, \Delta y) = \frac{2P_T}{\pi w^2 h^2 \sec^3 \phi_0} e^{\frac{2}{-w^2 h^2 \sec^2 \phi}\left(\frac{\Delta x^2}{\sec^2 \phi_0} + \Delta y^2\right)}, \tag{66}$$

where Δx is the distance from the center of the beam along the direction of the beam and Δy is perpendicular to it (see Fig. 14). This equation assumes w is sufficiently small so that the distance from the satellite to the surface is independent of where the observer is in the beam. According to this, the brightest spot in the beam is directly in the center, and is given by

$$P(0,0) = \frac{2P_T}{\pi w^2 h^2 \sec^3 \phi_0}. \tag{67}$$

The effective edge of the beam can be defined as the location where the strength falls to $1/e^2$ from the maximum. This defines an ellipse with major and minor axes of

$$\Delta x_w = 2wh \sec^2 \phi_0 \tag{68}$$

$$\Delta y_w = 2wh \sec \phi. \tag{69}$$

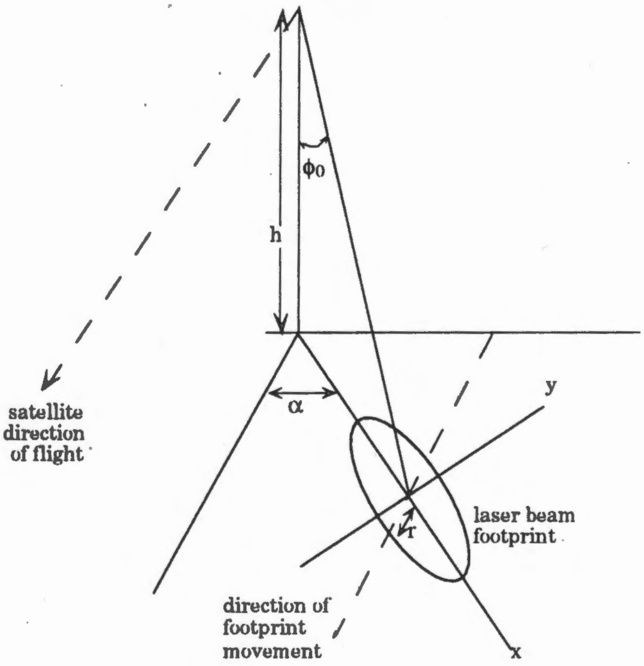

Fig. 14. Viewing geometry for eye safety calculations.

In order to calculate the MPE for a pulsed laser it is necessary to know the number of pulses observed. We first find the length of the footprint that passes through the center of the ellipse. This will provide the worst case estimate. This path length is

$$r = \frac{2wh \sec^2 \phi_0}{\left(\sec^2 \phi_0 \sin^2 \alpha + \cos^2 \alpha\right)^{1/2}}, \tag{70}$$

where α is the azimuth angle of observation (α=0 is looking along the direction of flight). The time to cover this path is $t = r/V_{sat}$. If the prf is n Hz, then the number of pulses seen, k', is

$$k' = \frac{2nwh \sec^2 \phi_0}{V_{sat}\left(\sec^2 \phi_0 \sin^2 \alpha + \cos^2 \alpha\right)^{1/2}}. \tag{71}$$

Since the number of pulses seen must be an integer, we round k' up to the next integer:

$$k = \text{int}(k'+1). \qquad (72)$$

The MPE for a train of k pulses is reduced from the single pulse MPE by

$$\text{MPE}(k) = k^{-1/4}\text{MPE}(1). \qquad (73)$$

Note that there are three factors which make this calculation a worst case one. First, atmospheric attenuation is ignored. This could reduce the exposure by ~2 at 532 nm. Second, the maximum exposure is used to represent the exposure everywhere inside the footprint. Third, the maximum possible time is used to estimate the exposure. Thus, besides the factors of 500 for aided viewing and scintillation effects, these factors give an additional safety margin to the eye-safety calculation.

Now consider an example. Let λ=532 nm, prf=1 kHz, power=20 W (20 mJ/pulse), ϕ_0=45°, α=45°, w=0.1 mrad, pulse duration=1μs, and h=350 km. From Eq. (71) we find the number of pulses to be 15.24, or, rounded up, 16 pulses. The MPE for a single pulse is 5 x 10^{-7} Jcm^{-1}, and for the pulse train

$$\text{MPE}(16) = \left(16^{-1/4}\right)\left(5\text{x}10^{-7}\right) = (0.5)\left(5\text{x}10^{-7}\right) = 2.5\text{x}10^{-7}\ \text{Jcm}^{-2}. \qquad (74)$$

Further, this MPE must be reduced by a factor of 100 for the optical aid, giving the effective MPE of $2.5\text{x}10^{-9}$ Jcm^{-1}.

The flux at the beam center is

$$P(0,0) = \frac{2P_T}{\pi w^2 h^2 \sec^3 \phi_0} = 3.7\text{x}10^{-10}\,\text{Jcm}^{-2}. \qquad (75)$$

This needs to be multiplied by 5, which is the scintillation factor, giving a maximum flux of 1.9 x 10^{-9} Jcm^{-2}. This is 75% of the MPE and demonstrates that this laser system would be eye safe.

We now consider in more detail lasers operating at 1064, 532 and 355 nm. The laser is assumed to have an output power of 20 W, and the satellite is placed at 350 km altitude. Figure 15 shows the MPE and exposure for a prf of 1 Hz (solid), 10 Hz (dotted), 100 Hz (dashed), and 1000 Hz (long dashed) as a function of laser divergence angle for a laser operating at 355 nm. As the divergence angle increases the exposure decreases as the beam is

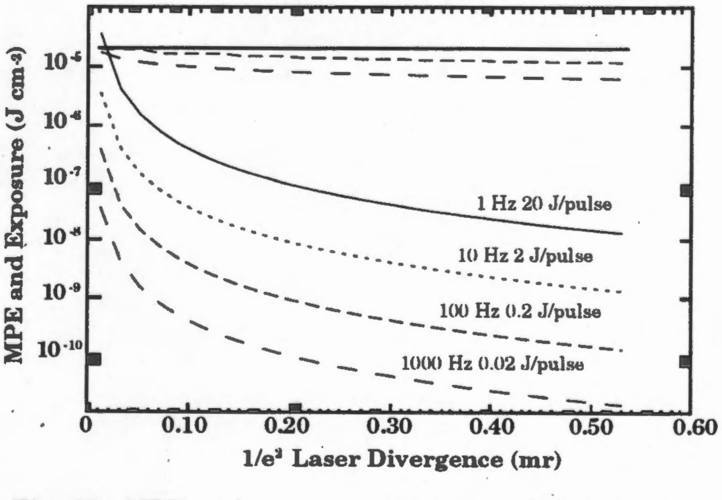

Fig. 15. MPE and exposure at 355 nm. Aided viewing factor 100, scintillation factor 5.0, laser power 20.0 W, satellite altitude 350 km, pulse length 100 ns.

spread out. The MPE also reduces slightly since there are more pulses that would be observed. Figure 16 shows the safety margin (exposure/MPE) for the same cases. Only for an extremely narrow pulse is this laser even remotely eye hazardous. At 0.2 mr even a single pulse of 20 J has a safety margin of ~100. Although carried out for a laser at 355 nm, this result would hold for any laser that operates below 400 nm. Other lasers that have been proposed for this spectral region, such as XeCl at 308 nm, Raman shifted XeCl at 350 nm, or frequency double Alexandite, would all be eye safe.

Figure 17 shows the safety margin for 532 nm. With a 20 W laser, prfs of 1 and 10 Hz do not provide an eye safe condition at reasonable divergence angles. A 100 Hz system becomes eye safe at ~0.23 mr, and a 1000 Hz system at 0.08 mr. This clearly shows a system at 532 nm can be made eye safe by either increasing the prf or increasing the divergence angle.

Figure 18 shows the safety margin for 1064 nm. A single pulse only comes close to safety at divergencies in excess of 0.5 mr. A 10 Hz system is eye safe at 0.20 mr and a 100 Hz system is safe at about 0.06 mr. The conclusion of this study is that even in the most sensitive region (~532 nm) it is possible to make a laser eye-safe by the proper choice of divergent angle and prf. There is a significant cost to doing this, however. Increasing the prf and divergence angle will increase the contamination by solar radiation. The impact of this will be demonstrated later.

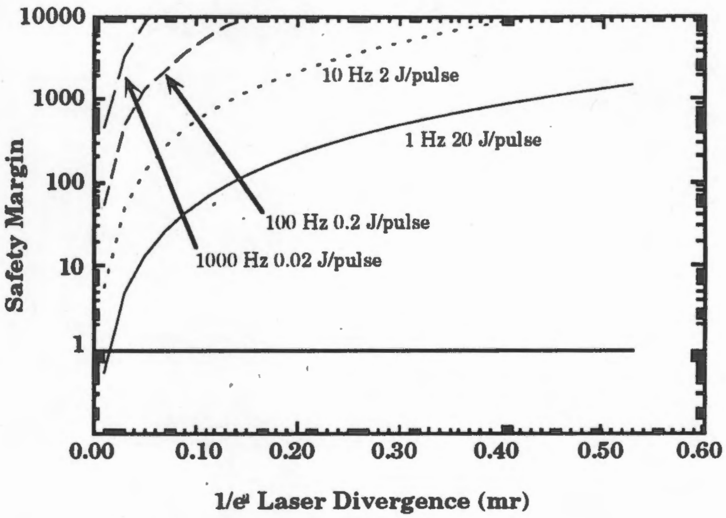

Fig. 16. Eye safety calculation at 355 nm. Aided viewing factor 100, scintillation factor 5, laser power 20.0 W, satellite altitude 350 km, pulse length 100 ns.

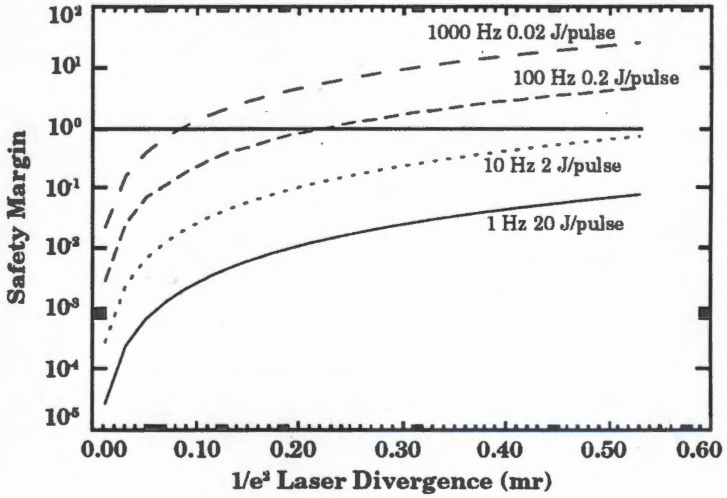

Fig. 17. Eye safety calculation at 532 nm. Aided viewing factor 100, scintillation factor 5, laser power 20.0 W, satellite altitude 350 km, pulse length 100 ns.

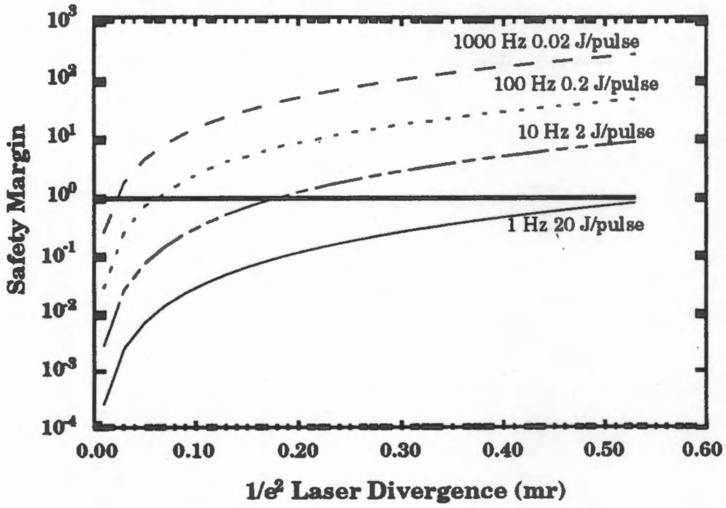

Fig. 18. Eye safety calculation at wavelength 1064 nm. Aided viewing factor 100, scintillation factor 5.0, laser power 20.0 W, satellite altitude 350 km, pulse length 100 ns.

3.1.6. LASER PROPERTIES

In this section we outline some of the fundamental requirements a laser must meet to operate an incoherent system.

3.1.6.1. *Laser pulse length.* The pulse length has two major influences on the lidar performance. The first influence concerns vertical resolution in the atmosphere. The line-of-sight resolution for a pulse of length Δt is

$$\Delta x = \frac{c}{2}\Delta t. \tag{76}$$

The second issue concerns the spectral width of the laser signal. From the uncertainty principle, the smallest width is related to pulse duration by

$$\Delta f \Delta t \approx \frac{1}{2\pi}, \tag{77}$$

where Δf is the spectral width in Hertz (this is known as a transform limited laser). The width in wavenumber units is

$$\Delta \nu = \frac{1}{2\pi c \Delta t}. \tag{78}$$

Table 5 shows the values of Δx and Δν for various pulse lengths assuming we can achieve the transform limited condition. This shows that very short pulses (less than about 30 ns) have widths that are large compared to the desired spectral width for an aerosol signal. For example, at 355 nm a free spectral range is equivalent to a dynamic range of ± 25 m/s when the gap is 53 cm. With a finesse of 10, the etalon width is equivalent to a shift of ~5 m/s. This is equivalent to a 6 ns pulse. Since for optimal operation the laser should be much smaller than the etalon width, a reasonable lower limit for the laser pulse is 30 nm. This does not apply for observations of the Rayleigh signal. The width of the Rayleigh scattered line is ~500 m/s and the laser width is not a critical consideration.

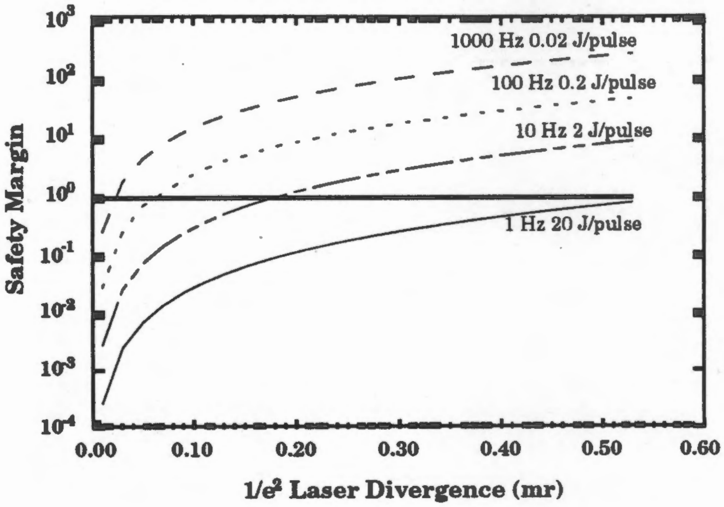

Fig. 18. Eye safety calculation at wavelength 1064 nm. Aided viewing factor 100, scintillation factor 5.0, laser power 20.0 W, satellite altitude 350 km, pulse length 100 ns.

3.1.6. LASER PROPERTIES

In this section we outline some of the fundamental requirements a laser must meet to operate an incoherent system.

3.1.6.1. *Laser pulse length.* The pulse length has two major influences on the lidar performance. The first influence concerns vertical resolution in the atmosphere. The line-of-sight resolution for a pulse of length Δt is

$$\Delta x = \frac{c}{2}\Delta t. \tag{76}$$

The second issue concerns the spectral width of the laser signal. From the uncertainty principle, the smallest width is related to pulse duration by

$$\Delta f \Delta t \approx \frac{1}{2\pi}, \tag{77}$$

where Δf is the spectral width in Hertz (this is known as a transform limited laser). The width in wavenumber units is

$$\Delta \nu = \frac{1}{2\pi c \Delta t}. \tag{78}$$

Table 5 shows the values of Δx and $\Delta \nu$ for various pulse lengths assuming we can achieve the transform limited condition. This shows that very short pulses (less than about 30 ns) have widths that are large compared to the desired spectral width for an aerosol signal. For example, at 355 nm a free spectral range is equivalent to a dynamic range of ± 25 m/s when the gap is 53 cm. With a finesse of 10, the etalon width is equivalent to a shift of ~5 m/s. This is equivalent to a 6 ns pulse. Since for optimal operation the laser should be much smaller than the etalon width, a reasonable lower limit for the laser pulse is 30 nm. This does not apply for observations of the Rayleigh signal. The width of the Rayleigh scattered line is ~500 m/s and the laser width is not a critical consideration.

Table 5. Resolution and spectral width for various pulse lengths.

$\Delta t(s)$	$\Delta x(m)$	$\Delta\nu(cm^{-1})$	Δf	$\Delta U(m/s)$ 532 nm	$\Delta U(m/s)$ 355 nm
1×10^{-9}	1.5×10^{-1}	5.3×10^{-3}	159 MHz	42	28.3
3×10^{-9}	4.5×10^{-1}	1.8×10^{-3}	53	14	9.4
1×10^{-8}	1.5×10^{0}	5.3×10^{-4}	16	4.2	2.8
3×10^{-8}	4.5×10^{0}	1.8×10^{-4}	5.3	1.4	0.9
1×10^{-7}	1.5×10^{1}	5.3×10^{-5}	1.6	0.4	0.3
3×10^{-7}	4.5×10^{1}	1.8×10^{-5}	530 kHz		
1×10^{-6}	1.5×10^{2}	5.3×10^{-6}	159		
3×10^{-6}	4.5×10^{2}	1.8×10^{-6}	53		
1×10^{-5}	1.5×10^{3}	5.3×10^{-7}	16		
3×10^{-5}	4.5×10^{3}	1.8×10^{-7}	5.3		
1×10^{-4}	1.5×10^{4}	5.3×10^{-8}	1.6		

The usual requirement for a space-borne lidar is a vertical resolution of approximately 1 km. The length of the laser pulse should be much shorter than this, say 100 m. This states that the pulse duration should be no more than 1 μs or so. In summary, we have

$$30\ \text{ns} < \Delta t < 1\mu\text{s} \qquad \text{aerosol lidar,} \tag{79}$$

$$0.1\ \text{ns} < \Delta t < 1\mu\text{s} \qquad \text{molecular lidar.} \tag{80}$$

3.1.6.2. *Pulse repetition frequency*. The pulse repetition frequency of the laser should be such that there is no interference between pulses. That is, as a pulse enters a region of significant scatter, the last bit of the previous pulse should have already left the scattering region. If h_{max} represents the maximum height of effective scatterers, then pulses must be separated by at least

$$\Delta t = \frac{2h_{max}}{c\cos\phi}, \tag{81}$$

with ϕ the observation angle from nadir. Table 6 shows Δt for various values of h_{max} and ϕ.

Table 6. Minimum time for adequate pulse separation (seconds).

	ϕ (degrees)				
h_{max} (km)	40	45	50	55	60
25	2.2×10^{-4}	2.4×10^{-4}	2.6×10^{-4}	2.9×10^{-4}	3.3×10^{-4}
50	4.4×10^{-4}	4.7×10^{-4}	5.2×10^{-4}	5.8×10^{-4}	6.1×10^{-4}
75	6.5×10^{-4}	7.1×10^{-4}	7.8×10^{-4}	8.7×10^{-4}	1.0×10^{-3}

The conclusion is that the prf has an upper limit of about 1 kHz. If the lidar is used in a region where eye safety is an issue then the laser should be operated at a prf that is as close to this as possible. Otherwise, the prf can be determined by other factors.

3.1.6.3. *Lag angle.* The lag angle, α, for an azimuth observation angle ψ and satellite velocity U_S is

$$\alpha = \frac{U_s \sin\psi}{c}. \tag{82}$$

For an observation angle of 45° and a satellite velocity of 7.5 km/s the lag angle is 1.8×10^{-2} mr. Since for an incoherent system the laser divergence would be on the order of 0.1 to 0.2 mr, the lag angle is at least a factor of 5 smaller. This small effect can be incorporated by making the telescope field of view slightly larger than the laser divergence or by small movements of the telescope.

3.1.6.4. *Speckle.* Speckle is a very important effect for coherent systems, but is insignificant for incoherent systems. The radius of a speckle cell, $r_{speckle}$, is of the order (Dainty, 1984)

$$r_{speckle} = \frac{3.832R\lambda}{\pi D}, \tag{83}$$

where R is the distance from the scattering source to the receiver, λ is the wavelength of light, and D is the diameter of the illuminated spot at the scatterer. The size of the spot is proportional to the laser beam divergence, giving

$$r_{speckle} = \frac{1.916\lambda}{\pi w}, \tag{84}$$

where w is the $1/e^2$ divergence of the laser. For a laser divergence on the order of 0.1 mr and a wavelength of 355 nm, the speckle size is ~2.2 mm. A 1 meter diameter telescope has on the order of 2.1×10^5 speckle cells, which should be more than sufficient to average out any intensity variations. This is a direct consequence of the fact that the incoherent system does not require diffraction limited optics and the divergence of the beam can be relatively large. It is still not large compared to the scale of the wind field. A 0.1 mr divergence at a distance of 500 km provides a spot of ~50 m.

3.2. Description of Coherent Lidar

The use of coherent detection for radar returns has a long history of successful application to the observation of motions in the atmospheric. This history naturally has led to a branch of lidar research that uses the same basic principles developed for radar, but applied to the aerosol return from lasers of various basic frequencies. The recently proposed development of space-borne coherent laser radars is the topic of this subsection. It is our intention to describe here the space-borne coherent lidar system in a clear fashion which will allow direct comparison between the incoherent and the coherent systems with less confusion than has been present in past attempts at this intercomparison.

The principle advantage of the coherent system is the possibility of detection that is shot-noise limited at long wavelengths where the number of photons for a given pulse power is maximum. However, this apparent advantage of the heterodyne system of detection at long wavelengths is complicated by the increase of the cross section for scattering at shorter wavelengths. These issues are now addressed by summarizing the relationships which determine the coherent lidar system's SNR and the resulting accuracy with which the velocity of a scattering volume can be determined. These factors are taken from a series of studies described in the summaries of Zrnic (1979), Thomson and Boynton (1977), Kane et al. (1984), and Huffaker et al. (1984).

3.2.1. COHERENT SYSTEM SIGNAL TO NOISE RATIO

The system SNR is a very important parameter in determining the Doppler shifts with a coherent lidar system. The literature is rather cluttered with diverse notation in describing this quantity and we will attempt to keep the jargon to a minimum. The notation used here is the same as that used throughout this report, but will differ from that used in the literature since there is no single standard for conventional use. The expression given here is taken from Thomson and Boynton (1977) as reported by Huffaker et al. (1984) and Frehlich and Kavaya (1991):

$$\mathrm{SNR} = \frac{A_0 J \eta_0 \eta_d Q_e \beta c \tau S \exp\left(-2\int_0^R \mu(R')dR'\right)}{2h\nu\left[R^2\left(1+\frac{A_0}{\pi\rho_n^2}\right)+\left(\frac{A_0}{\lambda}\right)^2\left(1-\frac{R}{f}\right)^2\right]}. \tag{85}$$

Here the symbols mean the following:

A_0 = area of the main telescope (m^2)
c = speed of light (m/sec)
C_n^2 = refractive-index structure parameter ($m^{-2/3}$)
D = telescope diameter (m)
f = focal distance (m)
$h\nu$ = photon energy (Joule)
J = transmitted pulse energy (Joule)

L = effective length of the turbulent field (m)
Q_e = detector quantum efficiency
R = range to the scattering volume (m)
ρ_a = turbulence induced transverse-field coherence radius which is related to the refractive-index structure parameter as described in Appendix III
S = distribution function for speckle fluctuations
SNR = narrow band signal to noise ratio of the heterodyned signal
β = atmospheric backscatter coefficient ($m^{-1}sr^{-1}$)
λ = wavelength of the laser light (m)
μ = atmospheric absorption coefficient (m^{-1})
η_0 = efficiency of the total optical system
η_d = efficiency of the detector system including the beam shape factor and heterdyne efficiency, here we use a total detector efficiency of 0.46
τ = pulse duration (sec)

In this expression several points should be made regarding factors which reduce the system efficiency.

Heterodyne Efficiency — The angular shape of the beam and the matching of the local oscillator are taken from Huffaker et al. (1984) but are very system dependent. This and the beam shape compensation factor are often smaller than the value quoted by Huffaker, however, we will use that estimate.

Optical Efficiency — The receiver optical efficiency used here is also based on estimates by Huffaker et al. (1984) and will be summarized in the table of system parameters (see Table 12). We have choosen to separate the detector quantum efficiency as a separate term to facilitate the comparison with the incoherent lidar system. The transmitter efficiency will be absorbed into the laser power required to produce the required transmitter power.

Turbulence — Turbulent fluctuations in the optical path from the transmitter to the scattering volume and back to the receiver are a serious problem (Smith, 1993; Frehlich, 1993) for shorter wavelength coherent lidars operating within the atmosphere. However, when the lidar is operating from space the phase front distortion of the transmitted beam is partially compensated for in the return beam by the scattering volume, and turbulence does not seriously influence the wavefront shape over the telescope area. In general, we find that the tranverse-field coherence length is large compared to the telescope diameter for the longer wavelength lidar at 9.1 microns. There is some question about the influence of turbulence in the first 1 kilometer of altitude inside the boundary layer. Some calculations show very small coherence length under varying meteorological conditions. See Appendix III for a model calculation of the coherence length.

Speckle — The effect of the target being diffuse and incoherent is significant on the short-term return from a laser radar. This phenomenon, known as speckle, produces a strongly modulated power distribution at the distance of the receiver. The long-term averaged return, i.e. over many shots, is not effected by this process. The number of photons received from a single shot of the lidar can be very strongly modulated. The degree of modulation over the receiving telescope is the critical measure of the effect on the lidar return. For a circular illumination of diameter D the autocorrelation function for the return signal can be approximated (Dainty, 1984) by the relationship

$$R_I\,(r) = \langle I\rangle^2\left[1+\left|2\frac{J_1\left(\frac{\pi Dr}{\lambda R}\right)}{\frac{\pi Dr}{\lambda R}}\right|^2\right] \tag{86}$$

where the scale of the speckle pattern is determined by the first zero of the bessel function, that is where $r=3.832R\lambda/\pi D$. Here R is the range and λ the wavelength of the coherent laser radiation illuminating the scattering volume. It is interesting to note that for heterodyne detection where the system must be diffraction limited the characteristic size of the speckle pattern is always equal to the telescope diameter. The consequence of this fact is that there will be a strong modulation of the coherent return due to the influence of speckle. This is not true for incoherent detection where the beam divergence can be much larger than the diffraction limit. The return signal for the coherent lidar is a Rayleigh distributed random variable. That is, the speckle factor that was introduced in the signal equation is obtained from the Rayleigh distribution

$$P(S) = \exp(-S), \tag{87}$$

where P is a uniformly distributed number between 0 and 1 with the speckle factor given by $S=-\log(P)$. Note that the effect of speckle can be to enhance the return or to reduce its value. Of course, the average of S is unity.

This condition is known as fading in conventional rf radars. It has a very important influence on the probability of detection and on the occurance of false alarms in the coherent lidar system when operating near the threshold of detection. The influence of speckle on the incoherent lidar system is normally not very important.

Probability of Detection — The coherent system is different in principle from the incoherent technique in that detection of a signal is usually equivalent to making the desired measurement of line-of-sight wind speed. This is because the individual frequency filters are sufficiently narrow that detection within one filter range is an accurate observation of velocity. However, it is necessary to detect the signal above the noise due to statistical variation in the local oscillator, the system background noise, and other sources of random signal fluctuations. There is a question of what criterion should be used to select when a signal has been detected above the noise. A unique relationship (Fox, 1993) exists between the detection probability, the narrow band signal to noise, and the resulting probability of a false detection, or probability of a false alarm.

$$P_d = \frac{1}{\pi}\int_{V_T}^{\infty} x\,\exp\left[-\frac{1}{2}\left(x^2+A^2\right)\right]\left\{\int_0^{\pi}\exp[xA\cos(y)]dy\right\}dx, \tag{88}$$

where

P_d = probability of detection
A = $(2\,\mathrm{SNR})^{1/2}$
V_T = $[-2\ln(P_{fl})]^{1/2}$
P_{fl} = probability of a false alarm.

This relationship can be approximated adequately under most circumstances with the following equation

$$P_d = \frac{1}{2}\left\{1 + \mathrm{erf}\left[\sqrt{\frac{1}{2} + \mathrm{SNR}} - \sqrt{\ln\left(\frac{1}{P_{fl}}\right)}\right]\right\}. \quad (89)$$

This probability must be evaluated each time a detection is attempted for an accurate simulation of the response of the coherent lidar system. We have incorporated this factor into the model used to simulate the coherent lidar system.

3.2.2. ESTIMATION OF LINE-OF-SIGHT VELOCITY ERRORS

The velocity of the scatterers along the line of sight is, in principle, very simply determined from the coherent laser radar. The frequency of the laser light is Doppler shifted during the scattering process and results in a heterodyned signal that has a frequency distinct from that of the return from an object that is at rest. This shift is uniquely related to the line-of-sight velocity and as such makes the estimation of velocity very simple. However, there are, as always, complications in this simple description. Noise in the detection process, small scale turbulent motions in the atmosphere, laser frequency broadening due to pulse length and jitter, errors in knowledge of pointing angle, and lack of sufficient signal return all contribute to uncertainty in our ability to determine the frequency of the heterodyned signal. These questions have been discussed extensively in the coherent radar literature and have been summarized by Zrnic (1979). We present a modified version of that error analysis for the pulse pair algorithm as described by Thomson and Boynton (1977) and published by Kane et al. (1984). The error is shown to depend primarily on the wide band signal to noise ratio ($\mathrm{SNR_w}$) of the heterodyned return signal and is give by

$$\sqrt{\overline{\delta U^2}} = \frac{1}{4\pi}\left(\frac{\lambda U_{max}}{NL\tau}\right)^{1/2}\left[2\pi^{3/2}W + \frac{16\pi^2 W^2}{\mathrm{SNR_W}} + \frac{1}{\mathrm{SNR_W^2}}\right]^{1/2}. \quad (90)$$

Here the symbols mean the following

f = sampling frequency of the electronics (sec^{-1})
L = ratio of the length of the range gate to the length of a pulse
N = number of shots averaged
$\mathrm{SNR_W}$ = wide band signal to noise ratio of the heterodyned signal
= $\sqrt{2\pi}\,W\,\mathrm{SNR}$
τ = duration of the transmitted pulse (sec)
$\sqrt{\overline{\delta U^2}}$ = root mean squared velocity error (cm/sec)

U_{max} = maximum unaliased velocity that can be determined by the Nyquist criterion, fλ/2 (cm/sec)

U_{atmos} = velocity variation of the atmosphere due to small-scale turbulence and wind shear

U_{bw} = equivalent laser frequency spread due to the finite length of the transmitted pulse, λ/4πt

W = frequency spread of the returned signal in relation to the maximum frequency of the detectable signal.

$$= \frac{\sqrt{U_{bw}^2 + U_{atmos}^2}}{U_{max}}$$

The MathCad document to calculate the predicted output from a coherent lidar system is given in Appendix IV. This document also illustrates the variation of the signal to noise and shows the distribution of errors in that result from observing the velocity with a fixed aerosol density. We will use this basic calculation to determine the errors and detections probability under realistic conditions in the terrestrial atmosphere.

3.2.3. TYPICAL OBSERVATIONS AND ERRORS

The formalism developed above is used to examine the distribution of errors for the coherent lidar described in Table 12 in section 5 where the incoherent and coherent lidars are compared. Here we show the altitude variation of signal to noise and velocity error associated with the various aerosol profiles that we have discussed previously. The computations carried out in this section as described in Appendix V. Figure 19 shows a typical signal return for a series of 100 random shots into an atmosphere that represents the median density of aerosols in the boundary layer, free troposphere, and stratosphere. The velocity error plot illustrates the strong influence of speckle, the loss of information when the detection is not achieved, and the very accurate observation when detection is achieved. This example is typical of the coherent lidar observation. Here the detection in the planetary boundary layer is excellent, with a very poor sampling within the free troposphere, and very adequate sampling of the lower stratosphere. This is characteristic of most aerosol profiles. The aerosol distribution over the southern oceans have much lower scattering in the middle troposphere. A simulation of this aerosol-depleted region is shown in Fig. 20 where very poor detection is achieved. Unfortunately, this low scattering is very likely over much of the southern hemisphere. Much higher aerosol distributions are observed over the northern continential areas. The simulation for this situation (see Fig. 21) exhibits exceptional accuracy. These figures illustrate the extreme variability that is encountered over the surface of the Earth. A complete study of the variability would require knowledge of the global distribution of aerosol scattering in the three populations which we have used to characterize the aerosol profiles. This is not possible within the constraints of this study. However, we can illustrate the implications of these variations on the observations of winds with a give lidar power.

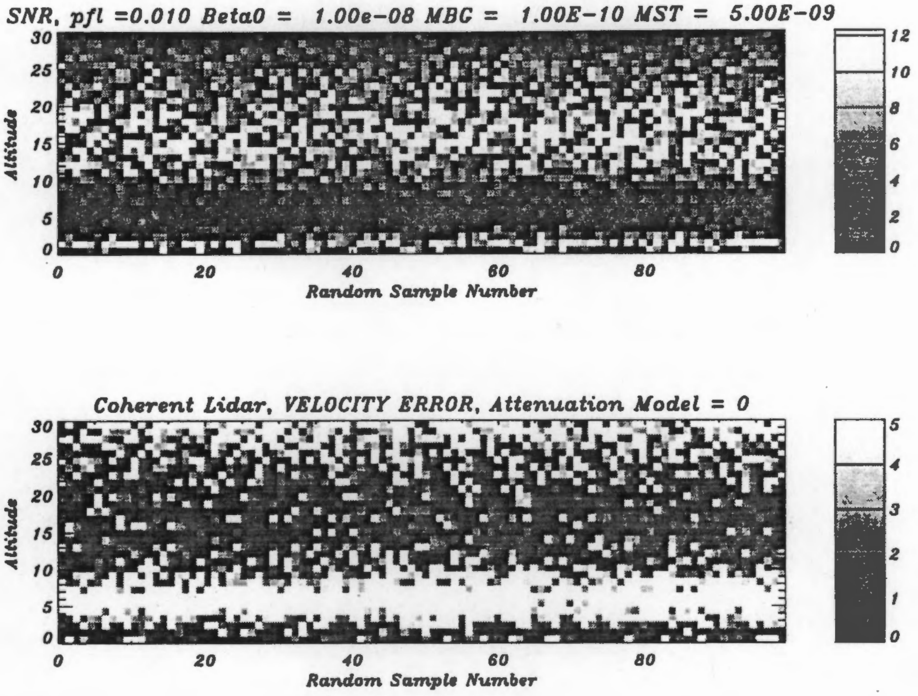

Fig. 19. Coherent lidar SNR and velocity error for global average aerosol distribution.

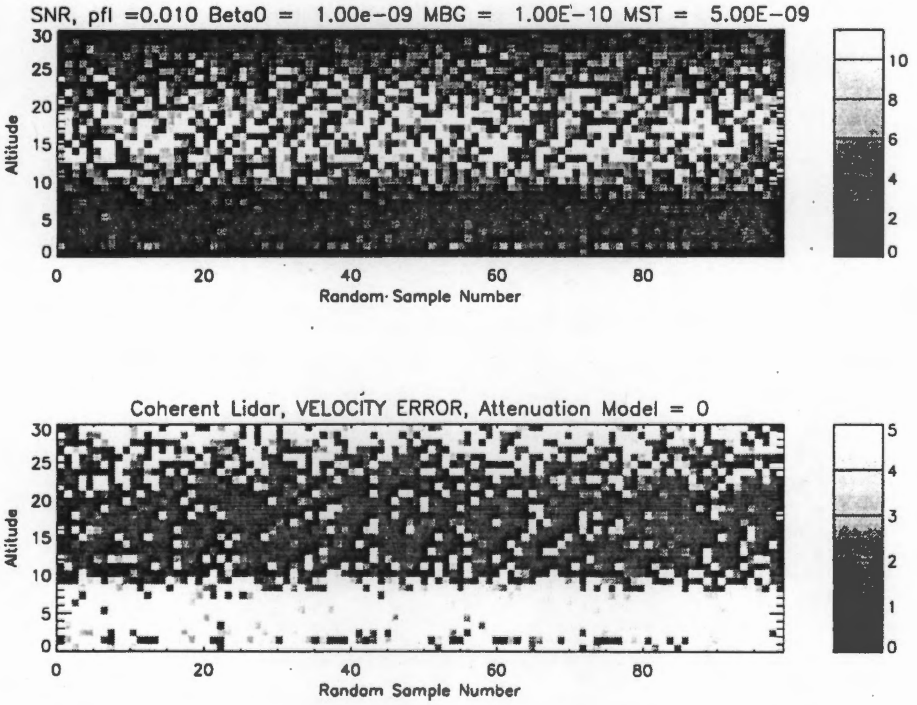

Fig. 20. Coherent lidar SNR and velocity error for southern hemisphere oceanic aerosol distribution.

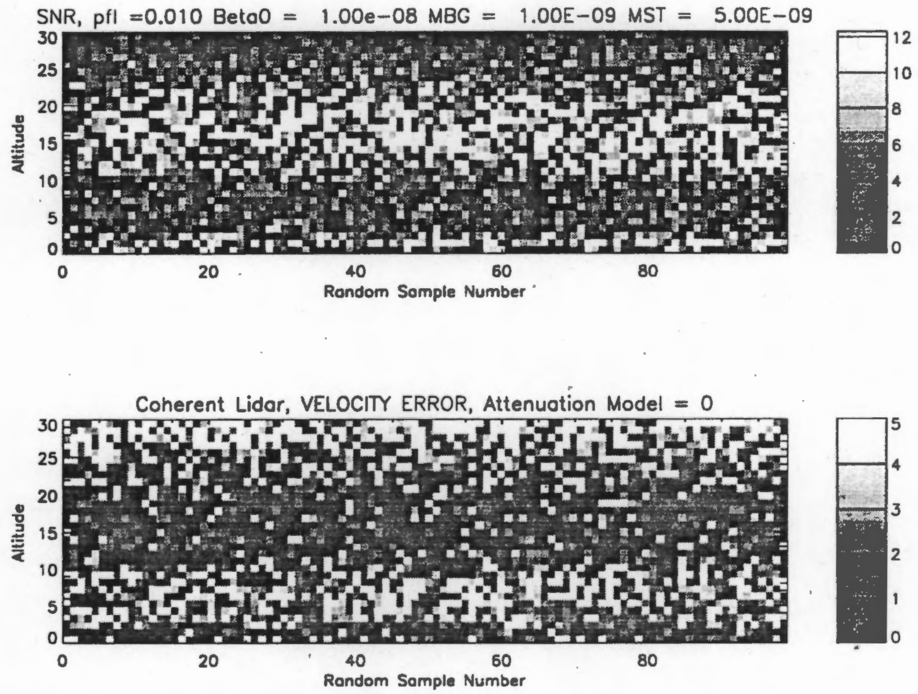

Fig. 21. Coherent lidar SNR and velocity error for northern continental aerosol distribution.

3.2.4. POWER REQUIREMENTS

The coherent lidar is inherently a nonlinear sampling device due to the discrete nature of the detection probability and the influence of speckle. This causes some difficulty is estimating the true power required to achieve a particular accuracy profile within the atmosphere. There are several possible approaches to this issue, but for simplicity we have selected two distinct approaches which give very similar results in the end.

3.2.4.1. *Optimal estimation of wind speed.* At any given altitude the estimates of accuracy on an individual lidar shot will vary considerably due to the influence of speckle. If speckle causes a low signal, then there is a good probability that the shot may not exceed the threshold of detection, and if the speckle enhances the signal there is usually a very high probability of a good observation. The problem here is to decide how many shots on an average are necessary to achieve the desired accuracy of measurement. We begin by considering the situation where the lidar energy is fixed and we ask how many shots must be averaged in order to achieve the desired accuracy. This is a very simple problem, but must be considered rather carefully. The line-of-sight variance of the observation is the proper quantity to consider in this case. We know that the variance of a set of observations which have different variance is given by the expression

$$\overline{\sigma}^2 = \left[\sum_{i=1}^{M} \frac{1}{\sigma_i^2}\right]^{-1}. \tag{91}$$

However, this is not necessarily the correct formula to apply since measurements with low variance will dominate in the sum and bias it towards small values. We choose to limit the variance to the minimum desired value. That is, if a measurement has variance less than or equal to the desired variance then the observation has been achieved. Under these conditions the number of shots required to achieve the desired accuracy is given by

$$N = \left[\frac{1}{M}\sum_{i=1}^{M} \frac{\sigma_{\text{desired}}^2}{\max\left(\sigma_i^2, \sigma_{\text{desired}}^2\right)}\right]^{-1}, \tag{92}$$

where $\max(x_1,x_2)$ means take the larger of x_1 and x_2. Thus, the energy, J, that must be expended to make the observation is simply

$$J = J_o\left[\frac{1}{M}\sum_{i=1}^{M} \frac{\sigma_{\text{desired}}^2}{\max\left(\sigma_i^2, \sigma_{\text{desired}}^2\right)}\right]^{-1}, \tag{93}$$

where J_o is the energy of each laser shot. This expression is simply the result of applying the optimal estimation formula with a threshold applied to the variance. We have used this expression to compare the energy required for the coherent lidar with that required for the incoherent lidar to achieve the same accuracy, an essential comparison.

There is an alternative way to consider this problem based on asking the question what energy would be required to achieve the same goal if only one shot were to be made with higher energy. This question is more difficult, but can be estimated for the coherent system by noting that the energy transmitted and the velocity accuracy are related linearly in the small signal limit. This condition can again be used to estimate the energy requirements of the lidar. Here the difference is just to change from the variance which is the square velocity error to the velocity error in the calculation of the required energy.

In this case the transmitted energy is simply

$$J = J_o\left[\frac{1}{M}\sum_{i=1}^{M} \frac{\sigma_{\text{desired}}}{\max\left(\sigma_i, \sigma_{\text{desired}}\right)}\right]^{-1}. \tag{94}$$

We note that only in situations where the ratio

$$\left[\frac{\sigma_{\text{desired}}}{\max\left(\sigma_i, \sigma_{\text{desired}}\right)}\right]^{P} \tag{95}$$

is substantially different than 0 or 1 will there be a significant difference in the results. The coherent lidar system normally has this ratio equal to 0 or 1.0 and thus the exponent, P, in this expression is of little consequence. That is, there is usually either a detection or a failure to detect, and the details of the process of averaging are of little consequence. This is demonstrated in Figure 22 where these two cases are illustrated for the limiting cases of the aerosol contributions. The computer code for the calculation of the averaged energy required to satisfy a 1 m/sec accuracy throughout the atmosphere is tabulated in Appendix VI. Note that the aerosol profiles used here are for the boundary cases discussed in the comparison section of this report, section 5. Figure 22(a) shows the linear dependence on velocity error and Fig. 22(b) the dependance on the variance of the velocity. It should be noted that these figures differ very little except near the boundary of the free troposphere where there is a rapid variation of detectability with altitude. This small variation is due to the singular nature of detection in the coherent lidar. In future discussions in section 5 we will consider only the case where averaging is based on the variance.

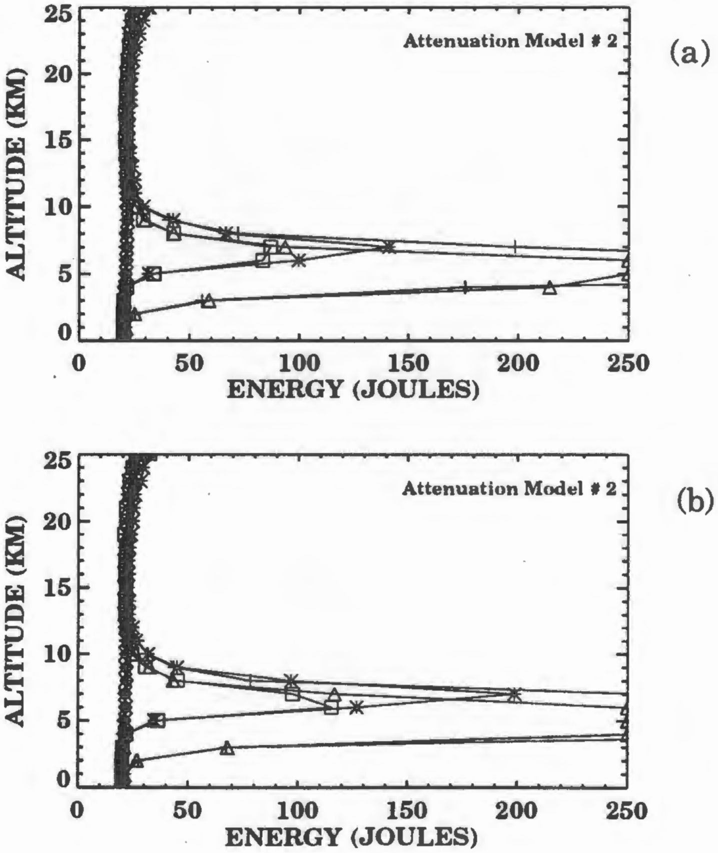

Fig. 22. Linear error and variance dependent energy estimates for a coherent lidar. Coherent lidar energy requirements, E=20 Joule, 1 m/s error, (a) P=1, (b) P=2.

4. Incoherent Lidar Optimization and Performance

The equations of the last section have been incorporated into a detailed model that simulates the complete performance of the incoherent space wind lidar system. The model is a complete end-to-end analysis of the space wind lidar or a ground-based system. Figure 23 outlines the various components of the model. The three major components are 1) the scattering calculations, 2) lidar and detector representation, and 3) error calculation. The scattering section includes only single scattering and keeps track of the amount of laser light scattered by aerosols and molecules as well at the solar contribution. The scattered photons are converted to a detector signal by the lidar equation and Fabry-Perot equations which were discussed previously. The errors are calculated by fitting the calculated spectra with a least squares fitting program. As noted in the section on error analysis, the results of this approach are the same as the analytical equations for wind error described earlier. The outputs of the model are the derived parameters and their errors; here we are concerned with the horizontal wind.

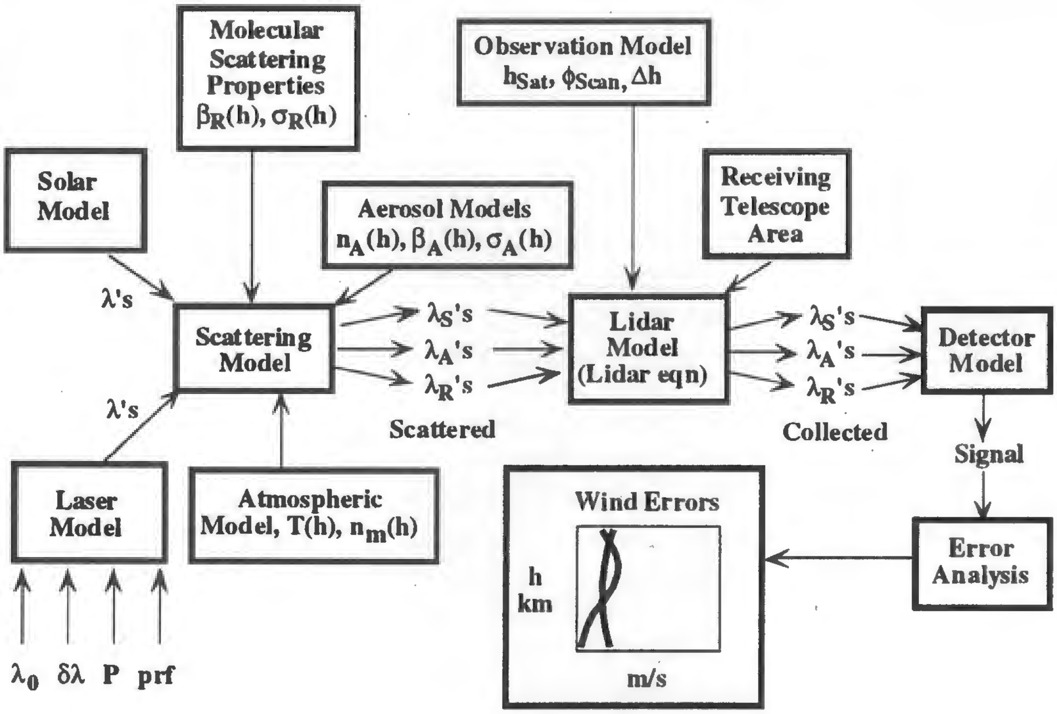

Fig. 23. Space lidar simulation model outline.

Three wavelength regions are considered in this report. The basic laser considered is a Nd:YAG laser with a fundamental wavelength of 1064 nm, which can be frequency doubled to 532 nm and tripled to 355 nm. Other lasers can be considered, but the arguments that apply to the Nd:YAG would also apply to other general spectral regions. The fundamental at 1064 nm is the most efficient since losses due to doubling and tripling are avoided. In addition, because of the longer wavelength this system provides the most photons per watt. On the negative side, detectors at this wavelength are somewhat noisier and eye safety considerations are similar to visible wavelengths. In addition, the molecular scattering is a factor 16 less than at 532 nm and 81 less than at 355 nm. Because of these factors we do not consider 1064 nm further. The doubled frequency at 532 nm avoids the detector problems since there are low noise detectors available at this wavelength that have quantum efficiencies up to ~80%. However, the eye safety issue remains, and in practice this makes 532 nm a difficult system to implement. The tripled frequency at 355 nm falls in a part of the spectrum that is almost completely eye safe. CCD detectors at this wavelength still have good response, with values of quantum efficiency up to 80% (Schaefer et al., 1991). Another consideration is the molecular scattering, which is by far the largest at this wavelength. Due to these considerations, only 532 nm and 355 nm are considered further.

The backscatter signal consists of molecular and aerosol components, each with a difference spectral signature. A system designed to measure winds can use either of these components; to date all studies of space-borne incoherent lidars have used the aerosol return. With the same number of photons, Doppler shift measurements are much more sensitive to aerosol returns because the spectral width is much smaller that molecular scattering. However, the number of photons are not equal. There are many locations and times when the aerosol concentration is quite low (Kent et al., 1983, 1988, 1991; Post and Cupp, 1992; Tratt and Menzies, 1994). These often occur in the free troposphere, and extremely low concentrations occur over southern hemisphere oceans where there is the most notable lack of direct wind observations (radiosondes). Molecular scattering is much more uniform over the surface, even though it is intrinsically less sensitive to Doppler shifts. An ideal system would use the aerosol signal whenever it is available and the molecular signal when it is not. Each of these returns requires a different instrument configuration, and therefore it is necessary to choose one or the other or a multi-channel system.

We consider three types of lidar systems: (1) a system that is optimized to use the aerosol scattering, (2) a system that is optimized to use molecular scattering, and (3) one the uses both. For each of these we consider a system at 355 nm and a system at 532 nm. We begin by discussing how the parameters for the etalon system are determined. There are in practice only two free parameters for the detection system, the etalon gap and finesse (reflectivity). These parameters are constrained as described previously. We use our experience to help determine reasonable values for other system parameters, such as etalon defects and losses. Table 7 shows some of the more important parameters used in our simulations. A telescope diameter of one meter was selected because this is the largest size that is easily accommodated by the current optical fabrication equipment and represents the 'knee' of the cost curve.

Table 7. Incoherent lidar simulation parameters.

Parameter	355 nm	532 nm
Satellite altitude (km)	350	350
Observation zenith angle (deg)	45	45
Laser bandwidth (1/e)	4.1×10^{-5} cm^{-1} 1.2 MHz	4.1×10^{-5} cm^{-1} 1.2 MHz
Etalon defects (1/e)	50 Å	50 Å
Loss per plate	0.01	0.01
Laser power	20 W	20 W
PRF	10 Hz	400 Hz
Integration time	5 s	5 s
Laser divergence (1/e^2)	0.20 mr	0.40 mr
Telescope fov (full)	0.0126°	0.0242°
Number of detector channels	64	64
Quantum efficiency	0.80	0.80
Optical efficiency	0.10	0.10
Telescope diameter	1 m	1 m
Telescope area	7800 cm^2	7800 cm^2

4.1. Lidar System Optimizations

In this section we will discuss the method to optimize a lidar system and the results. We develop eight systems which will be used in the next section to describe the performance. We consider a lidar that is optimized for aerosol and one optimized for molecules. Then we describe a system that combines the best features of each. The optimization procedure is constrained by issues of eye safety and practical limits of engineering. Eye safety forces a system operating at 532 nm to have a much greater laser beam divergence than a system operating at 355 nm. As a consequence, the etalon diameter must be larger. While in the past we have used etalon plates up to 15 cm in diameter, in this work we limit the practical size of the etalon to 10 cm in diameter. This will often not be large enough to match the etendue of the collected light. In that case the only option is to increase the velocity dynamic range of the system.

4.1.1. AEROSOL LIDAR – 355 NM

The optimization of a lidar at 355 nm is relatively simple compared to a lidar at 532 nm because eye safety is not a major concern. Thus, the laser beam divergence can be made whatever size is practical. The optimization need only really concern the etalon gap and reflectivity. Figure 24 shows a contour of the wind errors as a function of reflectivity and gap thickness. The fractional number of orders on the detector is adjusted to project 50 m/s on the detector. This is seen as the minimum dynamic range of a system to avoid ambiguities in the wind recovery. The system optimizes in reflectivity at about 90%. This is somewhat a function of the losses assumed for the system. Smaller values of the loss per plate and etalon defects would have resulted in a higher optimal reflectivity. A value of 90% corresponds to a value that our experience has shown to be a reasonable one. The wind error decrease monotonically as the thickness is increased. At a gap thickness of 53.25 cm the free spectral range corresponds to a dynamic range of 50 m/s. A gap of 53 cm is somewhat larger than we have constructed; the largest has been a 30 cm etalon built in the 1980s for RCA (Rosenberg and Sroga, 1985). We therefore define two systems for further analysis: System A has a gap of 53.25 cm, a reflectivity of ~0.90, and a dynamic range of 50 m/s; System C is the same except the gap is 30 cm.

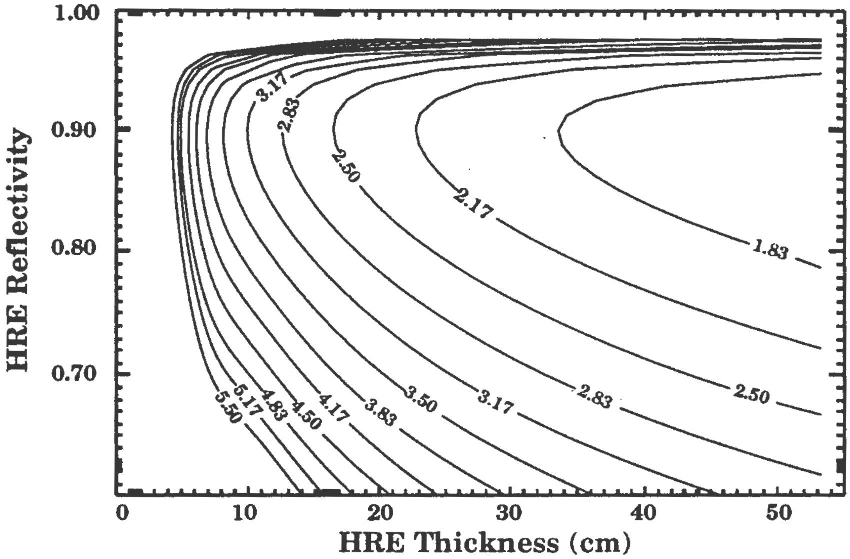

Fig. 24. Wind error (m / s) for an aerosol system as a function of etalon thickness and reflectivity.

4.1.2. AEROSOL LIDAR – 532 NM

The eye safety issue at 532 complicates the optimization somewhat. The eye safety requirements dictate that the laser beam divergence must be at least 0.4 mr (full angle) if we are using the parameters in Table 7. However, the results of this optimization will change significantly if the satellite altitude, laser power, or the prf is altered. Because of the large laser divergence angle, a 10 cm diameter etalon plate could not accept all of the light for a system with a dynamic range of 50 m/s. To meet all of the requirements this needs to be increased to 330 m/s. This merely means that for an etalon with a free spectral range of 50 m/s we are placing 6.6 orders on the detector. With the CLIO and CCD system described earlier multiple orders are readily handled. The etalon gap for a 50 m/s dynamic range at this wavelength is 79.25 cm. The reflectivity that optimizes is again ~0.9. Once more we define two systems: System B with a gap of 79 cm, and System D with a gap of 26.5 cm.

4.1.3. MOLECULAR LIDAR – 355 NM

For the molecular lidars there is an additional consideration besides the etalon gap and reflectivity. We need to consider the spectral interval to place on the detector. The aerosol signal is so narrow that the spectral interval is set by the dynamic range desired in the instrument. The molecular signal is so much wider that this is no longer applicable. The spectral interval on the detector must be large enough to sense a significant fraction of the line shape. The 1/e line width of the molecular line at 355 is ~0.035 cm^{-1}, which is equivalent to a Doppler shift of 186 m/s. We examined dynamic ranges varying from 400 to 1000 m/s. There was relatively little difference, but a small minima existed between 600 and 800 m/s. In such a case, a larger dynamic range is preferable since it will allow easier interpretation of any systematic variations in the spectral signature and we chose to project 800 m/s on the detector. Once the dynamic range is decided the optimization follows the same procedure as before. Figure 25 shows the contour plot of errors as a function of thickness and reflectivity. The optimal etalon thickness is 1.6 cm with a reflectivity of ~0.70. We define this as System E.

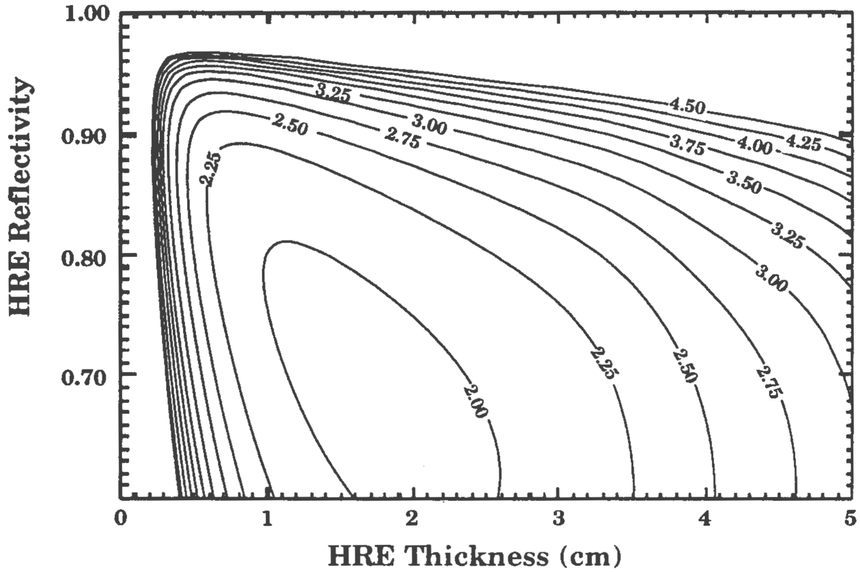

Fig. 25. Wind error (m/s) for a Rayleigh system as a function of etalon thickness and reflectivity.

4.1.4. MOLECULAR LIDAR – 532 NM

The 532 nm molecular system is much easier to define than the 532 nm aerosol system because the increased dynamic range allows a 10 cm diameter etalon to readily collect all of the light. The 1/e width of the molecular signal at this wavelength is about 0.024 cm^{-1}, which corresponds to the same Doppler shift as at 355 nm. Again, we choose a dynamic range of 800 m/s. The optimization for this system, System F gives a gap of 2.2 cm and a reflectivity of ~0.70.

4.1.5. COMBINED SYSTEM

The systems described above examine either the aerosol or molecular return. It is desirable to have a system that uses both returns; the aerosol system will give an excellent wind measurement when there are sufficient aerosols to make a measurement, and a molecular system provides an acceptable measurement in regions of low aerosols. There are a number of ways to implement a combined system. One of the most straightforward is a system that contains both an aerosol and a molecular channel with a scene selector mirror that directs light into one of the two systems. Which of the two systems is to be used could be determined in a number of ways. For example, the areas to use either system can be preprogrammed, e.g. use the molecular system over the ocean areas of the southern hemisphere and use the aerosol system elsewhere. Another control method would use an on-board computer to intelligently decide which system to use. The current return could be analyzed to determine how the next pulse should be analyzed. Yet another approach is to have both systems operational all the time and use a beamsplitter to give each a fraction of the light. If a 50/50 beamsplitter is used then each gets half the light and the error increases by a factor of $\sim\sqrt{2}$ for each. We now describe another approach which allows a more optimal use of the light. In order to understand this system we need to digress and discuss some more aspects of the Fabry-Perot.

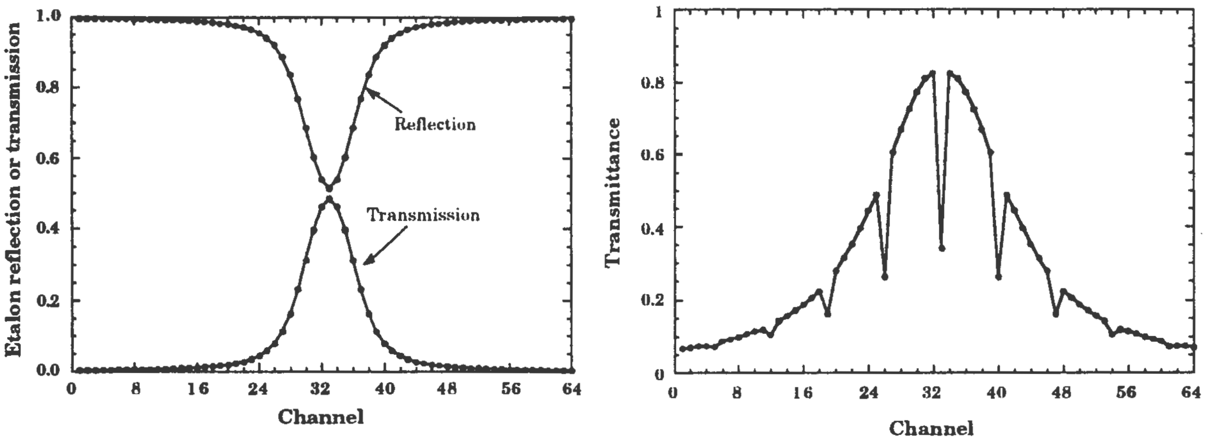

Fig. 26. (a) Transmission and reflection of an etalon. (b) Transmission of molecular etalon after reflection by aerosol etalon.

The Fabry-Perot is often touted as an efficient user of light, and in some respects it is (Jacquinot, 1954), but it actually throws away a significant amount of light. If one order is projected onto a detector a fraction [(1-R)/(1+R)] of the light incident on the etalon is actually transmitted while the rest is reflected. This reflected light amounts to a fraction 2R/(1+R). For example, if R=0.90 then 95% of the light is reflected. If less than a full free spectral range is projected, a higher fraction of the light is transmitted. This is the reason that some studies of incoherent lidar have projected less than a full free spectral range on the detector (Hays et al., 1984; Rees and McDermid, 1990). Figure 26(a) shows the reflection and transmission curves for the aerosol etalon which were described for System A (gap=30 cm, reflectivity=0.90). The maximum transmittance is about 50%, which is the result of the losses and defects assumed for this etalon. The reflectivity is simply 1-T, which is valid because the absorption losses in etalons with dielectric coatings are very small and any scattering losses are very narrow angle and do not diverge much from the specular beam. This points out that even with a system that projects 56% of an order on the detector, a very large fraction of the light is reflected. If we could use the reflected light as an input for a molecular etalon then the instrument function would look like that shown in Fig. 26(b). The spectral width of the molecular etalon is about 16 times greater than the aerosol etalon. The bite-outs in the transmission function are due to the light transmitted by the aerosol system. Clearly, though, the spectral shape still retains its fundamental characteristics, so Doppler shifts can be determined. If we can arrange the optical system so that the reflected light from the aerosol etalon can be used as the input to the molecular system, then we have a system that is very light efficient and can simultaneously use the spectral signature of the aerosol and molecular scattering.

We are left to show that an optical system can be arranged to do this. Figure 27(a) shows the typical optical layout for either an aerosol or molecular system. The similarities with the HRDI system are immediately apparent with the fundamental difference being the optics necessary to perform the circle-to-line conversion and the CCD instead of an IPD detector. Figure 27(b) shows how a system could be arranged to accommodate the combined system. The input optics are similar to before, with an interference filter and two etalons providing the filtering necessary to reduce the solar background. An imaging lens after the second etalon forms an image that is located slightly offset from the optical axis. The light reflected from the aerosol etalon will form an image on the opposite side of the optical axis where it can be directed into the molecular system. Since the light is no longer symmetric around the optical axis we must either increase the size of the etalon or increase the dynamic range. Either is possible, but here we have allowed the etalon size to increase if possible. This system has been optimized as the other systems. We have limited the aerosol etalon to a maximum of 30 cm in both cases. The system at 355 nm (System G) can handle a dynamic range of 50 m/s with an etalon diameter of 10 cm. The system at 532 nm (System H) requires that the dynamic range of the aerosol system be increased to 660 m/s.

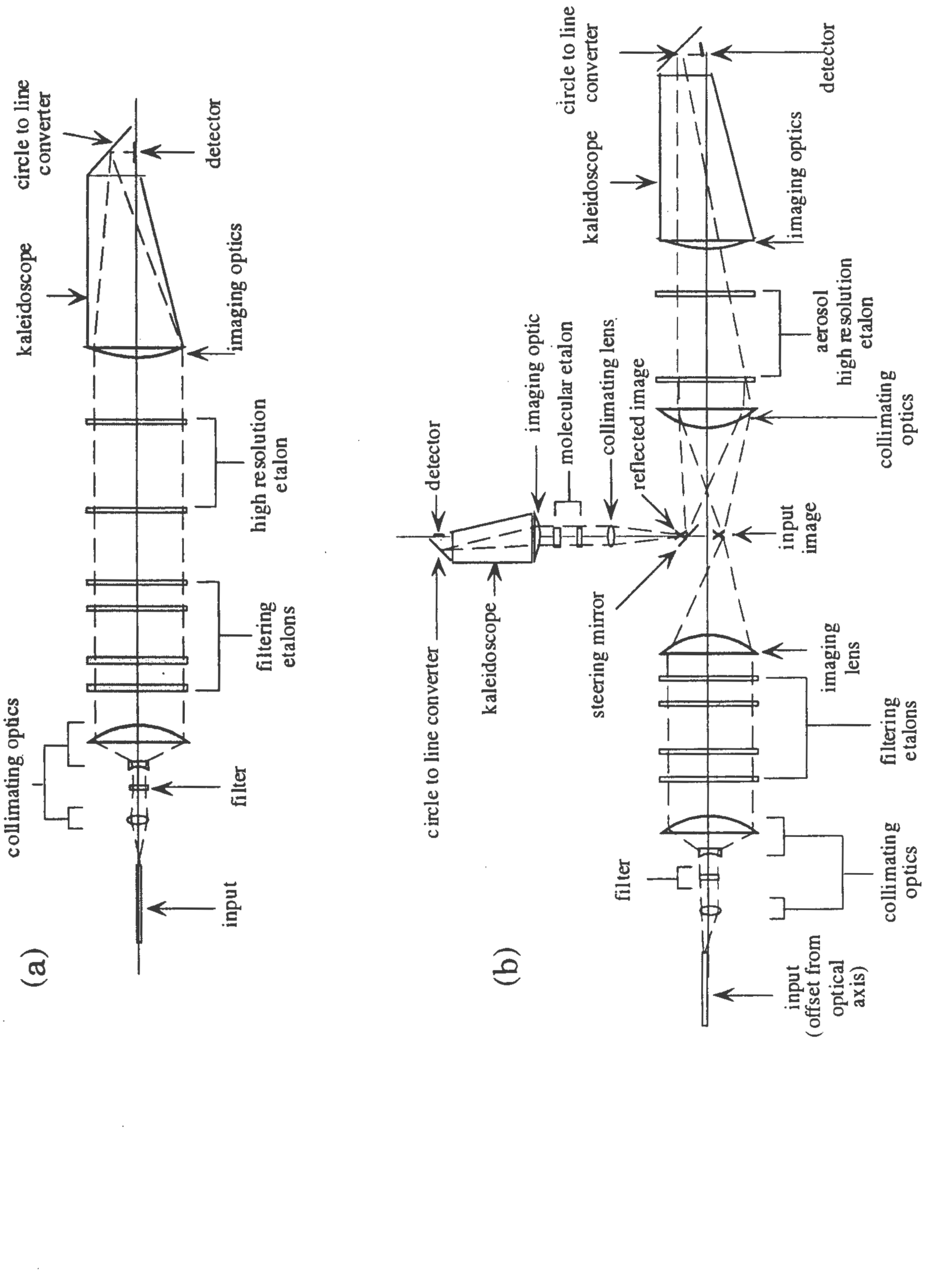

Fig. 27. (a) Aerosol or molecular lidar optical layout. (b) Combined aerosol and molecular lidar optical layout.

Table 8. Incoherent lidar system summary.

					System					
	A	B	C	D	E	F	G		H	
Laser wavelength (nm)	355	532	355	532	355	532	355	355	532	532
Scatterer	A	A	A	A	M	M	M	A	M	A
Etalon thickness (cm)	30.00	26.50	53.25	75.90	1.60	2.20	1.60	30.00	2.20	26.30
Etalon reflectivity	0.9125	0.9125	0.9000	0.8625	0.7125	0.7375	0.7125	0.9125	0.7375	0.8875
Fraction of order on detector	0.56	2.42	1.00	6.28	0.48	0.44	0.48	0.56	0.44	4.35
Etalon diameter (cm)	9.8	10.0	9.8	10.0	2.4	6.4	1.8	10.0	6.4	10.0
Velocity range (m/s)	50	330	50	330	800	800	800	50	800	660
Telescope FOV (full)(mr)	0.16	0.42	0.16	0.42	0.16	0.42	0.12	0.12	0.42	0.42
Medium resolution etalon thickness (cm)	0.336	0.973	0.382	1.998	0.129	0.627	0.152	0.152	0.973	0.973
Low resolution etalon thickness (cm)	0.073	0.844	0.083	1.732	0.028	0.136	0.033	0.033	0.211	0.211
Medium resolution etalon reflectivity	0.80	0.80	0.80	0.80	0.80	0.80	0.80	0.80	0.80	0.80
Low resolution etalon reflectivity	0.80	0.80	0.80	0.80	0.80	0.80	0.80	0.80	0.80	0.80
Filter width (FWHH) (nm)	0.8	0.1	0.8	0.1	0.8	0.1	0.8	0.8	0.1	0.1

A=Aerosols, M=molecular

A summary of the optimized systems is given in Table 8. In the next section we will discuss more fully the performance of each of these systems.

4.2. *Lidar Performance*

The performances of the eight lidar systems defined above are demonstrated in this section. The performance of each is examined with the aerosol model described earlier. The parameters of the model are chosen to provide a variety of aerosol conditions, particularly extreme ones. The different models are shown in Table 9 along with the plotting symbol used for each in subsequent plots. We also examine the effect of sunlight on the performance of each system. Some parameters are then varied to show their effect on the performance.

An important consideration is the total number of photons collected by the system and whether they are molecular or aerosol scattered. Figure 28 shows the calculated number of aerosol and molecular photons collected by the telescope at 355 nm. The molecular signal is most regular, but it can still vary by approximately a factor of 5. This is due to the varying amounts of extinction by aerosols. The aerosol return is much more variable, particularly in the free troposphere. In most cases the total number of aerosol photons collected is less than from molecules, but in the boundary layer and stratosphere the aerosol contribution can be roughly equal to the molecular.

Table 9. Model aerosol distributions.

Boundary layer height	1.0 km
Stratosphere height	20 km
Stratosphere scale height	3 km
Extinction/backscatter ratio	25 sr

Model	Mixing Ratio			
	Boundary layer	Background	Stratosphere	Symbol
1	1.0×10^{-9}	1.0×10^{-11}	5.0×10^{-10}	plain, solid, thin line
2	1.0×10^{-9}	1.0×10^{-11}	5.0×10^{-9}	plain, solid, thick line
3	1.0×10^{-9}	1.0×10^{-9}	5.0×10^{-10}	plain, dashed, thin line
4	1.0×10^{-9}	1.0×10^{-9}	5.0×10^{-9}	plain, dashed, thick line
5	1.0×10^{-7}	1.0×10^{-11}	5.0×10^{-10}	filled circles, solid, thin line
6	1.0×10^{-7}	1.0×10^{-11}	5.0×10^{-9}	filled circles, solid, thick line
7	1.0×10^{-7}	1.0×10^{-9}	5.0×10^{-10}	filled circles, dashed, thin line
8	1.0×10^{-7}	1.0×10^{-9}	5.0×10^{-9}	filled circles, dashed, thick line

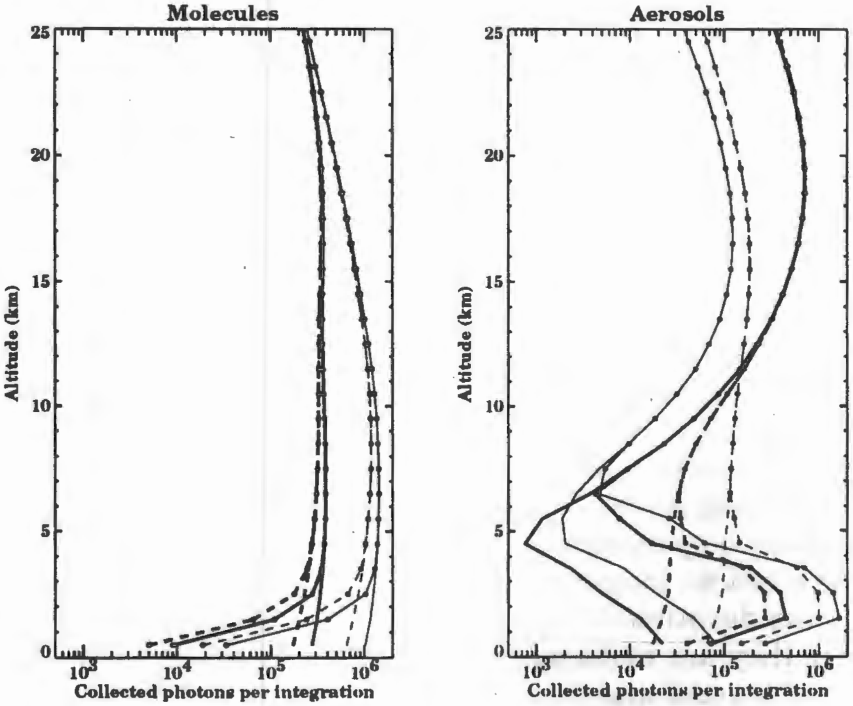

Fig. 28. Calculated number of aerosol and molecular photons collected by the telescope at 355 nm. See Table 9 for definition of plotting symbols.

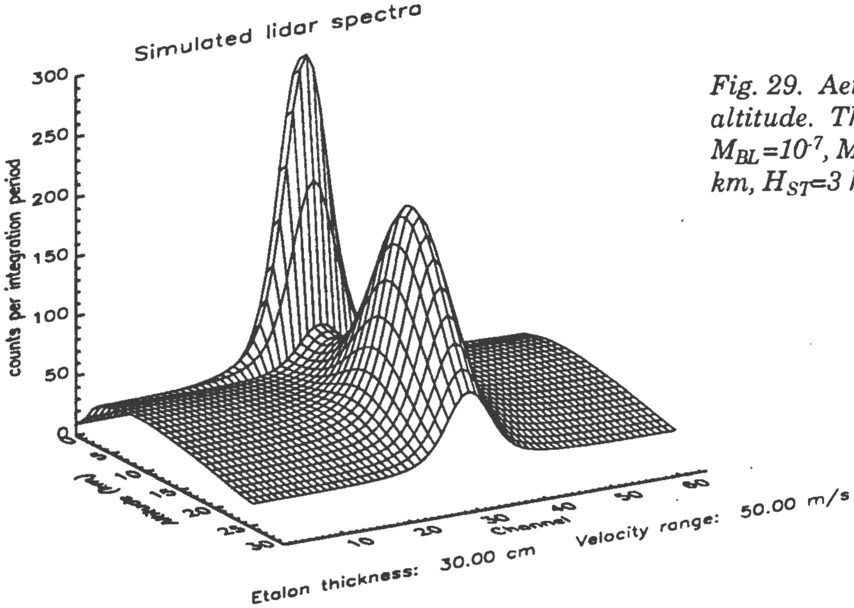

Fig. 29. Aerosol spectra as a function of altitude. The aerosol parameters are $M_{BL}=10^{-7}$, $M_{BG}=10^{-9}$, $M_{ST}=2x10^{-9}$, $Z_{BL}=1$ *km,* $H_{ST}=3$ *km.*

Simulated spectra as a function of altitude from systems A and E for a moderate aerosol loading case are shown in Figs. 29 and 30. In these simulations we let $M_{BL}=10^{-7}$, $M_{BG}=10^{-7}$, $M_{ST}=2 \times 10^{-9}$, $Z_{BL}=1$ km and $H_{ST}=3$ km. In Fig. 29 (system A) the aerosol signature is narrow and strong in the stratosphere and in the boundary layer, but is relatively weak in the free troposphere. Figure 30 (system E) shows a relatively broad signal which is again strong in the stratosphere and boundary layer. This is because systems designed to use the molecular return will be aided by any aerosol return since it is so narrow. The converse is not true. Molecular scattering will appear as a continuum background in an aerosol system and decrease the signal-to-noise ratio.

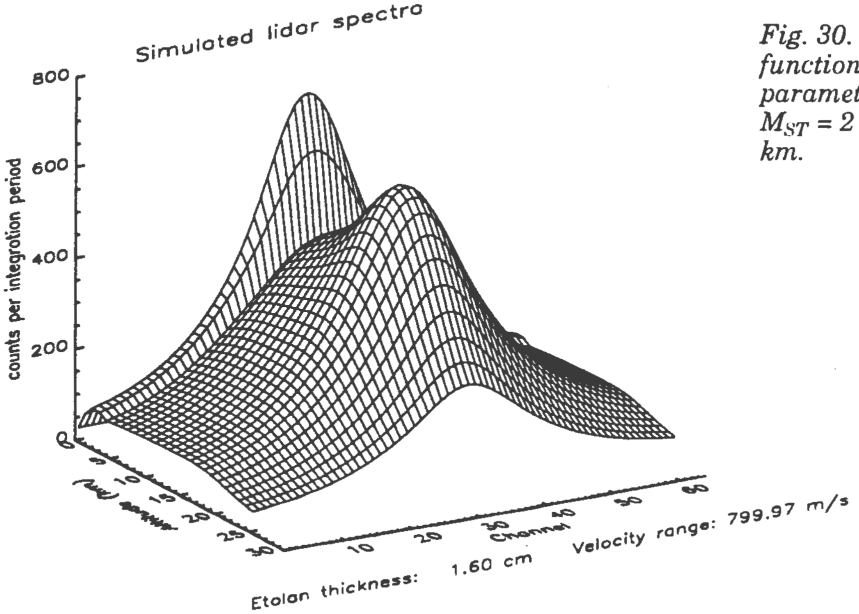

Fig. 30. Rayleigh spectra as a function of altitude. The aerosol parameters are $M_{BL} = 10^{-7}$, $M_{BG} = 10^{-9}$, $M_{ST} = 2 \times 10^{-9}$, $Z_{BL} = 1$ *km,* $H_{ST} = 3$ *km.*

Figures 31-38 show the horizontal line of sight wind errors for each of the eight defined systems. In all cases the error is shown for daylight and darkness. For the aerosol systems (A, B, C, and D) the errors can be below 1 m/s if there are sufficient aerosols; but low aerosol situations can lead to an error in excess of 10 m/s. The molecular systems (E-F) do not show the same degree of variability but can vary in the free troposphere from 1-2 m/s up to 6-7 m/s. The combined systems (G and H) provide the best error, with no more than 3 m/s at about 4-5 km. There is also a pronounced difference between the systems operating at 532 nm and at 355 nm. The eye safety constraint that forces the large number of small pulses at 532 nm causes this system to suffer significantly when there is sunlight. This result could be improved with better filtering, which is possible; there are filters available with half-widths less than 0.1 nm, but there may be a significant penalty in transmission. A system operating at 532 nm could operate very well in darkness, and hence could be used as a viable demonstration project. But there are better wavelengths to use in an operational system. Systems operating at 355 nm, or any wavelength below 400 nm where eye safety is not a major concern, can be designed so that the solar background is not significant.

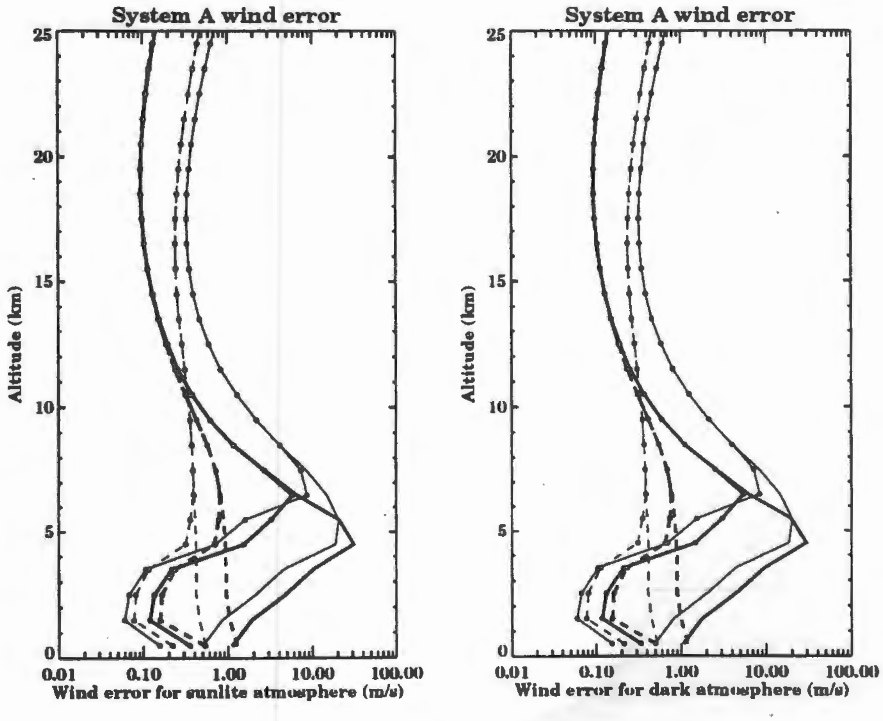

Fig. 31. Wind errors for system A. See Table 9 for definition of plotting symbols.

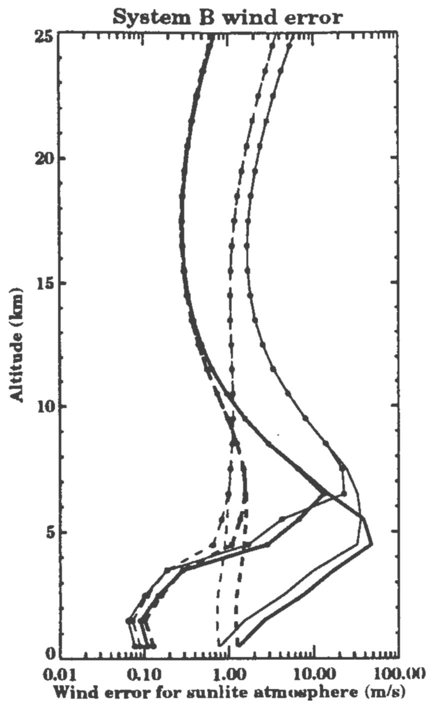

Fig. 32. Wind errors for system B. See Table 9 for definition of plotting symbols.

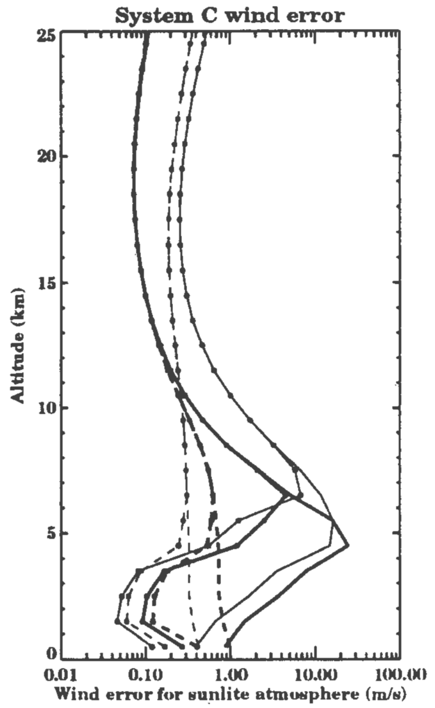

Fig. 33. Wind errors for system C. See Table 9 for definition of plotting symbols.

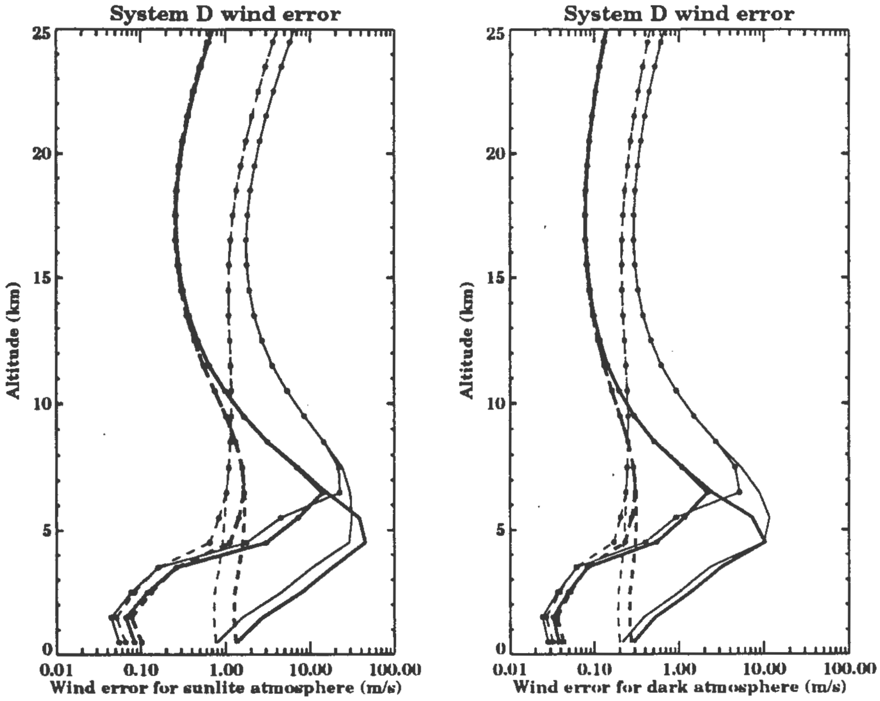

Fig. 34. Wind errors for system D. See Table 9 for definition of plotting symbols.

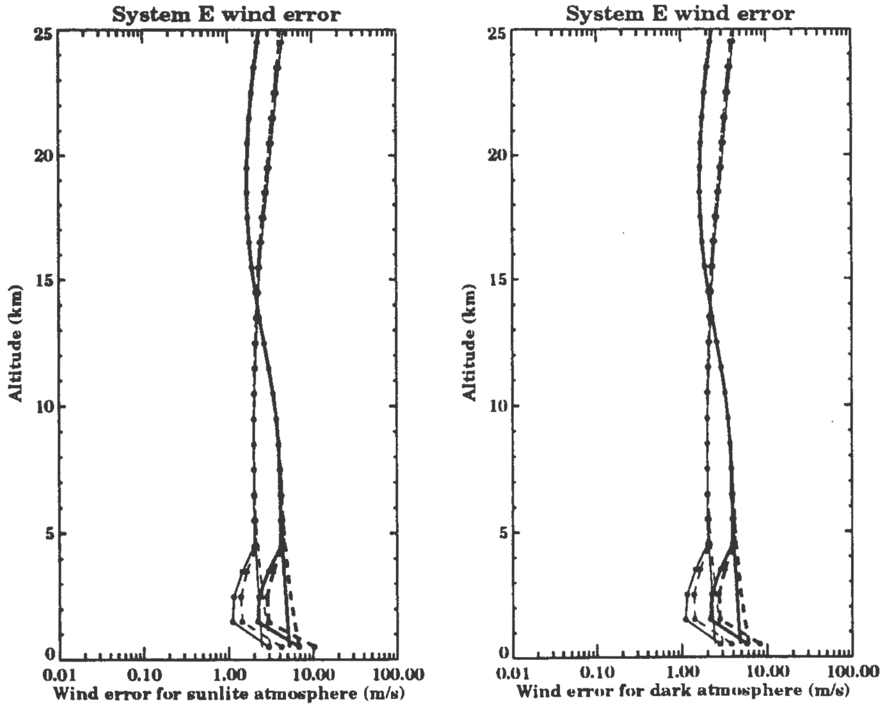

Fig. 35. Wind errors for system E. See Table 9 for definition of plotting symbols.

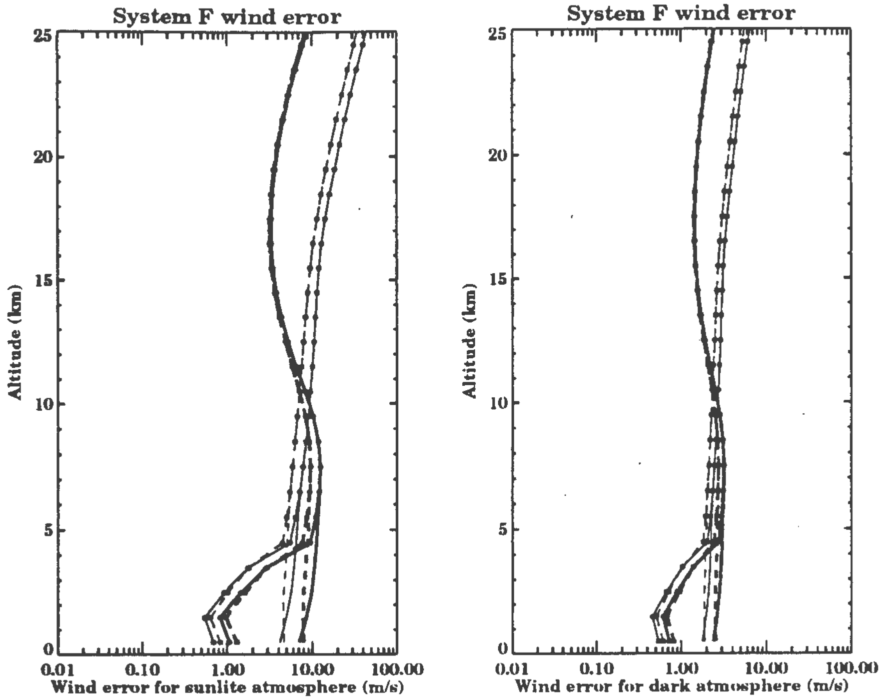

Fig. 36. Wind errors for system F. See Table 9 for definition of plotting symbols.

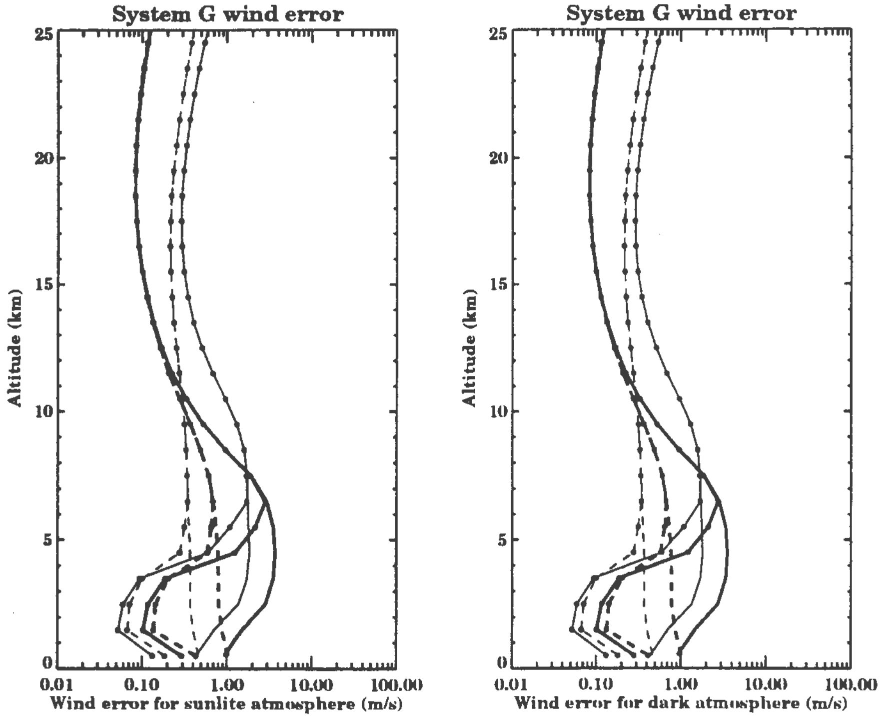

Fig. 37. Wind errors for system G. See Table 9 for definition of plotting symbols.

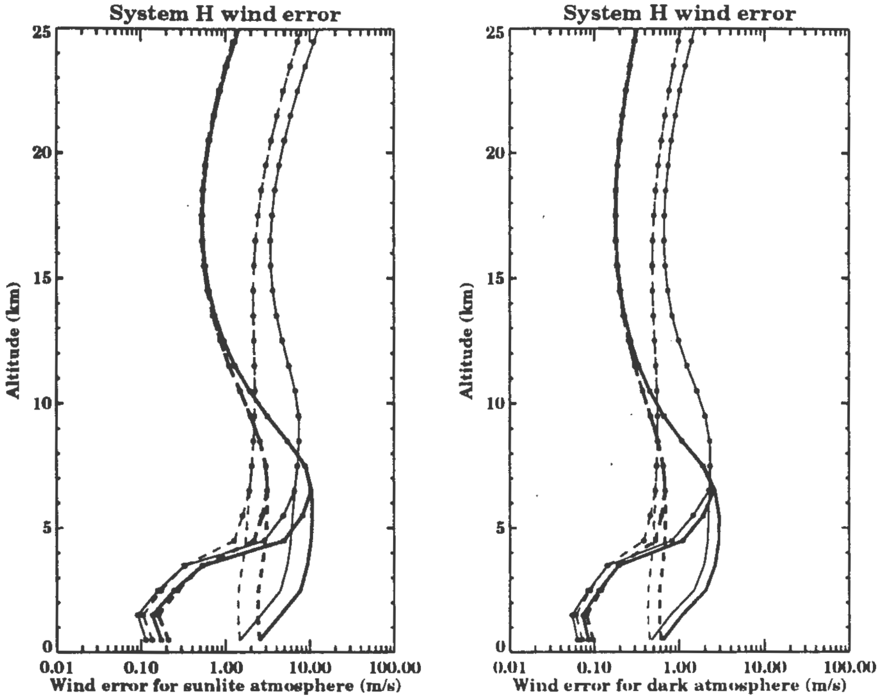

Fig. 38. Wind errors for system H. See Table 9 for definition of plotting symbols.

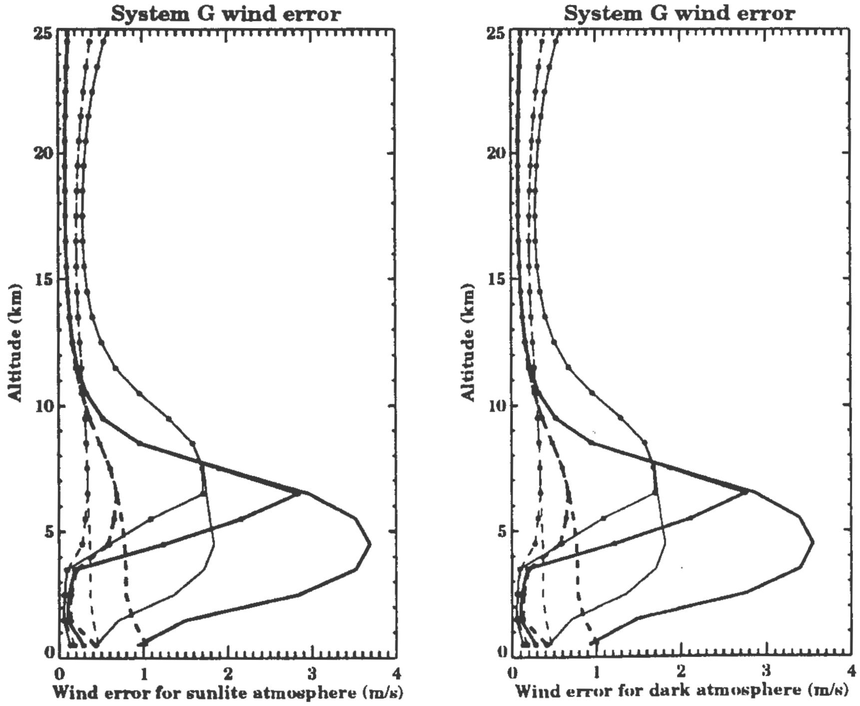

Fig. 39. Wind error for system G. This is the same as Fig. 37 except the wind error is plotted on a linear scale. See Table 9 for definition of plotting symbols.

System G (combined aerosol and molecular at 355 nm) provides the best overall result. Figure 39 shows the wind errors in more detail as a function of altitude for this system. The boundary layer winds in the worse case are 1 m/s and in most cases less than 0.5 m/s. The free troposphere winds are typically 0.5-1 m/s but errors can get as large as 3.5 m/s. In the stratosphere the wind errors decrease again to less than 1 m/s. We will use this system in a series of sensitivity studies and as the system to compare with a coherent system.

4.2.1. OBSERVATION ANGLE

We examined the effect of varying the observation angle from 20° to 60° from the nadir. Smaller angles have less attenuation and therefore more light can penetrate to lower in the atmosphere. Simultaneously, the component of the horizontal wind will decrease and reduce the sensitivity to wind shifts. Figure 36 shows the horizontal wind errors as a function of observation angle for 4 different altitudes and aerosol loadings. These situations were chosen to represent some extreme cases. All four cases show a shallow minimum somewhere between 30° and 50° with the error rising rapidly after 50° and a much less rapid increase going towards

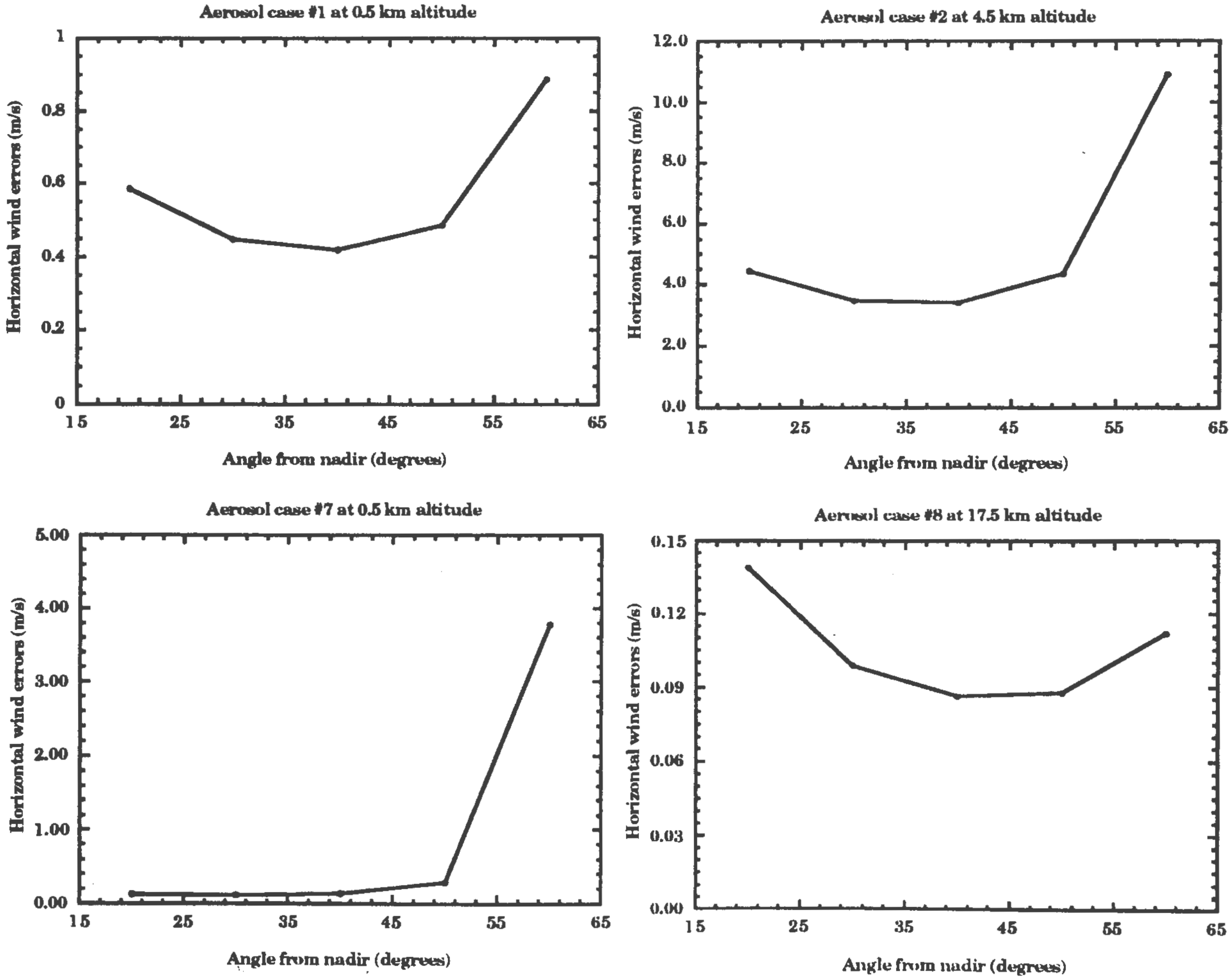

Fig. 40. Wind errors as a function of viewing angle for selected aerosol loading and altitudes.

20°. From this it is clear that an incoherent system operating at 355 nm should observe the atmosphere at an angle of about 40° from the nadir.

4.2.2. DARK COUNTS

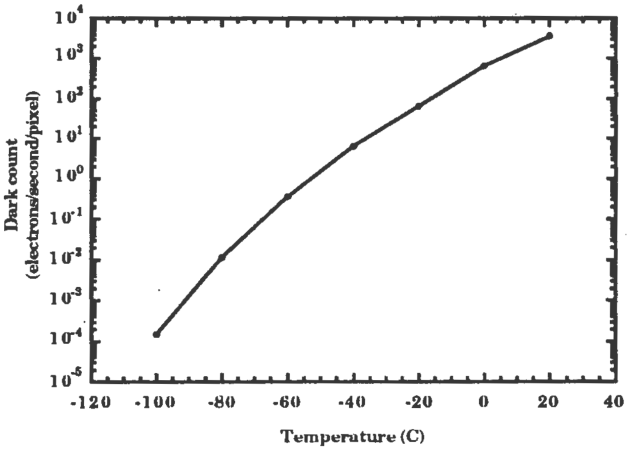

Fig. 41. Dark count of Tektronix TK1024 as a function of temperature. Dark counts are electrons per second per pixel.

We use a Tectronics TK1024 CCD as a model for the detector. The dark counts are a strong function of temperature (Fig. 41). This CCD is a 1024 by 1024 array so there are approximately 10^6 pixels. To a first order approximation we assume each channel is composed of the same number of pixels and all pixels are used. This is by far an upper estimate of the dark count. Further analysis of the mapping of the light on the detector could reduce this number by a factor of 10. The number of dark counts/channel is then

$$N_{Dark}(T) = \frac{n_{shots} n_{pixels}}{2\,prf\; n_c n_{alt}} \frac{\partial N_{Dark}(T)}{\partial t}, \qquad (96)$$

where n_{shots} is the number of shots collected, n_{pixels} is the total number of pixels, prf is the pulse repetition rate, n_c is the total number of spectral channels, n_{alt} is the number of altitudes to be examined and $[\partial N_{Dark}(T)]/\partial t$ is the dark count rate (electrons/second/pixel). The factor of 2 appears because only half of the detector is available for data since the other half is used to store that data as the image is shifted.

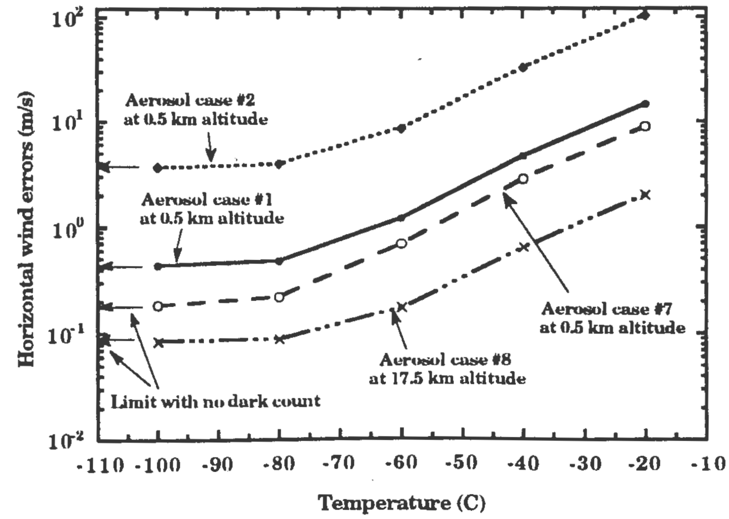

Fig. 42. Horizontal wind errors as a function of detector temperature assuming a TEK1024 CCD and all pixels are used.

The effect of dark counts is shown in Fig. 42. Below -80° C there is virtually no increase in wind error compared to the condition with no dark counts at all. The effects rise moderately by -60° C and much more dramatically above that. This result should not be taken too literally since the actual number of pixels per channel depends on the detailed engineering of the detector system and somewhat on the exact CCD used. It does show that it is possible to reduce the effect of dark counts to insignificance by reducing the detector temperature.

4.2.3. READ NOISE

The CCD read noise occurs whenever the signal on the chip is read off. Since our implementation of the CCD would integrate a significant amount of signal on the chip, reads are relatively infrequent and the read noise should not be a major source of noise. We examined the wind error for read noise levels of 0, 2.5, 5, and 10 electrons per read for a detector with 64 spectral channels. We note the current state of the art for CCDs is less than 5 electrons per read and is approaching 1 electron per read. Table 10 shows the wind errors for selected altitudes and aerosol loadings. These are the same as used in the discussion of observation angle. The results clearly show that read noise adds very little to the overall error.

Table 10. Wind errors with read noise.

	Horizontal wind error (m/s)			
Read noise (electrons/read)	**Aerosol #1 0.5 km alt**	**Aerosol #2 4.5 km alt**	**Aerosol #7 0.5 km alt**	**Aerosol #8 17.5 km alt.**
0.0	0.421	3.60	0.170	0.0837
2.5	0.429	3.64	0.178	0.0845
5.0	0.437	3.69	0.186	0.0853
10.0	0.453	3.78	0.198	0.0868

4.2.4. LASER BANDWIDTH

The laser bandwidth has been varied to get a better estimate of what the laser bandwidth requirement should be. The laser 1/e width was varied from 0 to 3 x 10^{-3} cm^{-1} (30 MHz). Figure 43 shows the wind error for selected conditions. In all cases a laser line width of less than 10^{-4} cm^{-1} has no effect on the wind error. This implies that the laser has no broadening effect on the signal. In 3 out of the 4 cases shown the error increases dramatically as the width increases. In these cases the wind error is largely determined by the aerosol signal. In the fourth case the error does not change significantly and is due to the fact that the molecular signal dominates the error. This analysis shows that the laser width is not important as long as it is less than 10^{-4} cm^{-1} (9 Mhz).

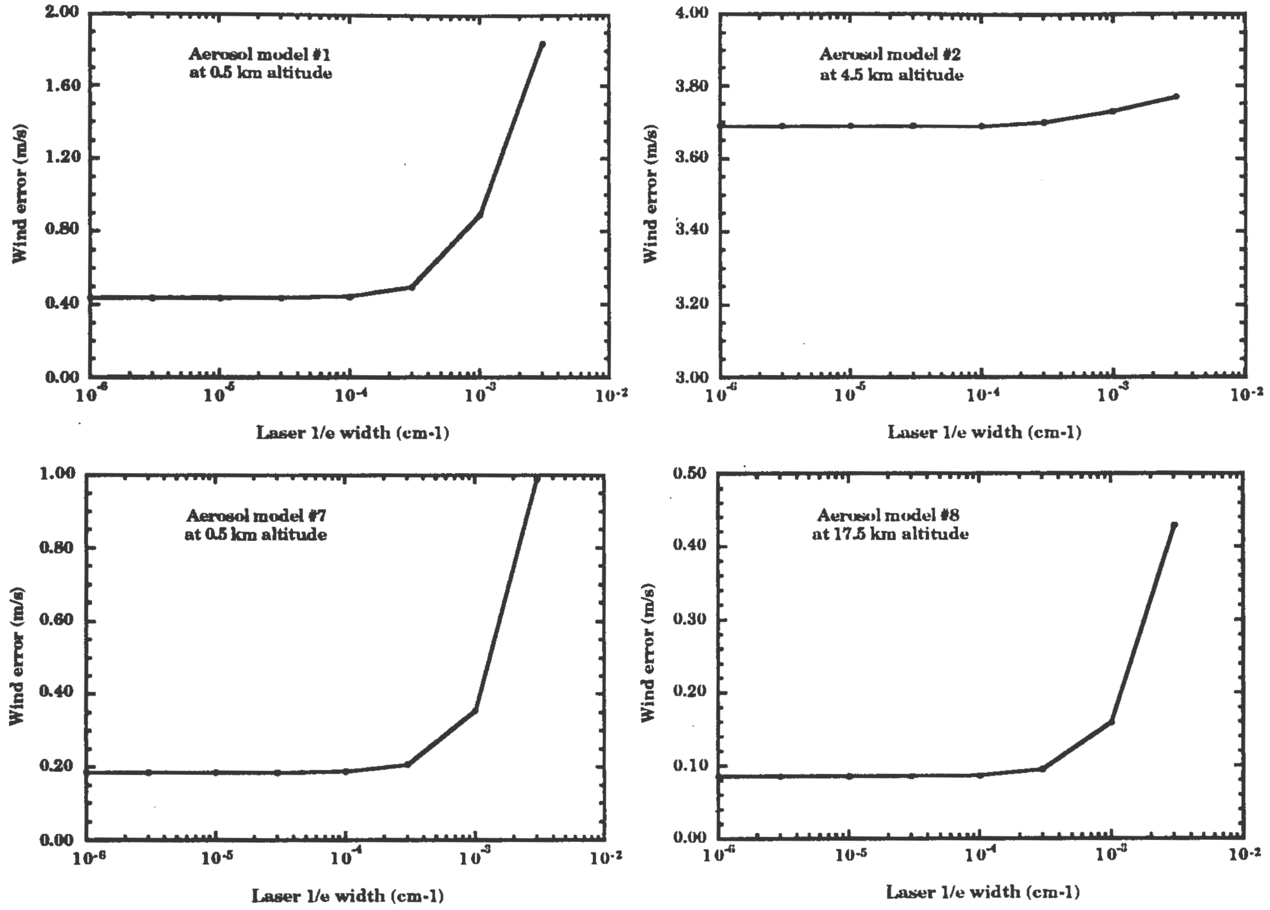

Fig. 43. Wind errors as a function of laser bandwidth for various altitudes and aerosol loading.

4.2.5. CLOUDS

Clouds have two important effects on a lidar system. First, if the clouds are thick enough then they prevent penetration to altitudes below the cloud layer. Second, they provide a large return allowing a good estimate of the winds at the cloud height to be made. Clouds are difficult to model in detail, and we have made the simplifying assumption that they are a Lambertain surface that can be characterized by an albedo. Table 11 shows the wind errors for clouds at various levels assuming the clouds have an albedo of 0.5.

Table 11. Cloud top wind errors (m/s).

Cloud Altitude (km)	Aerosol Model							
	1	2	3	4	5	6	7	8
0.0	1.73×10^{-2}	3.34×10^{-2}	2.19×10^{-2}	4.26×10^{-2}	4.36×10^{-1}	1.22×10^{0}	6.80×10^{-1}	2.08×10^{0}
2.5	1.32×10^{-2}	2.55×10^{-2}	1.59×10^{-2}	3.10×10^{-2}	1.45×10^{-2}	2.81×10^{-2}	1.81×10^{-2}	3.53×10^{-2}
5.0	1.09×10^{-2}	2.10×10^{-2}	1.25×10^{-2}	2.42×10^{-2}	1.09×10^{-2}	2.11×10^{-2}	1.25×10^{-2}	2.43×10^{-2}
7.5	9.43×10^{-3}	1.81×10^{-2}	1.04×10^{-2}	2.01×10^{-2}	9.43×10^{-3}	1.81×10^{-2}	1.04×10^{-2}	2.01×10^{-2}
10.0	8.42×10^{-3}	1.59×10^{-2}	9.01×10^{-3}	1.70×10^{-2}	8.42×10^{-3}	1.59×10^{-2}	9.01×10^{-3}	1.70×10^{-2}

Except for two cases (models 7 and 8 for surface level clouds), the wind errors are extremely small. For a lidar system with this much power, the actual wind errors will most likely be dominated by other noise terms, such as spacecraft pointing accuracy. Another way to view this data is that reasonable cloud top wind would require a laser with much less power than used in this baseline. The winds for a cloud at the surface are equivalent to a ground return and show the uncertainties that are possible by using the ground as a zero velocity reference source.

4.2.6. WAVELENGTH DEPENDENCE OF BACKSCATTER

We have assumed the backscatter has a quadratic wavelength dependence which allows us to use measurements of the backscatter at 9-10 microns and estimate the backscatter in the visible or near UV region. Other studies indicate that a power of two may be too large. Lawrence (1985) suggests a power of 1.5 for altitudes below 15 km and 2 for altitudes above. Recent work by McKenzie et al. (1994) use data from lidars operating at wavelengths ranging from 351 to 940 nm and find exponents ranging from 0.87 to 1.57 depending on altitude. We examine the effect of wavelength dependence by comparing simulations with a quadradic and linear dependence. These two cases should bracket the real atmosphere. Figure 44 shows the wind error for the two cases. There are some significant differences, most notably the decrease of the wind error in the free troposphere and an increase in the wind error in the stratosphere when the power is 1 instead of 2. The linear wavelength coefficient means that the effect of aerosols (in both attenuation and scattering) is less. In the stratosphere the reduction in scattering is more important and the error increases. In the troposphere either effect can be dominant, and the result is not so straightforward. The errors can be better or worse depending on the aerosol loading. The fundamental point is that in either case useful wind measurements can be made.

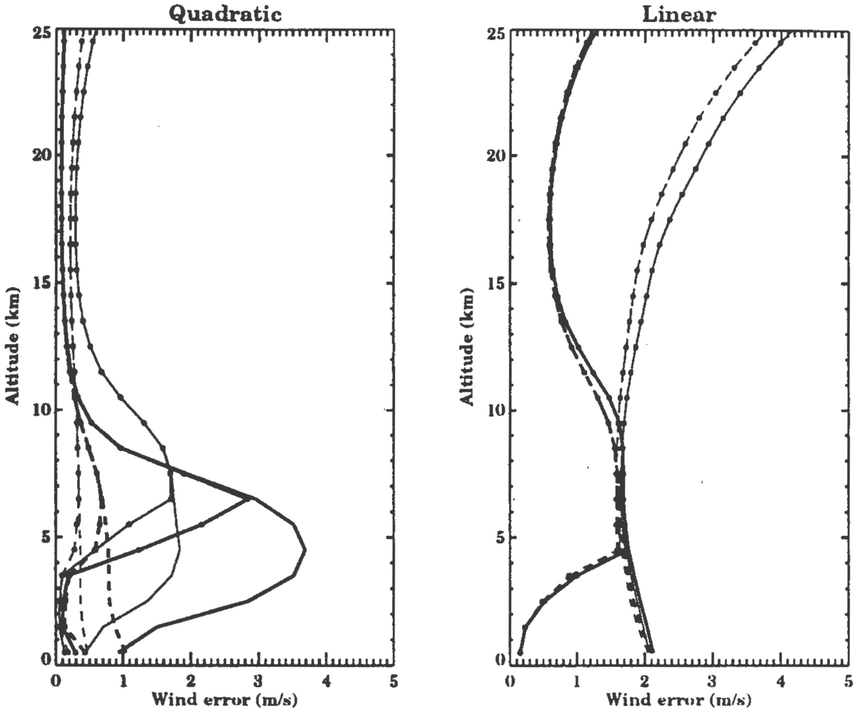

Fig. 44. Wind errors for different wavelength dependence of the aerosol backscatter. The form used is $\beta(\lambda) = \beta(\lambda_0)(\lambda_0/\lambda)^n$, *where n=2 (quadratic) or n=1 (linear). See Table 9 for definition of plotting symbols.*

4.2.7. OTHER PARAMETERS

This report has focussed on the measurement of Doppler shifts, but it is worthwhile to point out that other interesting and useful geophysical features can be determined from this type of data (Fiocco et al., 1971; Abreu, 1980; Curran et al., 1987b). We note that this type of system has capabilities that are similar to the LITE experiment (McCormick et al., 1993), and most, if not all, of the parameters measured by that system can also be determined by an incoherent wind sensor. Atmospheric temperatures, density, cloud top heights, aerosol backscatter, and optical depth are a few of the quantities that can be measured. Future work could examine in detail the ability of an incoherent system to measure these quantities.

5. Comparison of Incoherent and Coherent Lidar Systems

5.1. Simulations

The two systems have been compared by determining how much laser power is required to achieve a certain horizontal line-of-sight velocity measurement accuracy. We perform a comparison of the measurement accuracy and not of the fundamentally more important observational accuracy (see section 3.1.3.5 for a discussion of measurement and observation errors). However, using measurement errors most directly compares the detection techniques since sampling issues are not involved. The results reveal the required output power of the laser. Characterizations of the various laser efficiencies are beyond the scope of this report, although they are certainly extremely important. We use two sets of requirements for the horizontal line-of-sight wind accuracy in the comparisons: 1) 1 m/s throughout the range of interest (from the surface to 25 km altitude), and 2) 1 m/s below 3 km and 3 m/s above. The first represents the most challenging requirements of the meteorological community, and the second is roughly comparable to the accuracy currently achieved by radiosondes. Various system efficiencies are outlined in Table 12 for the coherent system and in Tables 7 and 8 for the incoherent. The IDL program used to perform the coherent calculations is given in Appendix V.

Table 12. Coherent lidar simulation parameters.

Parameter	Small Satellite
Altitude	350 km
Nadir angle	45 deg
prf	1 Hz
Pulse energy	20 Joule
Transmitter efficiency	0.05
Wavelength	9.1 microns
Pulse duration	4.7 μ sec
Laser pulse duration	1.0 μ sec
Optics diameter	1.0 m
Telescope area	0.785 m^2
Focal length	2.5 m
Receiver efficiency	0.09
Optics	0.4
Detector	0.5
Quantum efficiency	0.45
False alarms	0.01
L (turbulence length)	5.0 km.
Turbulence C_n^2	10^{-15} ($m^{-2/3}$)*
r_a coherence radius	0.024
U_{max}	50 m/s
U_{atmos}	3.0 m/s
U_{bw}	0.724 m/s

* Smith, 1993.

Note that we compare systems with the same size receiving telescope (1 meter diameter). We perform the simulations for various aerosol loadings which bracket the extreme cases. These are summarized in Table 13.

Table 13. Aerosol model parameters.

Model	M_{BL}	M_{BG}	M_{ST}	Plotting symbol
1	1×10^{-9}	1×10^{-11}	5×10^{-10}	plus sign (+)
2	1×10^{-7}	1×10^{-11}	5×10^{-10}	Asterisk (*)
3	1×10^{-9}	1×10^{-9}	5×10^{-10}	Period (.)
4	1×10^{-7}	1×10^{-9}	5×10^{-10}	Diamond
5	1×10^{-9}	1×10^{-11}	1×10^{-9}	Triangle
6	1×10^{-7}	1×10^{-11}	1×10^{-9}	Square
7	1×10^{-9}	1×10^{-9}	1×10^{-9}	X
8	1×10^{-7}	1×10^{-9}	1×10^{-9}	filled circle

The coherent system error has been analyzed using the method outlined in section 3.2. The output power of the laser is assumed to be 20 J/pulse. Figures 45, 46, and 47 show the required energy for various attenuation models for a 1 m/s error.

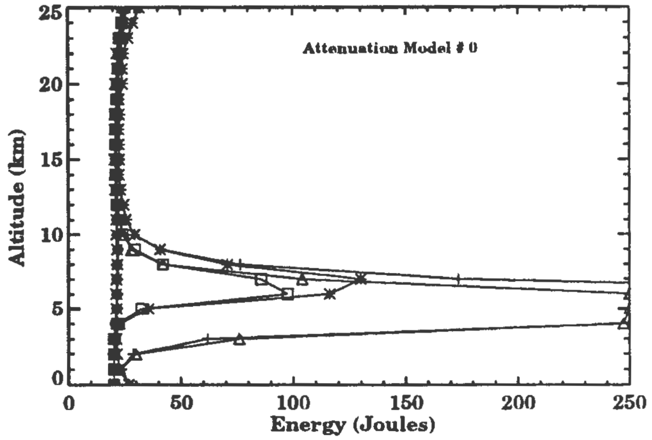

Fig. 45. Coherent lidar energy requirements, E=20 Joules, 1 m/s error, attenuation model #0.

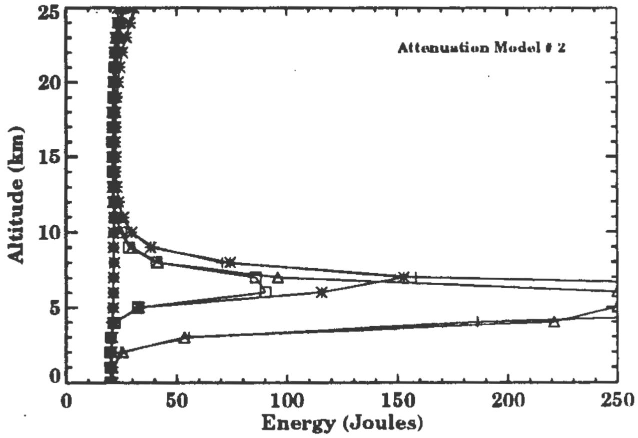

Fig. 46. Coherent lidar energy requirements, E=20 Joules, 1 m/s error, attenuation model #2.

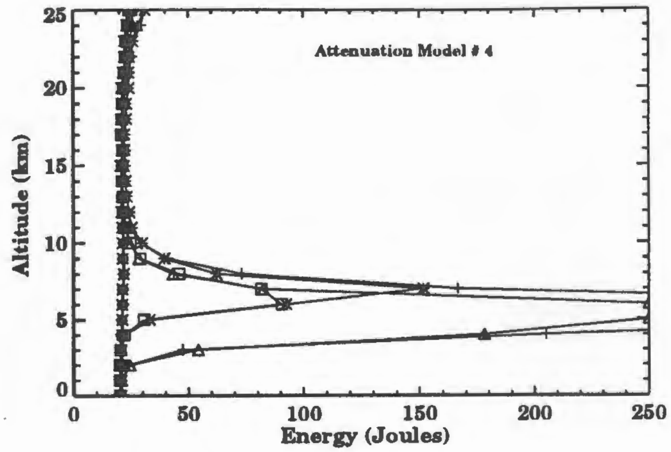

Fig. 47. Coherent lidar energy requirements, E=20 Joules, 1 m / s error, attenuation model #4.

The attenuation model is simply

$$T(z) = 10^{-0.1\,m\,\exp(-z/H_w)}, \qquad (97)$$

where m is the model parameter and H_w is the scale height of water, which in our calculations is equal to 1.5 km. Table 14 provides the relationship between model number and m. In the free troposphere and the lower stratosphere the effect of attenuation is very small. There is sufficient signal from a single pulse in these regions to make the measurement. The boundary layer shows a small attenuation effect, but overall attenuation is not a major concern for the coherent system. The energy requirement for the free troposphere can increase significantly above that required for either the boundary layer or stratosphere. When there are sufficient aerosols ($M_{BG} = 1 \times 10^{-9}$ in our models) the error remains in line with the boundary and stratospheric cases. For low aerosols ($M_{BG} = 1 \times 10^{-11}$ in our models) the error increased dramatically, up to several hundred joules (we stop the plotting at 250 J as a practical limit to the amount of energy expended on a single measurement). The situation improves as the error requirements are relaxed, as shown in Fig. 48 for attenuation mode 2. Now the maximum energy required is slightly more than 200 J. The reduced accuracy requirement has no effect on the boundary layer or stratosphere; one shot can still provide the required accuracy.

Table 14. Coherent Lidar Attenuation model parameters.

Model	m
0	10.0
1	6.0
2	3.5
3	1.0
4	0.5

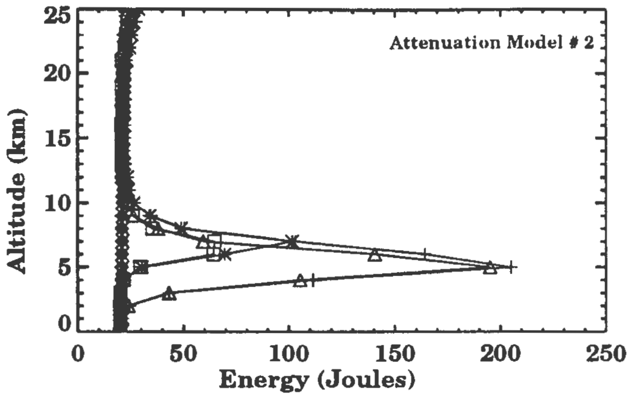

Fig. 48. Coherent lidar energy requirements, E=20 Joules, 1 m/s error, z<3 km; 3 m/s, z>3 km.

The energy requirements for the incoherent system were found by varying the number of laser shots until the wind error matched the desired value. For the system we have used in the simulations the error very closely goes as the inverse square root of the power (i.e. four times the power reduces the error by a factor of two). Figure 49 shows the energy requirements for a 1 m/s error everywhere. The largest energy requirements for the incoherent system occur in the free troposphere when the tropospheric aerosol loading is small and the stratospheric aerosol loading is large. Under the worst conditions, several hundred Joules would be required to achieve a 1 m/s wind error. With more aerosols the energy requirements drop to 20-50 J. The boundary layer can make a good measurement with much less than 10 J for large loadings in the boundary layer and low loading in the free troposphere and stratosphere. The stratosphere has fairly low energy requirements (<50 J) at all altitudes up to 25 km. With high aerosol loadings the energy requirement can be as low as 2 J. Figure 50 shows the energy necessary for errors of 1 m/s below 3 km and 3 m/s above. The absolute maximum energy is now reduced to slightly more than 200 J and most situations require less than 100 J to meet the requirement. This maximum value is almost the same as required by the coherent system. The stratosphere now requires less than 10 J everywhere and the free troposphere is typically less than 50 J.

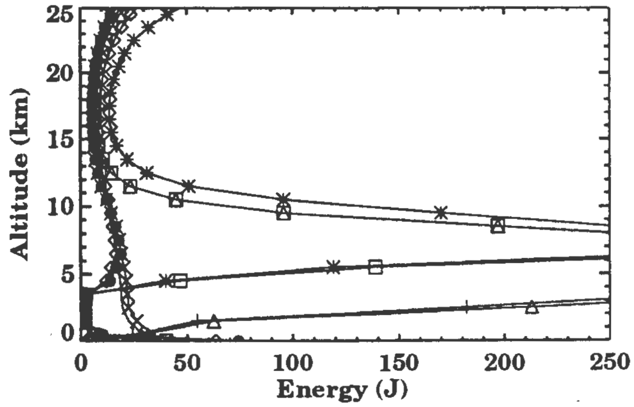

Fig. 49. Incoherent lidar energy requirements 1 m/s error.

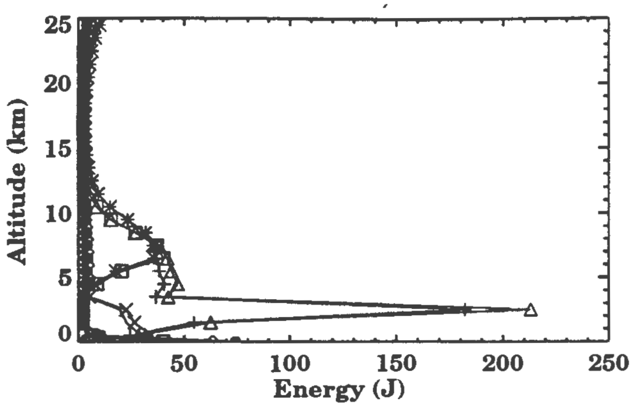

Fig. 50. Incoherent lidar energy requirements, 1 m/s error, z<3 km; 3 m/s, z>3 km.

The overall impression one gets from an examination of these plots is that the basic characteristics of each system are the same. Both can do extremely well in the boundary layer and stratosphere with a small amount of energy and both increase significantly under certain situations in the free troposphere. The necessary power for each system is comparable. This differs from previous studies (Menzies, 1986) which showed the coherent system to have significant advantages. The improvement of the incoherent system relative to the coherent is the result of two factors that were not considered in previous studies: 1) the CCD increases the detection efficiency by more than a factor of 10; and 2) the use of the molecular scattering in addition to aerosol in an efficient manner permits a more effective use of the scattered light. An important characteristic of the incoherent system is that it does not matter how the total amount of energy is obtained; 1 pulse at 10 Joules will give the same accuracy as 10 pulses at 1 Joule. All pulses will contribute to the total signal. Thus, several shots can be used and each can be aimed at a different location in a measurement volume. The averaging process then reduces observation error as well as measurement error. Both of these systems are clearly scalable. The incoherent system scaling is extremely straightforward. More photons will always decrease the uncertainty and except at very low photon flux rates (when detector noise and background may be significant) the uncertainty for a given system decreases as the inverse square root of the number of photons collected. The effect of changing any instrument parameter (telescope size, laser power, detector efficiency, etc.) can be readily determined once the error is determined for a standard instrument configuration. The scaling arguments are not so simple for the coherent system, primarily because of the effects of speckle. The methods described in this report can be used to perform the necessary calculations.

5.2. Summary and Conclusions

This report has described in detail some of the issues concerning an incoherent lidar system and compared the performance of an incoherent system with a coherent one. The incoherent system is much more competitive than previously believed (Menzies, 1985, 1986) primarily because of two factors. First, the CCD provides a factor of 10 increase in detector sensitivity, which lowers the time required to obtain a given measurement by the same amount. Second, the detection system has been optimized to use both the molecular and aerosol returns in such a way that the collected signal is used most efficiently.

This was not meant to be an engineering report, and some important questions in this area need further study. We have outlined several of the requirements for a laser but have not considered the state of the art of lasers operating in our desired wavelength region. This issue was examined in 1989 (Abreu et al.) as part of a study for a small lidar wind measuring system, and should be updated.

The CCD, which is assumed to be the detector in this study, has not been demonstrated to operate in the manner required. The circle-to-line system has been demonstrated to operate as theory indicates, but the shifting of the pixels as required in this application has not. This is the only technical component in the detector system that has no space heritage or has not been demonstrated in the laboratory. Although no technical reason exists indicating that this should be a problem, it should be verified with actual hardware.

Questions remain concerning the backscatter at various wavelengths. We have demonstrated that between extreme limits of the wavelength dependence of the backscatter coefficient, an incoherent system will perform very well. However, more measurements at difference wavelengths at difference locations, presented in a manner that aids comparison, would be useful.

Appendix I. Chapman Aerosol Model

```
; This routine calculates the aerosol distributions for
; the hays/skinner model with inputed values of the
; mixing ratios.
SET_PLOT,'TEK'
!P.MULTI=[0,0,0,0]
MZ=31
Z=indgen(MZ)
I=0
START: I=I+1
PRINT,'Enter Mixing ratio, Boundary, Background, stratosphere'
read,MBL,MBG,MST
HS=8.0
TAU=1.0
ZBL=1.0
ZST=20.0
DZST=3.0
JBL=FIX(ZBL+0.5)
RHO=Z
RHO=EXP(-(Z/HS))
BETA=RHO
BETA=RHO*(MBG+MBL*10^(-0.75*(Z-ZBL)))$
    +MST*EXP(-((Z-ZST)/DZST))*EXP(-TAU*EXP(-((Z-ZST)/(2.*DZST))))
BETA(0:JBL)=MBL*RHO(0:JBL)
IF(I EQ 1)  THEN BEGIN
PLOT_OI,BETA,Z,XRANGE=[1.0E-11,1.0E-6],YRANGE=[0.0,30.0]
ENDIF
IF(I NE  1) THEN BEGIN
OPLOT,BETA,Z
ENDIF
GOTO, START
END
```

Appendix II. Double Fabry-Perot Characterization

This appendix considers the equations necessary to calculate the response of the multiple etalon systems G and H described in chapter 4. The transmittance function of the aerosol system (directly transmitted by the aerosol etalon) is the same as described in chapter 3 and need not be repeated. The molecular system (reflected by the aerosol etalon and transmitted by the molecular etalon) will be described here. The transmission of this part of the system is the product of the transmittance of the molecular etalon (index 1) and the reflectance of the aerosol etalon (index 2) :

$$T_m(\Delta\nu,\theta) = T_1(\Delta\nu,\theta)\rho_2(\Delta\nu,\theta), \tag{A1}$$

where T_1 is the transmission and ρ_2 is the reflection of the etalons and T_m is the combined transmission. This is not completely valid in some systems as there can be interactions between the two etalons (McNutt et al., 1963). These interactions should be small for the configuration considered here. It is accurate enough for our purposes to assume the etalon reflectivity is given by:

$$\rho_2(\Delta\nu,\theta) = 1 - T_2(\Delta\nu,\theta). \tag{A2}$$

As before we make a definition to allow a more compact description of the Airy function. Let

$$\begin{aligned} B_n &= \left(\frac{2R}{1+R}\right) && \text{for } n = 0 \\ &= -2\left(\frac{1-R}{1+R}\right)R^n e^{-4\pi^2 n^2 \nu^2 \Delta t_r^2} && \text{for } n > 1 \end{aligned} \tag{A3}$$

Note that we have assumed the losses from this etalon to be negligible. This allows the etalon reflectivity to be written in a form that has the same characteristic as the transmission:

$$\rho(\Delta\nu,\theta) = \sum_{n=0}^{\infty} B_n \cos 2\pi n\left(\frac{\Delta\nu}{\Delta\nu_{FSR}} - \frac{\nu_0}{\Delta\nu_{FSR}}\frac{\theta^2}{2}\right). \tag{A4}$$

As with a single etalon we must integrate over the angle. In this case there is a magnification of the angle the light passing through the molecular etalon relative to the aerosol etalon. This magnification factor is called γ and is given simply by

$$\gamma = \sqrt{\frac{U_A}{U_m}}. \tag{A5}$$

where U_A and U_m are the dynamic range in velocity units of the aerosol and molecular systems, respectively. For example, if U_A equals 50 m/s and U_m equals 800 m/s, then γ is 0.25. The equation for the transmission through the molecular etalon is

$$T_m(\Delta\nu,\theta_o,\Delta\theta)=\frac{\displaystyle\int_{\theta_o-\frac{\Delta\theta}{2}}^{\theta_o+\frac{\Delta\theta}{2}} T_1(\Delta\nu,\theta)\rho_2(\Delta\nu,\gamma\theta)\theta d\theta}{\displaystyle\int_{\theta_o-\frac{\Delta\theta}{2}}^{\theta_o+\frac{\Delta\theta}{2}}\theta d\theta}, \tag{A6}$$

which, when evaluated and the angles converted to channel numbers, gives

$$\begin{aligned}T_m(\Delta\nu,j)=\frac{1}{2}\sum_{k=0}^{1}\sum_{n=0}^{\infty}\sum_{m=0}^{\infty}A_{1,n}B_{2,m}\Bigg[\cos 2\pi\left(\frac{n}{\Delta\nu_{FSR1}}+(-1)^k\frac{m}{\Delta\nu_{FSR2}}\right)\\ \cdot\left(\Delta\nu-\frac{j}{N_{FSR}}\Delta\nu_{FSR1}\right)\operatorname{sinc}\frac{\pi}{N_{FSR}}\left(n+(-1)^k m\gamma^2\frac{\Delta\nu_{FSR1}}{\Delta\nu_{FSR2}}\right)\Bigg].\end{aligned} \tag{A7}$$

Note that N_{FSR} refers to the molecular system.

The number of counts, N_{laser}, sensed by any channel of a detector is given by the convolution of the Fabry-Perot instrument function as given by Eq. (A7) and the spectral return given by Eq. (2), multiplied by appropriate instrument constants. This operation gives:

$$\begin{aligned}N_{laser}(j)=\frac{P_T\lambda}{hc}O_A(r)\frac{A_T\Delta h}{4\pi r^2}T^2(r)\frac{QT_{op}T_f(\nu)}{n_c}\frac{1}{2}\sum_{k=0}^{1}\sum_{n=0}^{\infty}\sum_{m=0}^{\infty}A_{1,n}B_{2,m}\\ \cdot\left\{\cos 2\pi\left[\left(\frac{n}{\Delta\nu_{FSR1}}+(-1)^k\frac{m}{\Delta\nu_{FSR2}}\right)\left(\nu_1-\nu_0-\frac{\nu_1 U}{c}\sin\phi-\frac{j\Delta\nu_{FSR}}{N_{FSR}}\right)\right]\right.\\ \cdot\operatorname{sinc}\frac{\pi}{N_{FSR}}\left(n+(-1)^k m\gamma^2\frac{\Delta\nu_{FSR1}}{\Delta\nu_{FSR2}}\right)\\ \cdot\exp\left[-\pi^2\left(\frac{n}{\Delta\nu_{FSR1}}+(-1)^k\frac{m}{\Delta\nu_{FSR2}}\right)^2\left(\Delta\nu_1^2+\Delta\nu_T^2\right)\right]\\ \cdot\left[P_A(\pi,r)\beta_a(r)\exp\left(-2\pi\alpha_A\left|\frac{n}{\Delta\nu_{FSR1}}+(-1)^k\frac{m}{\Delta\nu_{FSR2}}\right|\right)\right.\\ \left.\left.+P_m(\pi,r)\beta_m(r)\exp\left\{-\pi^2\left[\frac{n}{\Delta\nu_{FSR1}}+(-1)^k\frac{m}{\Delta\nu_{FSR2}}\right]^2\Delta\nu_G^2\right\}\right]\right\},\end{aligned} \tag{A8}$$

where all the symbols have the same meaning as before.

Appendix III. Influence of Refractive Turbulence

This calculation is for the Turbulence coherence length seen from the satellite

This is the Hufnagel-Valley Model of the refractive-index structure parameter from "The Infrared and Electro-Optical Systems Handbook",pp 222

Parameters

$R := 4.95 \cdot 10^{5}$

$A := 1.7 \cdot 10^{-4}$

$W := 21.0$

$$\mathrm{Ca2}(z) := \left(8.2 \cdot 10^{-26} \cdot W^{2} \cdot z^{10} \cdot \exp(-z) + 2.7 \cdot 10^{-16} \cdot \exp\left(-\frac{z}{1.5}\right) + A \cdot \exp(-10.0 \cdot z)\right)$$

This integral is the transverse-field coherence length of a point source located in the scattering volume

$x := 0, 1 \ldots 15$

$$\mathrm{rho}_{x} := 0.058 \cdot \lambda^{\frac{6}{5}} \cdot \left[\left[\int_{0}^{30} \mathrm{Ca2}(y + x) \cdot m^{-\frac{2}{3}} \cdot \left(\frac{y}{R \cdot 10^{-3} \cdot m^{-1}}\right)^{\frac{5}{3}} dy\right] \cdot 10^{3} \cdot m\right]^{-\frac{3}{5}}$$

$\lambda = 9.1 \cdot 10^{-6} \cdot \mathrm{length}$ $\quad R = 4.95 \cdot 10^{5} \cdot \mathrm{length}$

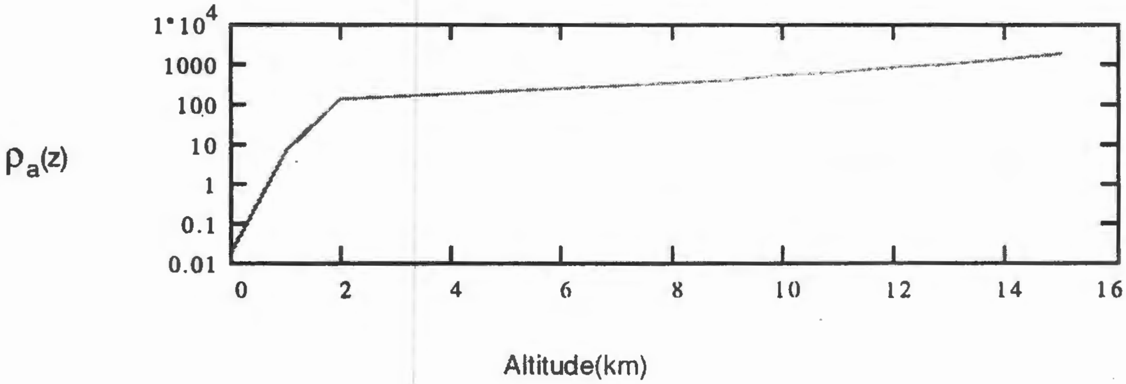

Appendix IV. Coherent Lidar Signal Calculation

This is a basic Mathcad document to develop the predicted output from a coherent Lidar system. The calculation is based on my study of several references described below.

Constants:

$\mathrm{Do} := 1.0 \cdot \mathrm{m}$ $\quad \mathrm{Ao} := \dfrac{\mathrm{Do}^2}{4} \cdot \pi$ $\quad \mathrm{Ao} = 0.785 \cdot \mathrm{length}^2$ $\quad \mathrm{Alt} := 800.0 \cdot 10^3 \cdot \mathrm{m}$

$\eta\mathrm{o} := 0.4$ $\quad \eta\mathrm{d} := 0.5$ $\quad c := 3.0 \cdot 10^8 \cdot \dfrac{\mathrm{m}}{\mathrm{sec}}$ $\quad \mathrm{Alt} := 350.0 \cdot 10^3 \cdot \mathrm{m}$

$\mathrm{Qe} := 0.45$ $\quad h := 6.6260755 \cdot 10^{-34} \cdot \mathrm{joule} \cdot \mathrm{sec}$ $\quad \lambda := 9.1 \cdot 10^{-6} \cdot \mathrm{m}$

$\nu := \dfrac{c}{\lambda}$ $\quad E := h \cdot \nu$ $\quad E = 2.184 \cdot 10^{-20} \cdot \mathrm{mass} \cdot \mathrm{length}^2 \cdot \mathrm{time}^{-2}$

$\beta := 10^{-11} \cdot \dfrac{1}{\mathrm{m} \cdot \mathrm{rad}^2}$ $\quad J := 10 \cdot \mathrm{joule}$ $\quad \tau := (4.7 \cdot 10^{-6}) \cdot \mathrm{sec}$

$\zeta := 45.0 \cdot \mathrm{deg}$ $\quad R := \dfrac{\mathrm{Alt}}{\cos(\zeta)}$ $\quad R = 4.95 \cdot 10^5 \cdot \mathrm{length}$ $\quad f := 100 \cdot R$

$\mathrm{eff} := \eta\mathrm{o} \cdot \eta\mathrm{d} \cdot \mathrm{Qe}$ $\quad \mathrm{eff} = 0.09$

Speckle Distribution

$i := 0 .. 90$ $\quad \mathrm{Ps}_i := \mathrm{md}(1)$ $\quad S_i := \overrightarrow{\ln\left(\dfrac{1.0}{\mathrm{Ps}_i}\right)}$

Signal to Noise Calculation

$\mathrm{So} := \dfrac{\mathrm{Ao} \cdot J \cdot \eta\mathrm{o} \cdot \eta\mathrm{d} \cdot \mathrm{Qe} \cdot \beta \cdot c \cdot \tau}{2 \cdot h \cdot \nu \cdot R^2}$ $\quad \mathrm{So} = 0.931$ $\quad \mathrm{Sa}_i := i \cdot 10^{-9} + 1$ $\quad 1 := 1$

$$\mathrm{So} := \mathrm{So} \cdot \frac{1.0}{\left[1.0 + \left(\dfrac{\mathrm{Do}}{2 \cdot \mathrm{rho}_1}\right)^2 + \left(\dfrac{\mathrm{Ao}}{R \cdot \lambda}\right)^2 \cdot \left(1 - \dfrac{R}{f}\right)^2\right]} \qquad \mathrm{So} = 0.9$$

$\mathrm{SNR} := \mathrm{So} \cdot S$ $\quad \mathrm{SNRa} := \mathrm{mean}(\mathrm{SNR})$ $\quad \mathrm{SNRa} = 0.895$ $\quad \mathrm{Sa}_i := \mathrm{Sa}_i \cdot \mathrm{SNRa}$

$\mathrm{jfl} := -2$ $\quad \mathrm{pfl} := 10^{\mathrm{jfl}}$ $\quad \mathrm{Pb}_i := \mathrm{md}(1)$

$$\mathrm{pd} := \overrightarrow{\left[0.5 \cdot \left(1 + \mathrm{erf}\left(\sqrt{0.5 + \mathrm{SNR}} - \sqrt{\ln\left(\frac{1}{\mathrm{pfl}}\right)}\right)\right)\right]}$$

$\mathrm{Det}_i := \Phi(\mathrm{pd}_i - \mathrm{Pb}_i) \cdot 1.02$

$pfl = 0.01 \qquad \beta = 1 \cdot 10^{-11} \cdot length^{-1}$

This graph shows the probability of detection for these events

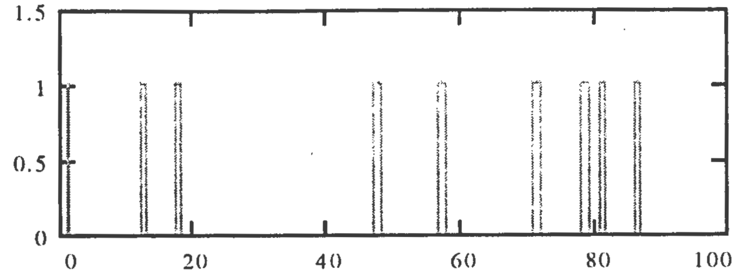

This graph shows theSNR, the average of the SNR and an overbar that shows whether the signal is detected

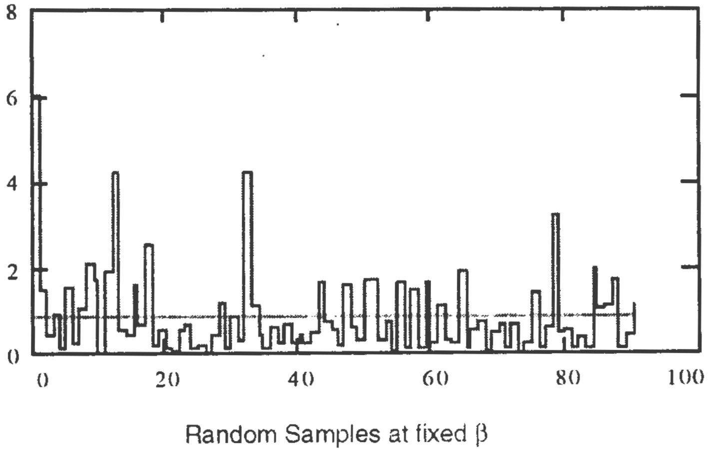

Appendix V. Coherent Lidar Altitude Response with Realistic Aerosol Profiles

Code to determine a matrix of coherent lidar returns as a function of altitude and a random set of observations along the track.

```
;Set System parameters here
LOADCT,3
MZ=31
Z=indgen(MZ)
IS=0
lamda=9.1e-6
model=fltarr(5)
model=[10.,6.,3.5,1.,0.5]
START: IS=IS+1
Print,'Enter the Probability of False Alarm and Abs Model(0-4) #'
Read,pfl,mn
;SET_PLOT,'TEK'
!P.MULTI=[0,0,0,0]
!MTITLE='!18Coherent Lidar Attenuation'
!YTITLE='Altitude'
!XTITLE='Attenuation'
Hw=1.5
atten=fltarr(5,MZ)
for i=0,4 do begin
atten(i,*)=10.0^(-(model(i)/10.0)*exp(-z/Hw))
endfor
;plot,atten(0,*),z
;for i=0,4 do oplot,atten(i,*),z
;print,'Enter 1 to continue'
;read,iq

;START: IS=IS+1
PRINT,'Enter Mixing ratio, Boundary, Background, stratosphere'
read,MBL,MBG,MST
HS=8.0
TAU=1.0
ZBL=1.0
ZST=20.0
DZST=3.0
JBL=FIX(ZBL+0.5)
RHO=Z
RHO=EXP(-(Z/HS))
BETA=RHO
BETA=RHO*(MBG+MBL*10^(-0.75*(Z-ZBL)))$
```

```
   +MST*EXP(-((Z-ZST)/DZST))*EXP(-TAU*EXP(-((Z-ZST)/(2.*DZST))))
BETA(0:JBL)=MBL*RHO(0:JBL)
BETA=BETA*((9.1E-6/LAMDA)^2)

SBG=STRING(MBG,'(E10.2)')
SST=STRING(MST,'(E10.2)')
SBL=STRING(MBL,'(e10.2)')
SPFL=STRING(pfl,'(f5.3)')
SMN=STRING(mn,'(i2)')

water=z
!LINETYPE=0
water=atten(mn,*)
pi=3.14159
Ao=1.0
etao=0.4
etad=0.5
Qe=0.45
c=3.0e8
h=6.626e-34
Joul=10.0
lamda=9.1e-6
tau=1.e-6
alt=350.0e+3
zeta=45.0
Vmax=50.0
Vatmos=3.0
Vbw=0.724
W=sqrt(Vbw^2+Vatmos^2)/Vmax
nu=c/lamda
E=h*nu
R=alt/cos(zeta/57.29578)
So=Ao*Joul*etao*etad*Qe*c*tau/(2.0*E*R^2)
;print,'So=',So

;Begin the random sample loop
ps=fltarr(100)
Speckle=fltarr(100)
SNR=fltarr(MZ,100)
Pd=fltarr(100)
Pb=fltarr(100)
Det=fltarr(MZ,100)
;
for j=0,MZ-1 do begin
be=beta(j)
So=Ao*Joul*etao*etad*Qe*be*c*tau/(2.0*E*R^2)
```

```
;print,So,be
ran=indgen(100)
ps=randomu(seed,100)
Speckle=alog(1.0/ps)
SNR(j,*)=So*Speckle*water(j)
SNN=SNR
SNR(J,*)=SNR(J,*)*SQRT(2.0*PI)*W
Pd=0.5*(1.0+errorf(sqrt(0.5+SNN(j,*))-sqrt(alog(1.0/pfl))))
Pb=randomu(seed,100)
id=where(pb le pd)
;print,n_elements(id)
Det(j,id)=1
im=where(pb gt pd)
;print,n_elements(im)
if(n_elements(im) lt 2) then goto, next
Det(j,im)=0
next:
endfor
it=where(det eq 1)
snm=2.*total(SNR(it))/n_elements(it)
Det=transpose(det)
SNR=transpose(SNR)
SET_PLOT,'X'
!MTITLE='!18Coherent Lidar Signal to Noise'
!YTITLE='Altitude'
!XTITLE='Random Sample Number'
!P.MULTI=[0,0,2,0]
!MTITLE='Detection'
;color_plot,det
;print,'enter 1 to continue'
;read,iq
;snm=max(snr)*0.6
!MTITLE='SNR, pfl ='+Spfl+' Beta0 ='+SBL+' MBG ='+SBG+' MST ='+SST
color_plot,SNR,ran,z,zrange=[0.,snm]
DVb=(0.25/pi)*sqrt(lamda*Vmax/tau)*sqrt(2*pi^1.5*W+$
      16.0*pi^2*W^2/SNR+1.0/SNR^2)
DVb=DVb*(10.0-9.0*DET)
;print,'enter 1 to continue'
;read,iq
!MTITLE='Coherent Lidar, VELOCITY ERROR, Attenuation Model ='+SMN
color_plot,DVb,ran,z,ZRANGE=[0.,5.]

print,'enter 0 to exit,1 continue,  2 for postscript file'
read,iq
if (iq eq 1) then goto, start
if (iq eq 0) then goto, finish
```

```
SET_PLOT,'PS'
DEVICE, /COLOR, BITS_PER_PIXEL=8, FILENAME = 'DUMP.PS', /LANDSCAPE,$
     YOFF=25.85, XSIZE=22.5
!P.MULTI=[0,0,2,0]
!MTITLE='SNR, pfl ='+Spfl+' Beta0 ='+SBL+' MBG ='+SBG+' MST ='+SST
color_plot,SNR,ran,z,zrange=[0.,snm]
!MTITLE='Coherent Lidar, VELOCITY ERROR, Attenuation Model ='+SMN
color_plot,DVb,ran,z,ZRANGE=[0.,5.]
SET_PLOT,'X'
goto, start
finish:
end
```

Appendix VI. Coherent Lidar Power Required with Realistic Aerosol Profiles

Code for Coherent.pro IDL routine

```
;This routine calculates a matrix of coherent lidar returns as a function
;of altitude and a random set of observations along the track for a set of
;aerosol profiles that encompass the observations.

     ;Set System parameters here
MTR=500                  ;number of trials with given aerosol profile
MZ=26                    ;number of altitudes
lamda=9.1e-6             ;wavelength of lidar
pi=3.14159               ;constant pi
Ao=PI/4.0                ;area of main telescope
etao=0.4                 ;optical system efficiency
etad=0.5                 ;detector efficiency
Qe=0.45                  ;quantum efficiency
c=3.0e8                  ;speed of light
h=6.626e-34              ;planks constnt
tau=4.7e-6               ;pulse duration sec
alt=350.0e+3             ;satellite altitude
zeta=45.0                ;zenith angle of lidar
nu=c/lamda               ;frequency
Vmax=50.0                ;dynamic range of detector system m/s
Vatmos=3.0               ;random distribution of atmosphere return, m/s
Vbw=lamda/(4.0*pi*tau)          ;bandwidth of lidar  m/s
W=sqrt(Vbw^2+Vatmos^2)/Vmax
E=h*nu                          ;photon energy
R=alt/cos(zeta/57.29578)        ;range,m
Z=indgen(MZ)                    ;altitde,km
AVER=Z
model=fltarr(5)
model=[10.,6.,3.5,1.,0.5]      ;absorption model parameters
print,'enter 0 for tek,  1 for postscript file'
read,iq

;setup the plotting environment and set device
SET_PLOT,'TEK'
SET_VIEWPORT, 0.15,0.85,0.25,0.85
!x.thick=4
!y.thick=4
!p.thick=2
IF(iq eq 0) then goto,pltek
SET_PLOT,'PS'
!p.font=0
```

```
;device,/landscape,yoff=25.85,xsize=22.5,color=0,filename='DUMP.PS', $
;           /schoolbook,/bold,font_size=16,font_index=19
device,/portrait,color=0,filename='dump.ps', $
      /schoolbook,/bold,font_size=16,font_index=19

Pltek:
!P.MULTI=[0,0,0,0]
IS=0
Print,'Enter the Probability of False Alarm, Abs Model(0-4),AND JOUL #'
Read,pfl,mn,JOUL              ;pulse energy in joules


;Set up the attenuation models
Hw=1.5
atten=fltarr(5,MZ)
for i=0,4 do begin
atten(i,*)=10.0^(-(model(i)/10.0)*exp(-z/Hw))
endfor
;BEGIN THE MAIN AEROSOL PROFILE LOOP HERE THE RANGES ARE
      ;1.0E-09 < MBL < 1.0E-7
      ;1.0E-11 < MBG < 1.0E-9
      ;5.0E-09 < MST < 1.0E-8
MBLA=[1.E-9,1.E-7]
MBGA=[1.E-11,1.E-09]
MSTA=[5.E-10,1.E-9]
FOR IBL=0,1 DO BEGIN
MBL=MBLA(IBL)
FOR IBG=0,1 DO BEGIN
MBG=MBGA(IBG)
FOR IST=0,1 DO BEGIN
IPSM=1+IBL+2*IBG+4*IST
IS=IS+1
MST=MSTA(IST)

;Aerosol models are calculated here based on the observational
;data on aerosol mixing ratios
HS=8.0
TA=1.0
ZBL=1.0
ZST=20.0
DZST=3.0
JBL=FIX(ZBL+0.5)
RHO=Z
RHO=EXP(-(Z/HS))
BETA=RHO
BETA=RHO*(MBG+MBL*10^(-0.75*(Z-ZBL)))$
```

```
    +MST*EXP(-((Z-ZST)/DZST))*EXP(-TA*EXP(-((Z-ZST)/(2.*DZST))))
BETA(0:JBL)=MBL*RHO(0:JBL)
BETA=BETA*((9.1E-6/LAMDA)^2)
;AEROSOL PROFILE KNOWN HERE

SBG=STRING(MBG,'(E10.2)')
SST=STRING(MST,'(E10.2)')
SBL=STRING(MBL,'(e10.2)')
SPFL=STRING(pfl,'(f5.3)')
SMN=STRING(mn,'(i2)')
SJOUL=STRING(JOUL,'(F4.0)')
!LINETYPE=0

water=z
water=atten(mn,*)

;Begin the random sample loop
ps=fltarr(MTR)
Speckle=fltarr(MTR)
SNR=fltarr(MZ,MTR)
Pd=fltarr(MTR)
Pb=fltarr(MTR)
Det=fltarr(MZ,MTR)
;
DVEL=1.0        ;desired velocity accuracy
for j=0,MZ-1 do begin

;optional accuracy range varying with altitude
;if(j gt 3) then dvel=3.0
if(j gt 3) then dvel=1.0
be=beta(j)
So=Ao*Joul*etao*etad*Qe*be*c*tau/(2.0*E*R^2)
ran=indgen(MTR)
ps=randomu(seed,MTR)
Speckle=alog(1.0/ps)
;Speckle probability function known here

SNR(j,*)=So*Speckle*water(j)
SNN=SNR
SNR(j,*)=SNR(j,*)*sqrt(2.0*pi)*W
Pd=0.5*(1.0+errorf(sqrt(0.5+SNN(j,*))-sqrt(alog(1.0/pfl))))
Pb=randomu(seed,MTR)
id=where(pb le pd)
Det(j,id)=1
im=where(pb gt pd)
if(n_elements(im) lt 2) then goto, next
```

```
Det(j,im)=0
next:
endfor

;detection is know here for all points, Det

it=where(det eq 1)
snm=2.*total(SNR(it))/n_elements(it)
Det=transpose(det)
SNR=transpose(SNR)
DVb=(0.25/pi)*sqrt(lamda*Vmax/tau)*sqrt(2*pi^1.5*W+$
        16.0*pi^2*W^2/SNR+1.0/SNR^2)

;RMS error in recovered line of sight velocity know here, DVb

;In this calculation we use the basic
;assumption that for small SNR the case of most interest
;the coherent lidar error is inversely proportional to SNR.
;This assumption favors the system.  A more conservative
;treatment would be to assume gaussian statics and use the
;rms.

POWER=FLTARR(MZ)
DVb=DVb*(1000.0-999.0*DET)>DVEL
EROR=DVEL*DET/DVb
;the factor eror is a counter that estimates the contribution of a given shot
;to that required to achieve the desired accuracy, DVEL.  This counter uses the
;linear assumption for power to SNR.

FOR IZ=0,MZ-1 DO POWER(IZ)=TOTAL(EROR(*,IZ))/N_ELEMENTS(DET(*,IZ))
POWER=JOUL/(POWER+0.0001)
;power is the number of joules required to achieve at least one
;observation of 1 m/s accuracy.  The coherent system requires more
;than one shot on the average to achieve this goal for the low
;aerosol cases

!psym=-1
!Mtitle='Coherent lidar energy requirements, E ='+SJOUL+' JOULES'+$
        ' !C1m/s error'
;       ' !C1m/s error z<3 km; 3 m/s z>3km'

!XTITLE='ENERGY (JOULES)'
!YTITLE='ALTITUDE (KM)
IF(IPSM EQ 8) THEN IPSM=1
ILIN=0
IF(IPSM EQ 8) THEN ILIN=1
```

```
IF(IS EQ 1) THEN PLOT,POWER,Z,XRANGE=[0.,250.],yrange=[0.,25.],XSTYLE=1$
     ,PSYM=-IPSM,SYMSIZE=1.0,LINESTYLE=ILIN
IF(IS NE 1) THEN OPLOT,POWER<250.,Z<30,PSYM=-IPSM,SYMSIZE=1.0$
     ,LINESTYLE=ILIN


ENDFOR
ENDFOR
ENDFOR
xyouts,150,22,'Attuation Model #'+smn,charsize=0.75
!COLOR=1
end
```

References

Abreu, V. J., "Wind measurements from an orbital platform using a lidar system with incoherent detection: An analysis," *Appl. Opt.* **18**, 2992-2997, 1979.

_____, "Lidar from orbit," *Opt. Eng.* **19**, 489-493, 1980.

_____, J. E. Barnes, and P. B. Hays, "Observations of winds with an incoherent lidar detector," *Appl. Optics* **31**, 4509-4514, 1992.

_____, P. B. Hays, B. C. Kennedy, J. Dombrowski, W. R. Skinner, and H. J. Grassl, "Spaceborne incoherent lidar wind sensor: A feasibility study," NASA grant NAG8-741 Final Report, 1989.

_____, T. L. Killeen, and P. B. Hays, "Tristatic high resolution Doppler lidar to study winds and turbulence in the troposphere," *Appl. Opt.* **20**, 2196-2202, 1981.

American National Standards Institute, "American national standard for safe use of lasers," ANSI Z136.1-1993, 1993.

Atlas, D., and C. L. Korb, "Weather and climate needs for lidar observations from space and concepts for their realization," *Bull. Amer. Meteorol. Soc.* **51**, 1270-1285, 1981.

Atlas, R., E. Kalnay, W. E. Baker, J. Susskind, D. Reuter, and Halem, "Observing system simulation experiments at GSFC." In*Proceedings of the NASA Symposium on Global Wind Measurements,* edited by W. Baker and R. Curran, 65-71. Hampton, Va.: Deepak, 1985.

Benedetti-Michelangeli, G., F. Congeduti, and G. Fiocco, "Measurement of aerosol motion and wind velocity in the lower troposphere by Doppler optical radar," *J. Atmos. Sci.* **29**, 906-910, 1972.

_____, F. Congeduti, and G. Fiocco, "Determination of vertical eddy diffusion parameters by Doppler optical radar," *Atmos. Environ.* **8**, 793-799, 1974.

Bevington, P. R., *Data Reduction and Error Analysis for the Physical Sciences*. New York: McGraw Hill, 1969.

Bowdle, D. A., private communication, 1994.

Chanin, M. L., A. Garnier, A. Hauchecorne, and J. Porteneuve, "A Doppler lidar for measuring winds in the middle atmosphere," *Geophys. Res. Lett.* **16**, 1273-1276, 1989.

Couch, R. H., C. W. Rowland, K. S. Ellis, M. P. Blythe, C. P. Regan, M. R. Koch, C. W. Antill, W. L. Kitchen, J. W. Cox, J. F. DeLorme, S. K. Crockett, R. W. Remus, J. C. Casas, W. H. Hunt, "Lidar In-space Technology Experiment (LITE): NASA's first in-space lidar system for atmospheric research," *Opt. Engin.* **30**, 88-95, 1991.

Curran, R. J., D. E. Fitzjarrald, J. W. Bilbro, V. J. Abreu, R. A. Anthes, W. E. Baker, D. A. Bowdle, D. Burridge, G. D. Emmitt, S. E. D. Ferry, P. H. Flamant, R. Greenstone, R. M. Hardesty, K. R. Hardy, R. M. Huffaker, M. P. McCormick, R. T. Menzies, R. M. Schotland, J. K. Sparkman, Jr., J. M. Vaughan, and C. Werner, "LAWS: Laser Atmospheric Wind Sounder. Instrument Panel Report," NASA Earth Observing System Report, Vol IIg, 1987a.

_____, R. R. Nelms, F. Allario, R. A. Bindschadler, E. V. Browell, J. L. Bufton, R. L. Byer, S. Cohen, J. J. Degnan, W. B. Grant, R. Greenstone, W. S. Heaps, B. M. Herman, A. Jalink, D. K. Killinger, L. Korb, J. B. Laudenslager, M. P. McCormick, S. H. Melfi, R. T. Menzies, V. Mohnen, J. Spinhirne, H. J. Zwally, "LASA: Lidar Atmospheric Sounder and Altimeter. Instrument Panel Report," NASA Earth Observing System Report, Vol IId, 1987b.

Dainty, J. C., "Laser speckle and related phenomena." In *Topics in Applied Physics*, Vol. 9, Springer-Verlag, 1984.

Emmitt, D., private communication, 1993.

Fiocco, G., and J. B. DeWolf, "Frequency spectrum of laser echos from atmospheric constituents and determination of the aerosol content of air," *J. Atmos. Sci.* **25**, 488-496, 1968.

_____, G. Benedetti-Michelangeli, K. Maischberger, and E. Madonna, "Measurement of temperature and aerosol to molecule ratio in the troposphere by optical radar," *Nature* **229**, 78-79, 1971.

Fox, C. S., *Infrared and Electro-Optical Handbook, Volume 6, Active Electro-Optical Systems*, Vol 6, pp. 45, copublished by ERIM and SPIE, 1993.

Frehlich, R. G., "Effects of refractive turbulence on coherent laser radar," *Appl. Opt.* **32**, 2122, 1993.

_____, and M. J. Kavaya, "Coherent laser radar performance for general atmospheric refractive turbulence," *Appl. Opt.* **30**, 5325, 1991.

Gagné, J.-M., J.-P. Saint-Dizier, and M. Picard, "Méthode d'echantillonnage des fonctions déterministes en spectroscopie: application à un spectrométre multicanal par comptage photonique," *Appl. Opt.* **13**, 581-588, 1974.

Gras, J. L., and W. D. Jones, "Australian aerosol backscatter survey," *Appl. Opt.* **28**, 852-856, 1989.

_____, C. M. R. Platt, W. D. Jones, R. M. Huffaker, S. A. Young, S. M. Banks, and D. J. Booth, "Southern hemisphere tropospheric aerosol backscatter measurements: Implications for a laser wind system," *J. Geophys. Res.* **96**, 5357-5367, 1991.

Grassotti, R., G. Isaacs, R. N. Hoffman, M. Mickelson, T. Nehrkorn, and J.-F Louis, "A simple Doppler wind lidar sensor: Simulated measurements and impacts in a global assimilation and forecast system," Philips Laboratory Technical Report PL-TR-91-2253, 1991.

Hays, P. B., "Circle to line interferometer optical system," *Appl. Opt.* **29**, 1482-1489, 1990.

_____, V. J. Abreu, M. D. Burrage, D. A. Gell, H. J. Grassl, A. R. Marshal, Y. T. Morton, D. A. Ortland, W. R. Skinner, D. L. Wu, and J.-H. Yee, "Remote sensing of mesospheric winds with the High Resolution Doppler Imager," *Planet. Space Sci.* **12**, 1599-1606, 1992.

_____, V. J. Abreu, M. E. Dobbs, D. A. Gell, H. J. Grassl, and W. R. Skinner, "The High-Resolution Doppler Imager on the Upper Atmosphere Research Satellite," *J. Geophys. Res.* **98**, 10,713-10,723, 1993.

_____, V. J. Abreu, J. Stroga, and A. Rosenberg, "Analysis of a 0.5 micron spaceborne wind sensor." In *Preprint Volume, Conference on Satellite/Remote Sensing Applications,* 25-29 June, pp. 266-271, Clearwater Beach. Boston: American Meteorological Society, 1984.

_____, T. L. Killeen, and B. C. Kennedy, "The Fabry-Perot interferometer on Dynamics Explorer," *Space Sci. Instrum.* **5**, 395-416, 1981.

_____, and R. G. Roble, "Technique for recovering line profiles from Fabry-Perot Interferometer Fringes of very low intensity," *Appl. Opt.* **10**, 193-200, 1970.

_____, and J Wang, "Image plane detector for Fabry-Perot interferometers: Physical model and improvement with anticoincidence detection," *Appl. Opt.* **30**, 3100-3107, 1991.

Hernandez, G., "Analytical description of a Fabry-Perot photoelectric spectrometer," *Appl. Opt.* **5**, 1745-1748, 1966.

_____, *Fabry-Perot Interferometers*, Cambridge Studies in Modern Physics. Cambridge: Cambridge University Press, 1986.

Huffaker, R. M., T. R. Lawrence, M. J. Post, J. T. Priestley, F. F. Hall Jr., R. A. Richter, and R.J. Keeler, "Feasibility studies for a global wind measuring satellite system (Windsat): analysis of simulated performance," *Appl. Opt.* **23**, 2523-2536, 1984.

Jacquinot, P., "The luminosity of spectrometers with prisms, gratings, or Fabry-Perot etalons," *J. Opt. Soc. Am.* **44**, 761-765, 1954.

Kane, T. J., B. Zhou, and R. L. Byer, "Potential for coherent Doppler wind velocity lidar using neodymium lasers," *Appl. Opt.* **23**, 2477,1984.

Kent, G. S., G. K. Yue, U. O. Farrukh, and A. Deepak, "Modeling atmospheric aerosol backscatter at CO_2 laser wavelengths. 2: Modeled values in the atmosphere," *Appl. Opt.* **22**, 1666-1670, 1983.

_____, U. O. Farrukh, P. H. Wang and A. Deepak, "SAGE I and SAM II measurements of 1 mm aerosol extinction in the free troposphere," *J. Appl. Meteor.* **27**, 269-279, 1988.

_____, M. P. McCormick, and S. K. Schaffner, "Global optical climatology of the free tropospheric aerosol from 1.0-mm satellite occulation measurements," *J. Geophys. Res.* **96**, 5249-5267, 1991.

Killeen, T. L., B. C. Kennedy, P. B. Hays, D. A. Symarrow, and D. H. Ceckowski, "Image Plane Detector for the Dynamics Explorer Fabry-Perot Interferometer," *Appl. Opt.* **22**, 3503, 1983.

Kondratyev, K. Y., I. Y. Badinov, G. A. Nikolsky, and E. V. Prokopenko, "Modeling of real profiles of aerosol attenuation," *Tr. Gl. Geofiz. Obs.* **262L**, 1976.

Korb, C. L., B. M. Gentry, and C. Y. Weng, "Edge technique: theory and application to the lidar measurement of atmospheric wind," *Appl. Opt.* **31**, 4202-4213, 1992.

Lawrence, T. R., "The effects of wavelength on coherent Doppler lidar performance." In *Proceedings of the NASA Symposium on Global Wind Measurements*, edited by W.E. Baker and R.J. Curran 183-187. Hampton, VA: Deepak, 1985.

McCormick, M. P., D. M. Winker, E. V. Browell, J. A. Coakley, C. S. Gardner, R. M. Hoff, G. S. Kent, S. H. Melfi, R. T. Menzies, C. M. R. Platt, D. A. Randall, and J. A. Reagan, "Scientific investigations planed for the Lidar In-space Technology Experiment (LITE)," *Bull. Amer. Meteor. Soc.* **74**, 205-214, 1993.

McDermid, I. S., J. B. Laudenslager, and D. Rees, "Ultraviolet-excimer laser-based Doppler Lidar system." In *Proceedings of the NASA Symposium on Global Wind Measurements*, edited by W. Baker and R. Curran, 149-155. Hampton, VA: Deepak, 1985).

McKenzie, R.L. et al., "Multi-wavelength profiles of aerosol backscatter over Lauder, New Zealand, 24 November 1992," *Geophys. Res. Letts.* **21**, 789-792, 1994.

McNutt, D. P., "PEPSIOS purely interferometric high-resolution scanning spectrometer. II. Theory of spacer ratios," *J. Opt. Soc. Am.* **55**, 288-292, 1965.

Menzies, R. T., "A comparison of Doppler lidar wind sensors for Earth-orbit global measurement applications." In *Proceedings of the NASA Symposium on Global Wind Measurements*, edited by W. E. Baker and R. J. Curran, 189-193. Hampton, VA: Deepak, 1985.

_____, "Doppler lidar atmospheric wind sensors: A comparative performance evaluation for global measurements applications," *Appl. Opt.* **25**, 2546-2553, 1986.

_____, M. J. Kavaya, P. H. Flamant, and D. A. Haner, "Atmospheric aerosol backscatter measurements using a tunable coherent CO_2 lidar," *Appl. Opt.* **23**, 2510-2516, 1984.

OSHA, "Guidelines for Laser Safety and Hazard Assessment," OSHA Instructional publication 8-1.7, 1991.

Pless, W. H., B. P. Flannery, S. A. Teukolsky, and W. T. Vetterling, *Numerical Recipes: The Art of Scientific Computing*, Cambridge: Cambridge University Press, 1989.

Post, M. J., "Aerosol backscattering profiles at CO_2 wavelengths: The NOAA data base," *Appl. Opt.* **23**, 2507-2509, 1984.

_____, and R. E. Cupp, "CO_2 lidar backscatter profiles over Hawaii during fall 1988," *Appl. Opt.*, **31**, 4590-4599, 1992.

_____, F. Hall, R. A. Richter, and T. R. Lawrence, "Aerosol backscattering profiles at λ = 10.6 μm," *Appl. Opt.* **21**, 2442-2446, 1982.

Rees, D., and I. S. McDermid, "Doppler lidar atmospheric wind sensor: Reevaluation of a 355nm incoherent Doppler lidar," *Appl. Opt.* **29**, 4133-4144, 1990.

Rosenberg, A., and J. Sroga, "Development of a 0.5 mm incoherent Doppler lidar for space application." In *Proceedings of the NASA Symposium on Global Wind Measurements*, edited by W. E. Baker and R. J. Curran, 157-162. Hampton, VA: Deepak, 1985.

Rothermel, J., D. A. Bowdle, J. M. Vaughan, and M. J. Post, "Evidence of a tropospheric aerosol backscatter mode," *Appl. Opt.* **28**, 1040-1042, 1989.

Schaefer, A. R., R. H. Varian, J. Cover, R. Larsen, "Megapixel CCD thinning/backside progress at SAIC," In*Charge-Coupled Devices and Solid State Optical Sensors II*, SPIE vol. 1447, 165-176, 1991.

Skinner, W. R., P. B. Hays, and V. J. Abreu, "Optimization of a triple etalon interferometer," *Appl. Opt.* **26**, 2817-2827, 1987.

Smith, Frederick G. (ed.), *The Infrared and Electro-Optical Systems Handbook*. Atmospheric Propagation of Radiation, vol. 2. Bellingham, Wa: SPIE, 1993.

Tepley, C. A., S. I. Sargoytchev, and C. O. Hines, "Initial Doppler Rayleigh lidar results from Arecibo," *Geophys. Res. Lett.* **18**, 167-170, 1991.

Thomson, J. A., and F. P. Boynton, "Development of design procedures for coherent lidar measurements of atmospheric winds." Final Report on Contract NOAA-03-7-022-35106, June 1977.

Tratt, D. M., and R. T. Menzies, "Recent climatological trends in atmosphere aerosol backscatter derived from the Jet Propulsion Laborarory multiyear backscatter profile database," *Appl. Opt.* **33**, 424-430, 1994.

Valley, S. L. (ed.), *Handbook of Geophysics and Space Environments.* Air Force Cambridge Research Laboratories, 1965.

Vaugh, J. M., *The Fabry-Perot Interferometer*, Bristol: Adam Hilger, 1989.

Winker, D., private communication, February 11, 1994.

Zrnic, D. S., "Estimation of spectral moments for weather echoes," *IEEE Trans. Geosci. Electron.* **GE-17**, 113, 1979.